UNIVERSIDADE
BEIRA INTERIOR

Analysis and Mitigation Strategies for Torque Fluctuations in Alternative Engines

Daniel Filipe da Silva Cardoso

Tese para obtenção do Grau de Doutor em
Engenharia Mecânica
(3º ciclo de estudos)

Orientadores:
Prof. Doutor Doutor Paulo Manuel Oliveira Fael
Prof. Doutor António Eduardo Vitória Espírito Santo

Júri:
Prof. Doutor José Carlos Páscoa Marques
Prof. Doutor José Luís Soares Esteves
Prof. Doutor Pedro de Figueiredo Vieira Carvalheira
Prof. Doutor Francisco Miguel Ribeiro Proença Brojo
Prof. Doutor Paulo Manuel Oliveira Fael
Prof. Doutor Jorge Manuel Pereira Gregório

abril de 2026

Declaração de Integridade

Eu, Daniel Filipe da Silva Cardoso, que abaixo assino, estudante com o número de inscrição D2267 de Engenharia Mecânica da Faculdade de Engenharia, declaro ter desenvolvido o presente trabalho e elaborado o presente texto em total consonância com o **Código de Integridade da Universidade da Beira Interior**.

Em particular, declaro assumir integralmente a autoria do presente trabalho, afirmando não ter incorrido em qualquer forma de fraude académica, cujas tipologias conheço e reconheço, tendo observado rigorosamente as exigências de referenciação de frases, excertos, imagens e demais formas de criação intelectual. Asseguro ter conduzido todo o trabalho de forma ética, com respeito pelos outros e com orientação pelo bem comum, não tendo recorrido a qualquer prática de fabricação ou falsificação de resultados.

Declaro, ainda, ter utilizado ferramentas de inteligência artificial unicamente para efeitos de melhoria da redação ou da estrutura do texto.

Universidade da Beira Interior, Covilhã, 15 de maio de 2026

Assinado por: **DANIEL FILIPE DA SILVA CARDOSO**
Num. de Identificação: 14496953
Data: 2026.05.15 13:06:46+01'00'

Daniel Filipe da Silva Cardoso

Dedicatória

A concretização deste trabalho de doutoramento não teria sido possível sem o apoio e a contribuição de pessoas extraordinárias. É com um profundo sentido de gratidão que reconheço a importância de cada uma delas nesta jornada.

Em primeiro lugar, um agradecimento sincero a todos aqueles que tornaram este trabalho uma realidade. Ao meu orientador, Professor Paulo Fael, por todas as oportunidades que me enriqueceram enquanto pessoa e investigador, pela sua paciência, inúmeras reuniões, crítica, reflexão e amizade. Ao Professor António Espírito Santo, pelo tempo despendido. Ao Professor Pedro Dinis Gaspar, pelas oportunidades e disponibilidade. Ao Martim Aguiar, pela amizade, trabalho e parceria.

De forma mais emotiva, dedico este trabalho às pessoas de sempre. À Cláudia, pela cumplicidade, motivação, por ser o meu porto de abrigo e, o mais importante de tudo, pela sua impaciência que impulsionou o avanço. E, claro, ao João, que, com a sua chegada, literalmente colocou o ponto final neste trabalho.

Muitos mais haveria para agradecer, mas na impossibilidade de incluir toda a gente, espero sempre ter demonstrado a minha gratidão.

Acknowledgements

This work was made possible through the opportunity and financial support provided by the following institutions and projects:

- Project Centro-01-0145-FEDER-000017 - EMaDeS - Energy, Materials and Sustainable Development, co-financed by the Portugal 2020 Program (PT 2020), within the Regional Operational Program of the Center (CENTRO 2020) and the European Union through the European Regional Development Fund (ERDF);
- Fundação para a Ciência e Tecnologia (FCT);
- R&D Unit C-MAST, "Center for Mechanical and Aerospace Science and Technologies", under project UIDB/00151/2020;
- University of Beira Interior.

Resumo

Nos dias que correm, as alterações climáticas representam uma crise crescente, cujos impactos ambientais, sociais e económicos provocam transformações na sociedade a nível global. No setor dos transportes recai grande parte da responsabilidade pelas emissões globais de gases com efeito de estufa. Neste contexto, a evolução no design de motores e o desenvolvimento de sistemas avançados de controlo têm contribuído para a melhoria do desempenho e da eficiência destes equipamentos.

Apesar dos avanços significativos nos sistemas elétricos aplicados ao setor dos transportes, o desenvolvimento de motores de combustão interna continua a receber investimentos relevantes, dada a sua ampla aplicabilidade e a infraestrutura já instalada. A atenuação das irregularidades de binário provocadas pela natureza intermitente da combustão em motores alternativos, através de atuadores mecânicos, constitui uma solução tecnicamente desafiante, com potencial para colmatar limitações de outras tecnologias e permitir o avanço de soluções atualmente estagnadas.

Neste enquadramento, a presente investigação tem como objetivo observar as irregularidades do binário instantâneo em motores alternativos de combustão interna durante os ciclos de funcionamento, bem como as variações de velocidade associadas. Pretende-se identificar as causas das flutuações de binário, analisando o seu impacto no binário global e na velocidade de rotação do motor. Com base nesta análise, projeta-se um atuador mecânico constituído por uma came e uma mola de compressão, capaz de armazenar e libertar energia de forma a gerar um binário oposto e de igual magnitude ao binário de saída do motor. Este binário contrafásico visa minimizar as flutuações de binário e reduzir significativamente as variações de velocidade, melhorando o funcionamento do motor sem aumentar a inércia do conjunto motriz.

A investigação propõe uma solução puramente mecânica para atenuar as variações instantâneas de binário, com vista a motores mais eficientes e sustentáveis. A validação prática dos atuadores permitirá confirmar a sua aplicabilidade e impacto no desempenho.

Palavras-chave

Motores alternativos; Flutuação de binário; Variação de velocidade; Mecanismo de came de compensação; Perfil da came; Mola de compressão; Validação experimental.

Abstract

Climate change represents an escalating global crisis, with environmental, social, and economic consequences that are reshaping societies worldwide. The transportation sector bears a substantial share of responsibility for global greenhouse gas emissions. In this context, advancements in engine design and the development of advanced control systems have contributed to improved performance and efficiency.

Despite significant progress in the electrification of transport, internal combustion engine (ICE) development continues to receive considerable investment due to its broad applicability and existing infrastructure. A key challenge in ICEs, particularly reciprocating engines, is the mitigation of torque irregularities caused by the intermittent nature of the combustion process. Addressing this issue through mechanical actuators presents a technically demanding yet promising solution, with potential to overcome limitations of alternative technologies and unlock new engineering developments.

This research analyses instantaneous torque irregularities in reciprocating ICEs during their operating cycles and the associated speed fluctuations. It identifies the underlying causes and evaluates their impact on overall engine torque and rotational speed. Based on this analysis, a mechanical actuator composed of a plate cam and a compression spring is designed and optimised. The actuator stores and releases mechanical energy to generate a counteracting torque equal in magnitude and opposite in direction to the engine's output. This counter-phase torque minimizes torque fluctuations and significantly reduces speed variations, improving engine performance without increasing drivetrain inertia.

The study proposes a purely mechanical solution to attenuate torque variations, contributing to more efficient and environmentally sustainable engines. Practical validation of the actuator will confirm its applicability and performance impact.

Keywords

Alternative Engines; Torque fluctuation; Velocity variation; Balancing cam mechanism; Cam profile; Compression Spring; Experimental validation.

Index

List of figures

List of tables

List of acronyms

BDC	Bottom Dead Centre
CAD	Computer Aided Design
DMF	Dual-Mass Flywheels
EVs	Electric Vehicles
GDI	Gasoline Direct Injection
GHC	Global Greenhouse Gas
HCCI	Homogeneous Charge Compression Ignition
ICE	Internal Combustion Engine
LDR	Light Dependent Resistor
RPM	Rotation Per Minute
SCR	Selective Catalytic Reduction
SRM	Switched Reluctance Motor
TDC	Top Dead Centre
VR	Variable Reluctance

1. Introduction

1.1. Framework

1.1.1. Climate emergency

The climate emergency is an acute and escalating crisis, posing severe environmental and public health threats to global economies. Such crisis has been articulated with a sense of urgency, stressing the critical need for immediate and transformative actions to address the various aspects of climate change. The rapid escalation of climate-related disasters, such as floods, heat waves, wildfires, hurricanes, and cyclones, that have occurred across the globe since 2019 serve as harrowing reminders of the increasing volatility of our climate system and the tangible impact of climate change on various ecosystems and communities. These changes lead to environmental degradation and pose significant risks to global biodiversity, water security, and agricultural productivity, with far-reaching implications for human livelihoods and well being. Furthermore, the transportation sector is identified as a critical area for intervention in mitigating climate change as well as innovative solutions that promote the efficient use of fossil fuels are essential for reducing the sector's carbon footprint and contributing to environmental conservation [1], [2].

1.1.2. Relationship between transport and climate changes

The transportation sector, along with agricultural machines, construction machines, and overall, all engine-powered machines, is a significant contributor to global greenhouse gas (GHG) emissions and influences climate change primarily through the consumption of fossil fuels. Gasoline and diesel-powered vehicles and engine-powered machines release various GHGs, including carbon dioxide (CO_2), methane (CH_4), and nitrous oxide (N_2O); the sector is responsible for a considerable portion of worldwide CO_2 emissions, a key factor in climate change, with a noticeable increase in emissions paralleling the rise in global vehicle use [3], [4].

Road vehicles, particularly passenger cars and heavy-duty trucks, are the largest emitters within the sector. However, aviation and maritime transport also play a significant role, especially considering their fuel-intensive nature and the long distances covered. The intensity of transportation's impact on climate change varies regionally; developed countries with higher vehicle user rates and extensive road and air travel networks tend to have higher transportation-related emissions. Nonetheless, developing countries are rapidly catching up, driven by economic growth and urbanization, leading to increased

vehicle ownership and freight transport. Urban areas, with their high concentration of vehicles, are particularly significant in the context of transportation-induced emissions, placing challenges faced by cities worldwide, such as traffic congestion and air pollution, exacerbate the climate impact [3], [4].

1.1.3. Impact of internal combustion engines in the transport and energy sectors

The internal combustion engine (ICE) significantly impacts both the transport and energy sectors, exploring its wide-ranging effects based on various studies [5], [6], [7]. For over a century, ICEs have powered most road vehicles, enabled unprecedented mobility and economic growth, and presented significant environmental challenges. Despite the rising prominence of electric vehicles (EVs), ICE vehicles continue to dominate the global landscape, especially in areas where the electric infrastructure is still underdeveloped. In 2020, the number of electric cars worldwide surpassed 10 million, marking a 43% increase from the previous year. However, this number pales compared to the approximated 1.4 billions of ICE vehicles in operation, highlighting the slow transition [8].

Beyond their pivotal role in transportation, ICEs are used in small-scale energy production, particularly in remote or off-grid areas, where they serve as generators for electricity or co-generation systems. This application is vital for energy access and contributes to localized pollution and GHG emissions. To mitigate the environmental impact of ICEs, advances in engine technology have led to a 20-30% increase in energy efficiency for modern diesel engines compared to their gasoline counterparts. Furthermore, adopting alternative fuels, such as biofuels, and hybridization techniques are being explored to reduce ICE operations carbon footprint significantly [5].

The transition towards EVs is a key strategy in reducing the transport sector's environmental impact. Several comparative analyses have demonstrated the potential for lower life cycle emissions with EV adoption. Nonetheless, this transition is heavily dependent on developments in battery technology, the expansion of charging infrastructure, and electricity generation sources. An important consideration is the uneven pace of global progress, with some developed countries aiming for significant electrification of their vehicle fleets by 2030, while many developing countries have no choice but to depend on ICE vehicles due to infrastructural and economic constraints [8].

1.1.4. Technologies for more efficient engines

The need to reduce emissions and improve energy use drives efforts to enhance ICE efficiency. Based on studies, several strategies have emerged [7] [9], [10].

Essential techniques like variable valve timing, direct fuel injection, and turbocharging optimize combustion in traditional fossil fuel engines, reducing emissions and boosting efficiency [11]. On the other hand, synthetic fuels, derived from natural gas, biomass, or CO2 capture, offer a viable alternative, cutting the carbon footprint of ICEs while being compatible with current technologies [9].

Engine design, like the downsize or downspeed trend and control innovations, including advanced algorithms and AI, has led to better performance and lower emissions [12]. Integrating electrification, mainly through hybrid powertrains, reduces fuel consumption and emissions by combining electric motors with ICEs [13], [14].

Advances in combustion systems like Homogeneous Charge Compression Ignition (HCCI) and Gasoline direct injection (GDI), alongside the integration of electric components, significantly improve efficiency [13], [14]. Hence, Modern emissions control systems, such as Selective Catalytic Reduction (SCR) and particulate filters, are critical in reducing pollutants like NOx and particulate matter [10]. Hydrogen and dual-fuel engines, capable of running on both conventional and alternative fuels like hydrogen, present additional opportunities for efficiency gains [15].

These technologies illustrate the diverse pathways available for enhancing engine efficiency. Each approach has a single solution; rather, a combination of these strategies will likely be necessary to achieve significant advancements in ICE efficiency.

1.2. Objectives and work relevance

The present document objectives align with the urgent need to address the climate emergency through technological innovations in the transportation and energy sectors. It intends to contribute with innovative technologies or solutions and advance our understanding.

1.2.1. Specific objectives

This research aims to investigate instantaneous torque irregularities in alternative internal combustion engines during their operational cycles and the resulting velocity

variations. The study will involve a thorough identification of the root causes of these fluctuations, with an emphasis on understanding their impact on overall engine performance.

Building upon this analysis, the research focuses on the design and optimization of a mechanical actuator composed of a plate cam and a compression spring. This actuator operates by storing and subsequently releasing mechanical energy in a controlled manner, generating a counteracting torque that is equal in magnitude and opposite in direction to the engine's output torque. By introducing this compensating effect, the actuator minimizes torque fluctuations, significantly reducing velocity variations and enhancing engine smoothness, all without increasing the system's rotational inertia.

Simulation tools will be employed to model and analyse the influence of multiple engine parameters on torque variations. These simulations will guide the design process and help predict the actuator's effectiveness under different operational conditions. Following the simulations, experimental tests will be conducted to validate the accuracy and reliability of the computational models developed and the proposed solutions.

Finally, the research will focus on integrating the developed cam-follower actuator into the engine system. Following integration, additional experimental tests will be conducted to assess its practical performance. The results obtained will then be compared with the simulation data to validate the design, verify consistency, and confirm the actuator's effectiveness under real operating conditions.

1.2.2. Relevance in the context of more efficient engines and innovative aspects

Despite significant advancements in electrical systems in transportation, the development of ICEs continues to receive substantial financial investment from companies due to the immediate and widespread applicability of improvements in ICE technology. This persistent investment is driven by the versatility and existing infrastructure supporting ICEs, which remain predominant in various sectors, including automotive, marine, and small-scale electric power generation [16], [17], [18].

Torque irregularities in ICEs are caused by the intermittent combustion process inherent in ICE operation, which results in non-uniform torque output and manifests as torque ripple or fluctuations [19], [20]. Addressing these torque fluctuations by introducing mechanical actuators can significantly enhance engine smoothness and efficiency,

harmonize the produced torque and compensating for velocity variations during the engine cycle [21], [22].

The research involves studying instantaneous torque variations in alternative engines, identifying root causes, and understanding their impact on engine performance. This foundational knowledge is then applied to design and optimize mechanical actuators that can store and release energy effectively, thereby mitigating torque fluctuations and velocity variations. Moreover, the integration of these mechanical actuators is tested to confirm their applicability and effectiveness [23], [24] [25], [26], [27], [28], [29].

The outcomes of this research align with global efforts toward sustainable development, particularly in reducing transportation's carbon footprint and promoting technological advancements in energy efficiency. This research supports the transition towards more efficient and environmentally friendly engines by providing a lightweight, adaptable solution that can be seamlessly integrated into existing engine designs. This approach contrasts with traditional, bulkier methods such as flywheels, which add significant mass and inertia and do not dynamically adapt to varying operational conditions [30], [31].

The innovative solutions presented in this work have the potential for wide-scale application across various types of ICEs. The successful implementation of these mechanical actuators could lead to significant improvements in engine performance, reduced emissions, and lower fuel consumption. Furthermore, the adaptability of this technology supports its integration into hybrid vehicles, range extenders, and micro-cogeneration systems, thereby broadening its impact on reducing global GHG emissions [32], [33], [34].

By addressing the multifaceted challenges of torque management in ICEs, this research advances the development of engine technologies that align with the evolving demands of modern transportation. The integration of these mechanical actuators has immediate effects on engine operation and promotes the successful implementation of other complementary technologies. [28], [35], [36].

1.2.3. Limitations of conventional torque smoothing solutions and motivation for a mechanical alternative

Instantaneous torque fluctuations are inherent to internal combustion engines due to the discontinuous nature of the combustion process. At low engine speeds where inertial effects are insufficient to dampen cyclic variations these fluctuations result in significant rotational speed irregularities. Such irregularities negatively affect the stability,

efficiency, and durability of downstream systems, including powertrains and generators [16], [17], [19], [20], [37].

Traditional strategies to address this issue have relied on passive mechanical components, such as conventional and dual-mass flywheels (DMF). While these devices provide some smoothing, they inherently increase system mass and are not adaptive to real-time variations in engine speed or load [21], [22]. Their bulk and limited response make them suboptimal for lightweight or compact systems such as hybrid powertrains and portable generators, where packaging, weight, and maintenance constraints are more severe [23], [24], [25]. Active methods involving control systems and torque cancellation have also been explored [26], [27], [29], but they frequently require complex electronic architectures and extensive sensor integration.

To overcome these limitations, various mechanical alternatives have emerged in recent years. DMFs remain widely used, particularly at idle, yet they function effectively only over narrow frequency ranges and contribute significant weight [21], [25], [38]. Centrifugal pendulum vibration absorbers are often integrated into flywheels or clutches to absorb low-order torsional oscillations passively. However, their effectiveness is confined to tuned frequency ranges, and their physical integration presents packaging challenges [39], [40].

Other approaches involve kinematically driven mechanisms, such as the design by Pfabe and Woernle [41], which couples a secondary flywheel to the crankshaft via a non-uniform gear system. This configuration generates counteracting inertial torque aligned with the engine's dominant harmonic. Despite its effectiveness in reducing speed variation, it introduces mechanical complexity and lacks adaptability across varying speeds. Similarly, variable inertia flywheels, such as the system proposed by Zhang et al. [28], utilize sliding masses that shift in response to angular acceleration, thereby modifying the effective inertia without requiring external control. These designs offer promising results during transients but may suffer from long-term durability concerns due to their mechanical intricacy.

Among emerging passive solutions, cam-spring mechanisms have gained attention for their compactness and potential to dynamically store and release energy in synchrony with the engine cycle. Arakelian and Briot [31] proposed a system for simultaneous force and torque compensation in slider–crank mechanisms, which inspired further innovations. Lin et al. [30] later adapted this principle to valve trains, demonstrating static compensation of torque fluctuations at the camshaft level. However, these

solutions were not applied to the crankshaft and were not validated over the whole engine cycle.

In this context, the present work proposes a balancing cam mechanism, consisting of a purpose-designed cam and a spring-loaded follower, to passively counteract torque and velocity fluctuations throughout the entire four-stroke cycle. Synthesized from experimental torque data, the system dynamically compensates torque deficits in phase with crankshaft rotation, particularly improving performance under idle conditions. Unlike pendulum-based or inertia-variable systems, the proposed mechanism introduces no added rotating mass and requires no actuation or control logic. It presents a lightweight, passive alternative for enhancing rotational smoothness with minimal mechanical overhead [42].

The present research is grounded on the hypothesis that instantaneous torque and velocity fluctuations in reciprocating internal combustion engines can be mitigated. This is achieved through a passive mechanical actuator. The actuator consists of a plate cam and a compression spring and is designed to generate a counter-phase compensating torque.

1.3. Research hypothesis and research questions

It is hypothesised that, by accurately defining the cam geometry and spring stiffness, the actuator can store and release mechanical energy in sync with the engine cycle. This process produces a compensating torque equal in magnitude but opposite in direction to the driving torque fluctuations. This counteracting behaviour should reduce cyclic variations in angular velocity. It does so without increasing the system's inertia or requiring extra control or actuation systems. As a result, the mechanism would enhance the smoothness, efficiency, and stability of engine operation. It maintains a lightweight and purely mechanical configuration.

Based on this hypothesis, the following research questions were formulated to guide the investigation. These questions ensure a coherent progression from problem characterization to modelling, optimization, and experimental validation.

1. How can instantaneous torque fluctuations in reciprocating internal combustion engines be modelled and quantified, and how do these fluctuations influence the resulting angular velocity throughout the operating cycle?

2. How can a mechanically driven actuator based on a cam–spring system generate an opposite-phase compensating torque capable of attenuating velocity fluctuations without increasing the system's rotational inertia?

3. Which geometric and functional parameters of the cam–spring assembly most significantly influence the efficiency of torque compensation, and how can these parameters be optimised for different engine operating conditions?

4. To what extent do the experimental results validate the numerical predictions regarding torque fluctuation reduction and engine speed stabilization when the balancing cam mechanism is applied?

Together, the research hypothesis and questions define the methodological framework of this thesis. They set a structured sequence. It starts with identifying and quantifying torque irregularities. It progresses to the design, optimization, and experimental validation of a novel mechanical solution to improve the rotational regularity of alternative internal combustion engines.

1.4. Structure of the thesis

This investigation delves into the challenges of torque production in alternative internal combustion engines, focusing on developing, integrating, and assessing a mechanical actuator, specifically the balancing cam mechanism. It also examines existing studies, exploring the mechanism's integration into other engine cycles facing torque production challenges and alternative strategies for torque issue mitigation. The introduction sets the research context, aims, and motivations, then progresses through a theoretical foundation, computational engine modelling, experimental methods, and performance analysis, concluding with discussions on future research directions and summaries of related studies.

Introduction: This chapter sets the stage by discussing the global climate emergency and the urgent need for sustainable solutions to mitigate climate change. It examines transportation's significant role in contributing to greenhouse gas emissions and the broader impact of ICEs. The chapter outlines various strategies for achieving more efficient engines and reducing emissions; additionally, it presents the specific objectives of the research and the innovative aspects and provides an overview of the thesis structure and the topics to be addressed.

Theoretical foundations: It offers an overview of the historical development of ICEs, examining various alternative ICE cycles and their distinct characteristics. The review explores critical issues related to torque production, identifying the causes and consequences of irregularities and discussing the mechanisms and technologies, such as flywheels, dual-mass flywheels, and balance shafts, that have been developed to address these challenges. Additionally, the chapter covers the theoretical concepts essential for the development of the mechanical actuator.

Engine torque simulation and experimental validation: This chapter discusses the methodology and tools for simulating instantaneous torque in internal combustion engines. It covers the simulation process for four-stroke alternative engines. The results of these simulations are presented, focusing on the torque production challenges. The chapter also details the experimental setup used to validate the simulation results, followed by a comparative analysis of the simulation and experimental findings.

Mechanical actuator - Balancing cam mechanism: Presents a conceptual framework for the balancing cam mechanism, detailing its architecture and components and elucidating how it enhances torque consistency in internal combustion engines, the process and analysis used to define the balancing cam profile. The chapter then explores distinct design strategies for implementing the mechanism, whether exclusively during engine idle or with variation in the spring pre-charge. It discusses integrating the balancing cam mechanism with the internal combustion engine, followed by a performance evaluation and result study regarding its integration. The construction of the balancing cam mechanism, manufacturing processes, and assembly techniques are detailed. An experimental framework designed to test the balancing cam mechanism within an engine system is presented, including the testing setup, parameters measured, and analysis conducted to evaluate the mechanism's impact on torque consistency and overall engine performance.

Analysis of results and discussion: This chapter analyses the results obtained from the research and discusses their implications by outlining the key benefits and advantages of the balancing system. The chapter then analyses the performance improvements achieved through the torque correction mechanism and compares the experimental results to those obtained through simulation.

Conclusion and future works: The key findings of the research are summarized, highlighting the achievement of the set objectives. The significance of the study is discussed, emphasizing the contributions made to the field of engine technology. This

chapter explores the implications of integrating mechanical actuators, demonstrating how these innovations can lead to more efficient and environmentally friendly engines. Concluding remarks reflect on the overall impact of the research and potential future advancements. The chapter also introduces future work that builds on the presented study, extending its impact and scope.

2. Theoretical foundations

2.1. Engines historical context and definition

The development of heat engines reflects a cornerstone of technological advancement, with roots extending over two and a half centuries [43]. Among the most significant milestones in this evolution was Nikolaus Otto's invention of the four-stroke engine with pre-compression, patented in the late 19th century. Otto's design established a new standard for engine efficiency and performance despite facing legal challenges that questioned the validity of its patent [44]. This engine, often called the "Otto cycle", became the foundation for most ICEs used in subsequent decades.

As the 20th century approached, engine design rapidly diversified. Rudolf Diesel's introduction of the compression ignition engine, commonly known as the Diesel engine, marked a significant departure from Otto's principles. Diesel's engine, characterized by higher thermal efficiency due to its fuel ignition through the compression method, represented a new operational cycle distinct from the Otto cycle [45]. This innovation quickly became widespread, particularly in sectors requiring robust and fuel-efficient engines.

Throughout the 20th century, internal combustion engines became integral to global transportation and industry. Their application expanded beyond land-based vehicles to include aviation and marine transportation [46]. The continual pursuit of increased efficiency and adaptability led to multiple engine configurations and hybrid designs, which combined traditional, ICE principles with emerging technologies like electric motors [47], [48]. Notably, the aviation industry experienced a significant transition during this period, moving from piston engines to more powerful and efficient turbine engines that could meet the demands of modern aircraft.

Despite the rise of EVs in the 21st century, ICEs dominate road transportation. However, they now face increasing pressure to adapt to stringent environmental regulations and the urgent need for sustainable energy solutions [49]. The modern era has seen significant developments in fuel technology, emissions reduction, and hybridization as critical areas of research and development [50]. Notable achievements in the 21st century include the creation of high-efficiency turbocharged engines [51], the enhancement of direct fuel injection systems [52], and the integration of sophisticated emission control technologies [53]. Such innovations reflect the ongoing evolution of ICEs, ensuring their continued viability in a rapidly transforming automotive landscape.

The intensive search for alternative fuels, improvements in engine design, and the integration of intelligent technologies are central to the ongoing evolution of internal combustion engines [54], [55]. These advancements are driven by the need to address contemporary challenges such as reducing greenhouse gas emissions, improving fuel efficiency, and meeting the demands of a global population increasingly concerned with environmental sustainability [56], [57]. As a result, ICEs continue to evolve, adapting to the modern-day demands of the automotive industry and ensuring their relevance in the context of future transportation needs [58].

2.1.1. Heat engines

Heat engines convert thermal energy into mechanical energy, typically derived from the combustion of a fuel-oxidizer mixture, releasing the fuel's chemical energy. Air is the common oxidizer, though oxygen-containing compounds are used in applications like rockets. The energy released is transferred to the working fluid, which undergoes cyclical changes and transmits this energy to the engine's mechanical components. In jet engines, the fluid generates thrust for propulsion performing work through pressure and volume variations induced by heat. This fluid can either pulsate within a variable volume cavity, as in volumetric engines or flow continuously, using its kinetic energy in dynamic engines [44], [59], [60].

Volumetric engines are clustered into reciprocating and rotary types. Reciprocating engines involve the active fluid changing within a variable volume cylinder, transferring energy to a moving piston, which drives the engine using a crank-connecting rod system. In rotary engines, the variable volume develops between a rotor and an enclosing casing, with the rotor connected to the drive shaft.

External combustion engines transfer heat to the working fluid through a heat exchanger without the fluid participating in combustion, while steam engines are an example, where water is heated to produce steam that drives the engine. Internal combustion engines have combustion occurring within the working fluid. The active fluid, a mixture of air and fuel, burns in a specific part of the engine cycle [44], [59], [60].

Dynamic engines or turbo-engines involve the continuous flow of the working fluid, delivering energy to blades with aerodynamic profiles. This kinetic energy is used for thrusting in jet engines, propelling the vehicle by reaction, with a small part of the gas energy moving the compressor [61].

Table 1 Heat engines classification.

Heat engines	Volumetric	Dynamic
Internal combustion	Alternative (piston engine)	Rotative (gas turbine)
	Rotative (Wankel engine)	Reaction (jet)
External combustion	Stirling engine	Steam turbine

Figure 1 illustrates different types of internal combustion engines, comparing two distinct engine configurations: the reciprocating volumetric engine, or alternative engine on the left, and the dynamic rotary engine on the right. The reciprocating volumetric engine operates by the linear movement of a piston within a variable-volume cylinder. This movement is converted into rotational motion via a crankshaft mechanism. This engine type has a distinct torque production profile, with cyclical variations corresponding to the piston's reciprocating motion. These torque variations are critical for developing and optimizing smooth and efficient performance. On the other hand, the dynamic rotary engine, such as a gas turbine, operates by the continuous flow of the working fluid through a series of aerodynamic blades. This engine type provides a relatively constant torque output due to the continuous nature of its fluid dynamics, resulting in smoother operation compared to reciprocating engines [44], [59], [60], [61], [62]. The forthcoming work will focus on alternative engines like the reciprocating volumetric engine represented in Figure 1.

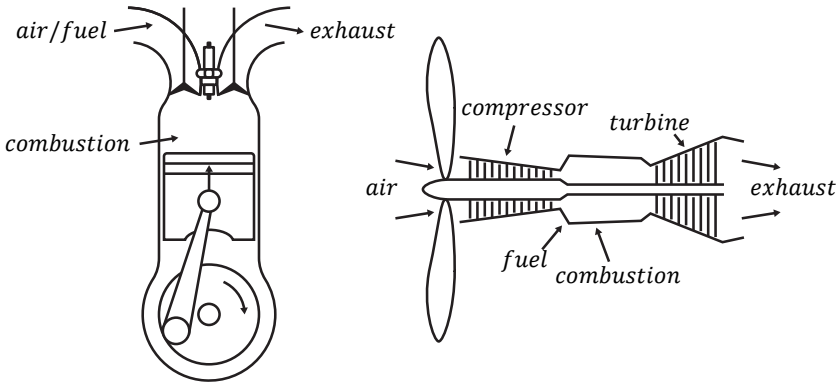

Figure 1 Comparison of a reciprocating volumetric engine (left) and a dynamic rotary engine (right), adapted from [61].

2.1.2. Alternative internal combustion engines classification

The field of ICEs encompasses several mechanisms and thermodynamic cycles, each with unique characteristics. The classification of the different types of ICEs based on various

criteria, including ignition type, thermodynamic cycle, working cycle, engine configuration, applications, combustion chamber types, valve or port placement, camshaft design, fuel type, mixture preparation methods, mixture control methods, cooling methods, and lubrication methods [61], as presented on Table 2.

Table 2 Alternative internal combustion engines classification.

Category	Type
Working cycle and type of ignition	Spark Ignition (SI) or Compression Ignition (CI) Two-Stroke, Four-Stroke or Eight-Stroke
Valve or port placement and camshaft design	Camshafts in the block with side valves Overhead valves with camshafts in the block or overhead Two-stroke engines ports
Fuel type	Gasoline, Diesel, Gas (CNG, LPG), Alcohol (methanol, ethanol) or Hydrogen
Induction method	Naturally Aspirated or Forced Induction
Injection type	Direct fuel injection into the cylinder Indirect Injection with auxiliary chamber
Mixture preparation method	Direct fuel injection into the cylinder Fuel injection into intake manifolds or carburettor
Cylinder arrangement	Inline, V-type, Radial, Horizontally opposed (boxer) or Opposed piston
Cooling method and lubrication method	Cooled by water, oil, or air. Splash lubrication or pressure lubrication. Mixed lubrication (two-stroke engines).
Applications	Automotive, trucks, light aircraft, boats, power generation systems, etc.

2.2. Alternative internal combustion engines

2.2.1. Working principle

In alternative internal combustion engines, the combustion process increases the gas temperature inside the cylinder, raising the pressure and causing the piston to move downward from the Top Dead Centre (TDC) to the Bottom Dead Centre (BDC). TDC represents the piston's closest approach to the engine head, while BDC is the furthest

point from the engine head in its reciprocating motion [61]. The distance between TDC and BDC is defined as the stroke S , and the internal diameter of the cylinder housing the piston is the bore B. The volume displaced by the piston moving between TDC and BDC is termed the displacement volume V_d. The volume above the piston at TDC is the combustion chamber volume V_c. Conversely, the total volume V_t encompasses the cylinder volume when the piston is at BDC. The V_d and V_t can be obtained respectively from Equations 1 and 2[61].

$$V_d = \pi \left(\frac{B}{2}\right)^2 S \tag{1}$$

V_d $-$ *displacement volume*

$B-$ *bore*

$S-$ *stroke*

$$V_t = V_d + V_c \tag{2}$$

V_t $-$ *total volume*

V_d $-$ *displacement volume*

V_c $-$ *combustion chamber volume*

The crank-connecting rod assembly converts the piston's reciprocating motion, driven by the expansion of gases under pressure, into rotational motion. Figure 2 illustrates the fundamental geometry of an alternative internal combustion reciprocating engine, depicting the role of the crank-connecting rod assembly in translating the piston's linear motion into the crankshaft's rotational motion.

The ratio between the stroke and the bore, known as the stroke-to-bore ratio, are crucial to determine engine characteristics; engines are classified as square (stroke equal to bore), oversquare (stroke less than bore), or undersquare (stroke greater than bore). An oversquare engine tends to allow higher engine speeds due to a shorter stroke, while an undersquare engine typically provides higher torque due to a longer stroke.

The compression ratio ϵ determined by Equation 3, defined as the V_t ratio when the piston is at BDC to the combustion chamber volume V_c at TDC, is a critical parameter influencing engine efficiency and performance.

$$\epsilon = \frac{V_t}{V_c} = \frac{V_d + V_c}{V_c} \tag{3}$$

ϵ $-$ *compression ratio*

For gasoline engines, typical compression ratios range between 8:1 and 11:1. Engines with forced induction, such as turbocharged engines, often have slightly lower compression ratios to accommodate higher pressures from the turbocharger. Conversely, engines using alcohol fuels can sustain higher compression ratios due to the higher knock resistance of alcohol. During the compression stroke, pressure, and temperature increase within the cylinder, the engine experiences pressure elevation. The gas pressure at the end of the compression stroke is generally higher than that calculated by the geometric volume ratio alone due to the heat added during compression. This requires a polytropic compression process with an exponent near 1.4 [61].

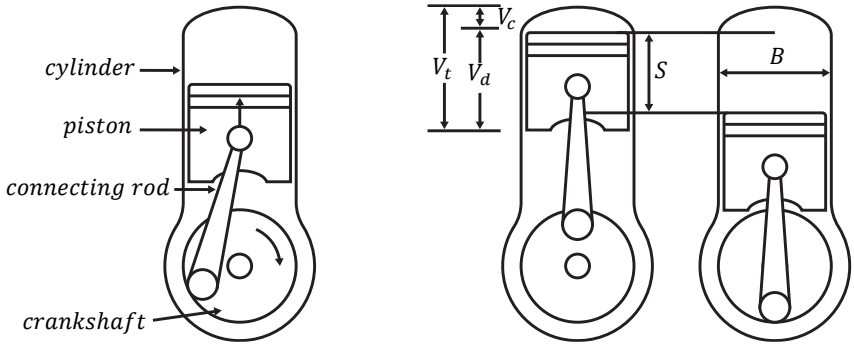

Figure 2 Representation of the basic components of an alternative internal combustion engine on the left, and the piston's positions at TDC and BDC on the right, showing the respective volumes Vd, Vt and Vc, adapted from [61].

2.2.2. Working cycles

2.2.2.1. Two-stroke cycle

The two-stroke engine differs from the four-stroke engine or eight-stroke that has only one power stroke out of four or eight, respectively, leading to operational irregularities. To address these issues, a two-stroke engine design eliminates the intake and exhaust strokes by performing these operations simultaneously when the piston is near the BDC. This results in a cycle with four phases (intake, compression, power, and exhaust) completed in just two strokes (piston movements). Consequently, a two-stroke engine completes the four stages of the cycle in each revolution (360°) of its crankshaft.

The structure of a two-stroke engine differs slightly from the four-stroke engine because it dispenses the valve system, making the engine much simpler. Instead, fresh mixture and burnt gases enter and exit the cylinder through openings in the cylinder walls, called ports, which are opened and closed by the piston during its movement. Pre-compression of the mixture to be admitted into the cylinder is necessary, often achieved in the crankcase by the action of the lower part of the piston [61], [63].

1st Half revolution (0-180°) is expansion-exhaust stroke: As the piston approaches TDC, the fuel-air mixture is compressed to its maximum. Shortly before reaching TDC, the mixture is ignited by a spark, initiating combustion. The expansion of the combustion gases and the associated release of energy increases the temperature and pressure within the combustion chamber, causing the piston to perform work. This work is transmitted through the connecting rod to rotate the crankshaft. As the piston moves downward, it uncovers the exhaust port. This opening allows the burnt gases to be expelled, driven by the high pressure in the combustion chamber. In contrast, the pressure in the exhaust port is approximately atmospheric, creating a significant pressure differential [61], [63].

As the piston continues its downward movement and approaches BDC, it also uncovers the transfer port. At this point, the cylinder pressure is lower than the pressure in the crankcase due to the descending movement of the piston, creating pressure on the mixture in the crankcase. This pressure difference causes the fuel-air mixture to flow from the crankcase into the combustion chamber, assisting in exhausting the burnt gases. When the piston reaches BDC and begins to ascend again, the transfer port is closed, and the cycle begins anew with the second stroke [61], [63].

2nd Half revolution (180°-360°) is intake-compression: This movement corresponds to the piston's return stroke to TDC. When the piston reaches BDC, it begins to move toward TDC. At the start of this movement, the transfer port is open, allowing the air-fuel mixture to enter the cylinder. Once the transfer port is closed, the entry of the air-fuel mixture stops, and the piston compresses the mixture inside the cylinder during the remainder of its upward stroke. As the piston moves from BDC to TDC, a vacuum is created in the crankcase due to the upward movement of the piston's lower part. This vacuum allows the atmospheric air-fuel mixture to enter the crankcase, which will be compressed during most of the following stroke. At the end of the compression, a spark from the spark plug ignites the mixture, initiating a new cycle [61], [63].

Two-stroke engines generally have a similar structure, featuring a simple mechanism and few moving parts. The main differences rely in admitting and pre-compressing the air-fuel mixture and scavenging the cylinder. The piston functions as a valve, opening and closing all engine ports, as shown in Figure 3.

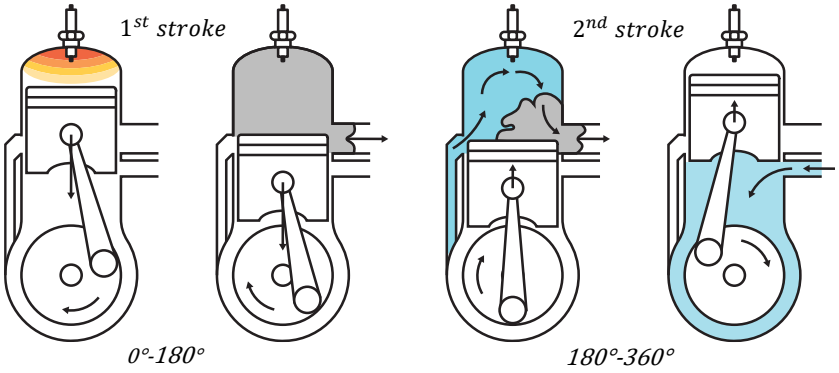

Figure 3 The operation of a two-stroke engine, adapted from [61].

Although less common, two-stroke Diesel engines also exist and implement a distinct working cycle compared to the more widespread two-stroke gasoline engines described above. In these Diesel variants, crankcase pre-compression and spark ignition are not used. Instead, fresh air is forced into the cylinder using external devices such as blowers or turbochargers. Fuel is directly injected into the highly compressed air near top dead centre, and combustion occurs by compression, following the Diesel cycle. Intake and exhaust processes occur near bottom dead centre through a scavenging phase, where fresh air enters and expels the burnt gases. This alternative working cycle is typically found in marine propulsion systems, stationary power generators, and heavy-duty applications, where high torque output and mechanical robustness are crucial [64], [65].

2.2.2.2. Four-stroke cycle

The four-stroke cycle is prevalent among ICEs, despite having a more complex engine when compared to the two-stroke engines can achieve more efficiency and less emissions; the operating cycle of this engine is carried out every two complete revolutions (720°) of the crankshaft, and each phase corresponds to a specific piston movement and valve operation:

1st Half revolution (0-180°) is intake: valve opens at the TDC, allowing a fresh mixture of air and fuel into the cylinder as the piston moves downwards to the BDC. This movement creates a vacuum that draws the mixture into the cylinder [61], [62].

2nd Half revolution (180°-360°) is compression: With the piston at the BDC, both valves are closed, and the piston moves upward, compressing the mixture. This increases the temperature and pressure inside the cylinder, setting the stage for efficient combustion [61], [62].

3rd Half revolution (360°-540°) is expansion: Upon completing one crankshaft rotation, the spark ignites the compressed mixture at the TDC. The combustion rapidly increases pressure, driving the piston downward to the BDC. This is the only phase where the engine performs work necessary for the other cycle phases [61], [62].

4th Half revolution (540°-720°) is exhaust: As the piston reaches the BDC, the exhaust valve opens, allowing the burnt gases to escape at high speeds. The upward movement of the piston clears the burnt gases from the cylinder, completing the cycle as the piston reaches the TDC [61], [62].

The sequence of these four phases is illustrated in Figure 4 below, showing the detailed movements and valve operations throughout the cycle.

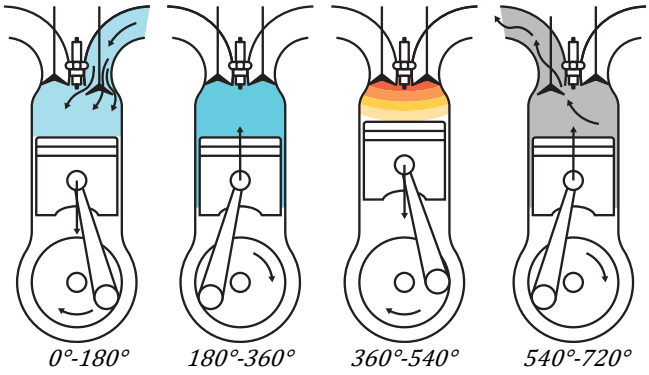

Figure 4 The four phases of a four-stroke engine cycle, adapted from [61].

The valves open and close almost instantaneously for extremely slow engines, coinciding with BDC or TDC. However, for modern fast engines to achieve high air filling in the cylinder during the intake stroke, it is necessary to use the inertial and resonance effects of the gas columns at the cylinder's inlet and outlet (dynamic effects). Thus, the valves remain open longer than the assumed half rotation of the crankshaft. The following explanation details how the engine is commanded and how the valves function [61]

1st Stroke intake: The intake valve remains open during the entire downward stroke of the piston from TDC to BDC and stays open for a short period after BDC. This delay in closing the intake valve ensures that the inertia of the gas column allows the mixture to

continue entering the cylinder during the initial part of the piston's upward movement. Custom designed intake systems can utilize pressure waves to enhance the amount of air entering the cylinder, even with the pressure higher than the intake manifold pressure. The intake valve opens slightly before the piston reaches TDC. This timing leverages the inertia of the exhaust gases and minimizes the risk of them re-entering the intake manifold [61], [62].

2nd Stroke compression: During the compression phase, both valves are closed, and the mixture is compressed as the piston moves upward. This compression increases the temperature and pressure inside the cylinder, setting the stage for efficient combustion [61], [62].

3rd Stroke expansion: Ideally, combustion should occur evenly throughout the piston's downward stroke, starting from TDC. In fact, combustion starts just before TDC, ensuring that the peak pressure and temperature occur just after TDC. This phase is crucial as it provides the energy for the other cycle phases. Ensuring complete combustion as quickly as possible is essential for maximizing efficiency [61], [62].

4th Stroke exhaust: The exhaust valve opens slightly before the piston reaches BDC, expelling the burnt gases. This early opening helps to lower the pressure inside the cylinder, making it easier for the piston to push out the gases. The exhaust valve remains open until slightly after TDC to allow the residual gases to escape, ensuring the cylinder is cleared for the next intake phase. The closing of the exhaust valve is strategically timed to create a slight negative pressure near the valve, aiding the intake of the fresh mixture.

Among other parameters, this difference between the initially presented engine timings and the timing performed by the valves is responsible for the need to differentiate between real and theoretical cycles when studying the thermodynamic cycles in combustion engines. This topic will be revisited in Otto's thermodynamic cycle section where the cycle will be analysed, Figure 5 below illustrates the sequence of these four phases, showing the valve lifting and valve crossing throughout the cycle [61], [62].

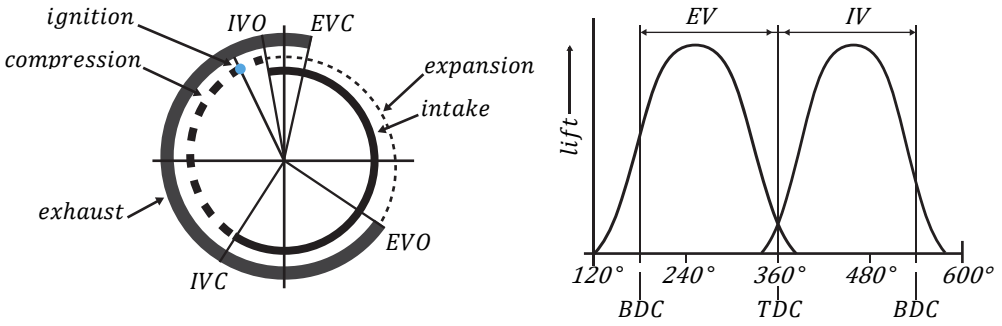

Figure 5 Valve timing and elevation in a four-stroke engine. The left diagram shows intake and exhaust valve phases relative to the crankshaft angle. The right graph shows valve elevation profiles, indicating valve overlap, intake, compression, and exhaust phases, adapted from [61].

2.2.2.3. Eight-stroke cycle

Exploring unconventional engine cycles, such as the six-stroke and eight-stroke configurations, emerged from the ongoing pursuit of improved thermal efficiency and combustion optimization beyond the limitations of conventional two-stroke and four-stroke engines. The six-stroke engine, for instance, enhances combustion efficiency while reducing fuel consumption and emissions[66], [67][68]. Building upon this concept, a novel eight-stroke engine cycle was developed during this study, incorporating dedicated air-only intake and compression strokes to recover residual thermal energy and significantly reduce heat rejection. This innovative cycle represents a new approach to low heat rejection engine design and is the subject of patent application submitted to the Portuguese Institute of Industrial Property. The patented eight-stroke configuration enhances thermal performance and introduces unique dynamic behaviour, particularly in torque generation. Due to its extended cycle and increased complexity, the engine exhibits highly irregular torque output, presenting new challenges for balance and drivability. This study addresses those challenges by using the eight-stroke engine as a representative case for extreme torque irregularity and by proposing solutions, such as the balancing cam mechanism, to mitigate its effects and enable practical implementation of advanced thermodynamic cycles [69].

The eight-stroke cycle offers significant advantages over the two- and four-stroke engines by increasing thermal efficiency by using additional strokes that utilize residual heat. This engine operates similarly to a conventional four-stroke engine but extends the cycle to harness the remaining thermal energy better. The eight-stroke cycle can be divided into two sets of four strokes: the first set operates like a traditional four-stroke engine, while the second set focuses on air-only intake to harness residual heat. The differences

between the second set of four strokes and those of a standard four-stroke engine are as follows [69]:

5th Half revolution (720°-900°) is second intake: The intake valve opens again at TDC, but only air is admitted into the cylinder as the piston moves downward to BDC. This phase uses the existing control system of a 4-stroke engine but fills the cylinder only with air.

6th Half revolution (900°-1080°) is second compression: With the piston at BDC, the intake valve closes, and the piston moves upward, compressing the air. The temperature difference between the cylinder walls and the fresh air increases the pressure and temperature inside the cylinder.

7th Half revolution (1080°-1260°) is second expansion: The compressed air absorbs residual heat from the cylinder walls, expanding and performing additional work as the piston moves downward to BDC. This phase, termed the second power stroke, utilizes residual energy that would otherwise be wasted.

8th Half revolution (1260°-1440°) exhaust: The exhaust valve opens as the piston reaches BDC, allowing the heated air to escape. The piston then moves upward from BDC to TDC, expelling the remaining gases and completing the cycle.

The sequence of these eight phases is illustrated in the Figure 6, showing the detailed movements and valve operations throughout the cycle.

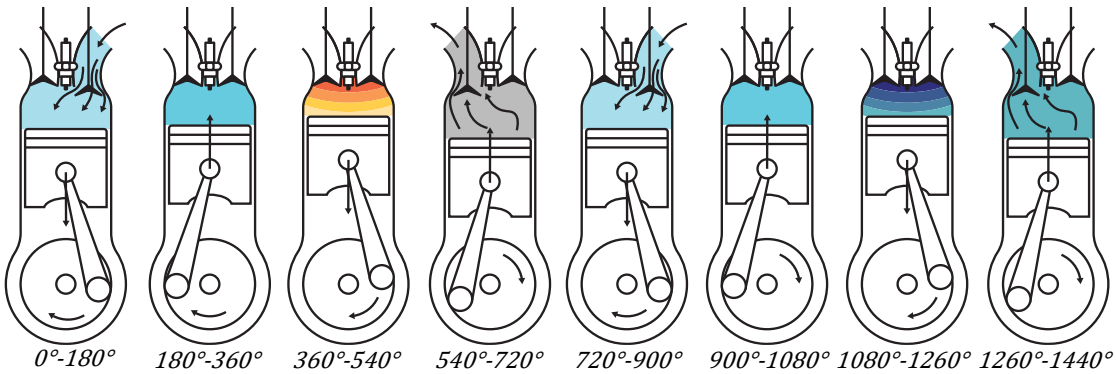

Figure 6 The eight phases of an eight-stroke engine cycle.

The 8-stroke cycle, despite its improved thermal efficiency and reduced specific fuel consumption by incorporating additional strokes to use residual heat, it faces challenges related to low specific power and torque production issues. On the other hand, the two-stroke engine offers higher specific power but suffers from high pollutant emissions and

lower fuel efficiency. For these reasons, and despite the four-stroke engine being the most commonly used working cycle, the 8-stroke engine is gaining attention, mainly when combined with new technologies or specific control systems that will be discussed later in this work. Two-stroke engines, however, still find applications where weight is critical and a high power-to-weight ratio is desired, such as in UAVs, karting competitions, and motocross/enduro bikes.

2.2.3. Thermodynamic cycles

The working cycle and the slider crank mechanism are the main factors determining an engine's torque profile [70]. The thermodynamic cycle significantly influences the produced torque. Subsequent work focuses on the four-stroke Otto cycle, both computationally and experimentally, to make the work more concise.

2.2.3.1. Theoretical Otto cycle

The Otto thermodynamic cycle represents a foundational concept in studying internal combustion engines. Named after Nikolaus Otto, who developed the first successful four-stroke engine, this cycle serves as an idealized model to understand the fundamental principles of how engines convert thermal energy into mechanical work. The Otto cycle consists of four main processes: isentropic compression, isochoric combustion, isentropic expansion, and isochoric exhaust. These processes describe how a fuel-air mixture is compressed, ignited, expanded to perform work, and finally expelled [44], [59], [61], [62], [71], [72].

These processes can be analysed in Figure 7 and described in a cyclical way from:

0-1 - Isobaric intake: The engine draws in a fuel-air mixture at constant pressure.

1-2 - Isentropic compression: The mixture is compressed without heat exchange with the surroundings, increasing pressure and temperature inside the cylinder.

2-3 - Isochoric combustion: Heat is added at constant volume from an external source, representing the combustion process.

3-4 - Isentropic expansion: The high-pressure gases expand, pushing the piston down and performing the work that powers the engine and other processes. This phase occurs without heat exchange with the surroundings.

4-1 - Isochoric exhaust: The exhaust valve opens, releasing the residual heat and gases to the environment at constant volume.

1-0 - Isobaric exhaust: The exhaust gases are expelled at constant pressure.

The theoretical-ideal Otto cycle described above involves several simplifications to effectively model the engine cycle and determine the theoretical thermal efficiency based on the compression and specific heat ratios. These simplifications assume no losses in any of the processes like demonstrated on Figure 7.

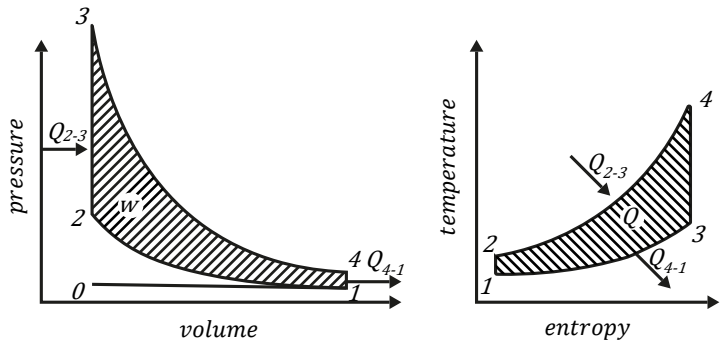

Figure 7 Diagram (p-V) and (T-s) of the theoretical Otto cycle, adapted from [61].

2.2.3.2. Real Otto cycle

Deviations from the ideal cycle occur due to heat losses, pumping losses, non-instantaneous combustion, and valve command. These deviations can be represented on a pressure-volume (p-v) diagram illustrated in Figure 8 resulting in a practical cycle that deviates from the theoretical model and are described by the following processes [44], [59], [61], [62], [71], [72]:

A - Non-isentropic compression and expansion: Energy degradation and heat transfer occur between the working fluid and its surroundings during these processes.

B - Non-isochoric combustion: Combustion is neither isochoric nor instantaneous, requiring spark ignition before the piston reaches TDC to allow time for combustion.

C - Non-instantaneous and non-isochoric exhaust: The exhaust valve opens before the bottom dead centre BDC to facilitate pressure drop and match the cylinder pressure with the external pressure.

D - Non-ideal intake and exhaust: The intake and exhaust processes are not truly isobaric, with losses occurring due to fluid pumping into and out of the cylinder and the non-instantaneous opening of intake and exhaust valves.

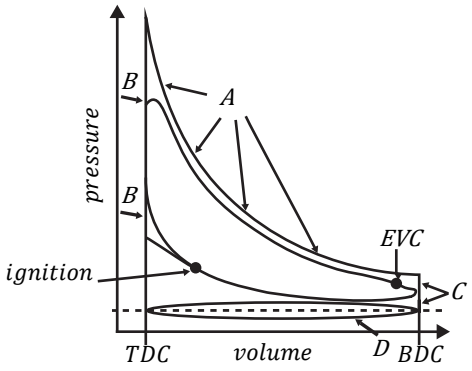

Figure 8 Real Otto cycle superimposed on the theoretical Otto cycle in the (p-v) diagram, adapted from [61].

Figure 9 observes the pressure diagram as a function of the crankshaft angle presented for a 4-stroke engine. The p-v diagram of the real cycle can be converted into this pressure versus crankshaft angle diagram. This conversion allows an analysis of pressure variation throughout the entire cycle and aids in understanding the average behaviour of gases inside the cylinder. It also helps to identify phases of useful work and consumed work, as well as to understand the loads imposed on the moving parts and bearings of the crankshaft, providing a better insight into the dynamic behaviour of these components to define the engine torque profile.

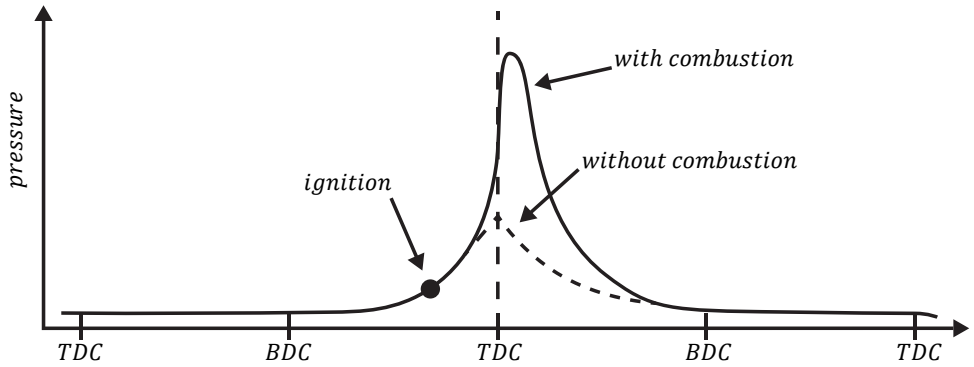

Figure 9 Pressure diagram as a function of the crankshaft angle, adapted from [61].

2.3. Instantaneous torque in alternative engines and the technologies involved in its management

2.3.1. Alternative engines torque composition

In ICEs, the output torque at the crankshaft, as illustrated in Figure 10, the torque fluctuation arises mainly from three sources. Firstly, driving torque generated chiefly during the expansion stroke in ICEs leading to irregular driving actuation. This fluctuation is consistent across different crankshaft speeds, depending solely on crankshaft angle θ_{crank} and pressure force $F_{pressure}$. Secondly, fluctuation occurs due to the inertia force from the acceleration α of the imbalanced mass. This type of fluctuation is more pronounced at higher speeds as it is proportional to the square of the engine's angular speed ω. Lastly, fluctuating resistive loads, such as those in engine valve systems, impart irregular torque to the camshaft, independent of engine angular speed and related to crankshaft angle [73], [74].

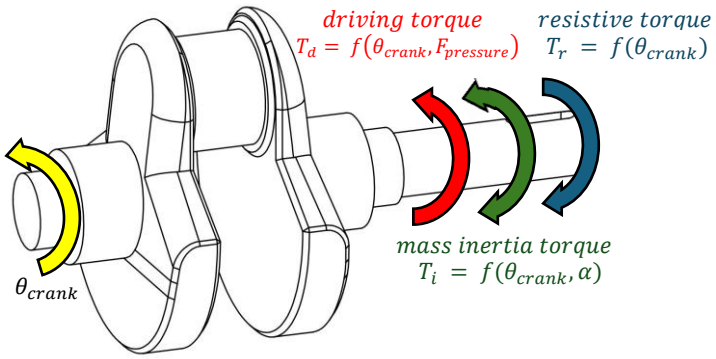

Figure 10 Representation of how the 3 types of torque mentioned above act on the crankshaft.

The analysis of the torque production cycle in internal combustion engines is often conducted using a single-cylinder engine model to better understand it. This approach effectively isolates three types of torque fluctuations, which are more difficult to discern in multi-cylinder engines due to the overlapping of multiple-stroke events [73].

These events significantly contribute to torque fluctuations and can be categorized into two groups: those that generate positive and negative torque. Only the expansion representing a quarter (on Otto) of the strokes and part of the first group is helpful for the engine's primary purpose. However, the magnitude of this proper stroke at engine full load is about fifteen times greater than the average of the other three strokes. However, despite their negative torque, intake, compression, and exhaust strokes are essential for the engine's cycle.

The torque generated by an engine is a composite of the three types previously described, as outlined in Equation 4. Alternative engines capability to generate torque stems from the slider-crank mechanism, shown in Figure 11. Through dynamic analysis of this mechanism, the engine's inertia and driving torque can be accurately determined.

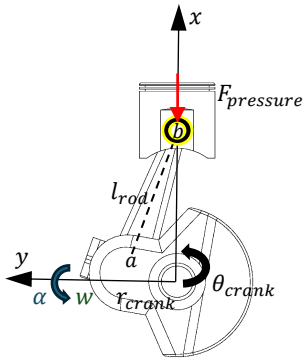

Figure 11 Slider crank mechanism from a single-cylinder engine.

$$T_t = T_d + T_i + T_r \tag{4}$$

$T_t - total\ engine\ torque\ [Nm]$

$T_d - driving\ torque\ [Nm\ ]$

$T_i - inertia\ torque\ [Nm\ ]$

$T_r - resistive\ torque\ [Nm]$

2.3.1.1. Driving torque

ICEs are volumetric machines designed to convert the chemical energy in fuel into mechanical energy, which is then transferred to the crankshaft. They use a slider-crank mechanism to convert pressure from fuel combustion in the combustion chamber into mechanical movement. This is due to the design of the alternative engine, which only allow gases in the cylinder to expand in the piston direction [44], [59], [61], [62], [71], [72].

The force resulting from these pressure can be expressed as the product of the cylinder's internal pressure by the piston area, as shown in Equation 5. This equation illustrates the generation of driving force in ICEs due to pressure, calculated from Equation 6, determined using the first law of thermodynamics.

For a comparative analysis, Figure 12 observes how the values of pressure exerted in the piston can act in the piston when the engine is running at idle, i.e., when the engine only

produces the torque needed to keep it running and when the presence of the flywheel is most necessary to store energy from the expansion stroke for the rest of the strokes, in contrast, Figure 13 derived from an analysis based on Figure 11, culminating in Equation 7, depicts the generation of driving torque throughout a 720° crankshaft rotation in an four strokes Otto engine under identical operational conditions to those shown in Figure 13 [44], [59], [61], [62], [71], [72].

$$F_{pressure} = (p_{cyl} - p_{atm})\,\frac{\pi\, B^2}{4} \tag{5}$$

$$p_{cyl} = \frac{2\left(\delta Q_f - \delta Q - \delta Q_{vap}\right) + p_{cylprev}\left(\frac{\gamma+1}{\gamma-1}V_{cylprev} - V_{cyl}\right)}{\frac{\gamma+1}{\gamma-1}V_{cyl} - V_{cylprev}} \tag{6}$$

$F_{pressure} - pressure\ force\ acting\ on\ the\ piston\ [N]$

$B - bore\ [m]$

$p_{cyl} - cylinder\ pressure\ [Pa]$

$p_{atm} - atmosferic\ pressure\ [Pa]$

$\delta Q_f - energy\ released\ by\ the\ fuel\ [J]$

$\delta Q - energy\ transferred\ in\ the\ form\ of\ heat\ to\ cylinder\ walls\ [J]$

$\delta Q_{vap} - energy\ for\ the\ fuel\ vaporization\ [J]$

$p_{cylprev} - pressure\ in\ the\ cylinder\ at\ the\ previous\ iteration\ [Pa]$

$\gamma - expansion\ coefficient$

$V_{cylprev} - volume\ in\ the\ cylinder\ at\ the\ previous\ iteration\ [m^3]$

$V_{cyl} - volume\ in\ the\ cylinder\ at\ the\ current\ iteration\ [m^3]$

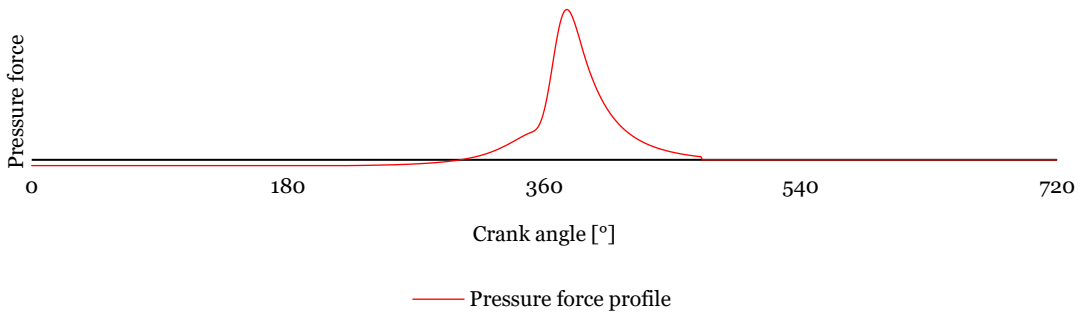

Figure 12 Sketch of $F_{pressure}$ during the four-stroke engine running in an Otto cycle, with the intake process starting at 0°.

$$T_d = F_{pressure} r_{crank} \sin\theta_{crank} \left(1 + \frac{r_{crank}}{l_{rod}} \cos\theta_{crank}\right) \quad (7)$$

$T_d - driving\ engine\ torque\ [Nm]$

$r_{crank} - crank\ radius\ [m]$

$l_{rod} - connecting\ rod\ length\ [m]$

$\theta_{crank} - crankshaft\ rotation\ angle\ [rad]$

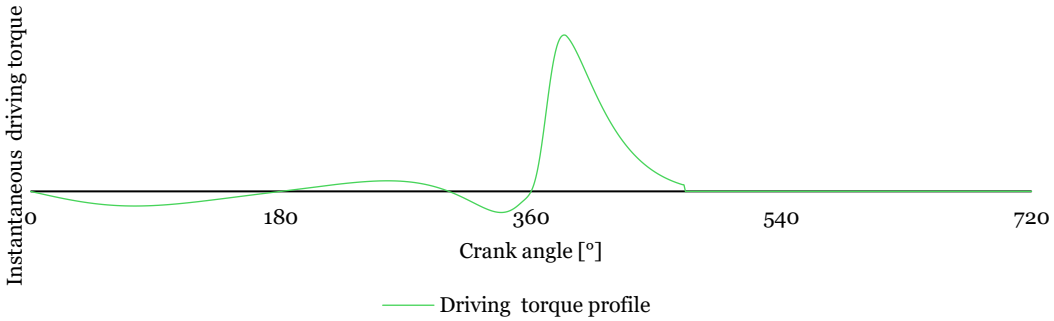

Figure 13 Sketch of driving torque from the $F_{pressure}$ on the slider crank mechanism.

2.3.1.2. Mass inertia torque

Mass inertia torque, referred as inertia torque, arises from the moving parts, particularly during changes in their speed. In the context of an ICE, this involves components like the crankshaft, connecting rods, pistons, and other moving parts. The inertia of these components plays a significant role in the engine's responsiveness, vibrations, and overall performance. Inertia torque is influenced by several factors, including the mass and distribution of the engine's moving parts and the speed. The faster the components rotate, the more significant the inertia torque becomes, as it takes more force to change the speed of these rapidly moving parts. This phenomenon is especially noticed during rapid accelerations or decelerations, where the inertia torque can substantially impact engine performance [75], [76]. The inertia forces can be broken down into components along the piston's movement line (x-axis), which induce forces on the crankshaft and thereby contribute to its torque, presented in Equation 8, and forces acting perpendicularly to the former (y-axis), which do not directly affect the torque generated by the engine, presented in Equation 9. The mass responsible for inducing inertia forces includes the mass of the piston group and the connecting rod. For simplification purposes, this mass is divided between two distinct points: point *a*, located on the crankshaft pin (as shown in Figure 11), where, according to literature,

we can consider as comprising 2/3 of the connecting rod mass, and point b, located on the piston pin, where the piston group mass and 1/3 of the connecting rod mass are assumed, as outlined in Equations 10 and 11 [77].

$$F_{inertia}^{x} = (m_a + m_b) r_{crank} \omega^2 \ cos\ \theta_{crank} + \left(m_b \frac{r_{crank}}{l_{rod}}\right) r_{crank} \omega^2 \ cos\ 2\theta_{crank} \tag{8}$$

$$F_{inertia}^{y} = m_a r_{crank} \omega^2 \ sin\ \theta_{crank} \tag{9}$$

$$m_a = \frac{2}{3} m_{cr} \tag{10}$$

$$m_b = \frac{1}{3} m_{cr} + m_{pg} \tag{11}$$

$F_{inertia}^{x} - inertia\ forces\ on\ x - axis\ [N]$

$m_a - mass\ considered\ at\ point\ a, crankshaft\ pin\ [kg]$

$m_b - mass\ considered\ at\ point\ b, piston\ pin\ [kg]$

$\omega - angular\ velocity\ \left[\frac{rad}{s}\right]$

$F_{inertia}^{y} - inertia\ forces\ on\ y - axis\ [N]$

$m_{pg} - mass\ of\ piston\ group\ [kg]$

$m_{cr} - mass\ of\ connecting\ rod\ [kg]$

To calculate the torque induced by inertia forces on the crankshaft, as detailed in Equation 12, it considers only the masses previously divided and located at point b. This approach is based on the premise that the crankshaft is properly balanced. Such factors in the masses on the crankshaft pin and the equivalent connecting rod mass at point a, ensure that the rotational balance point of this mass aligns with the crankshaft's centre of rotation.

$$T_i = \frac{m_b}{2} {r_{crank}}^2 \omega^2 \left(\frac{r_{crank}}{2l_{rod}} \sin\ \theta_{\text{crank}} - \sin\ 2\theta_{\text{crank}} - \frac{3r_{crank}}{2l_{rod}} \sin\ 3\theta_{\text{crank}}\right) \tag{12}$$

$T_i - mass\ inertia\ torque\ [Nm]$

Inertia effects from the reciprocating components influence both the force and torque experienced by the crankshaft. Figure 14 shows the variation of inertia forces with crank angle. In contrast Figure 15 presents the corresponding instantaneous inertia torque over a full engine cycle, highlighting the periodic nature of these internal dynamics.

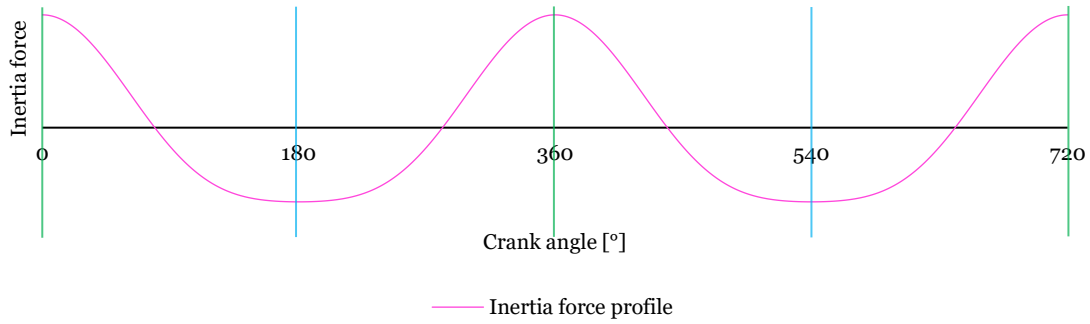

Figure 14 Sketch of the inertia forces on the crankshaft generated by the piston and connecting rod assembly. The vertical green lines indicate the TDC positions, and the blue lines indicate the BDC positions.

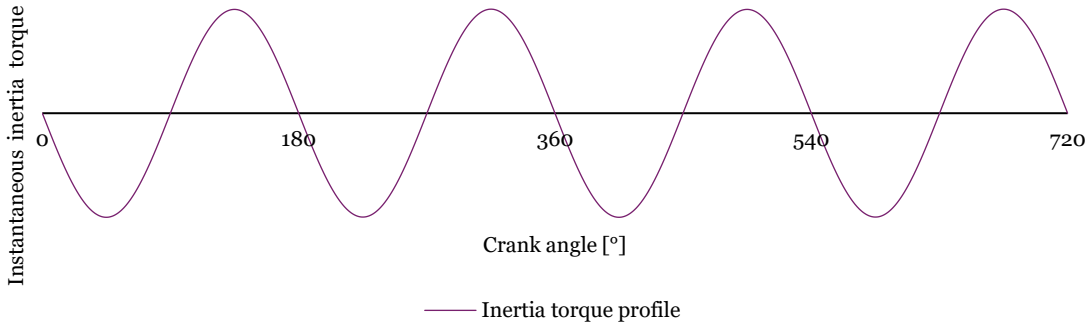

Figure 15 Sketch of instantaneous inertia torque on the crankshaft from internal components in a single-cylinder slider crank engine.

2.3.1.3. Resistive torque

The resistive torque comes from camshafts, oil pumps, friction between parts or other engine auxiliary elements. This torque type is primarily due to resistive forces that the engine components must overcome during operation. In the context of camshafts, this type of torque fluctuates based on the engine cycle, particularly in the valve operation phase, where the opening and closing of valves require varying levels of force. In the camshaft context, the resistive torque results from the need to compress (negative torque) and then release (resulting in positive torque) the valve springs. The magnitude of this torque fluctuation can vary significantly based on the springs' stiffness and the valve mechanism's design. At lower to medium speeds, the resistive torque fluctuation tends to be more substantial than the inertia torque fluctuation. To quantitatively analyse resistive torque in ICEs, one must consider the spring stiffness, the preload force, the rocker mechanism, and the displacement of valves. The spring force from the valve mechanism can be expressed by Equation 13 obtained from the analysis of Figure 16,

resulting in the torque on the camshaft that will be transmitted to the crankshaft through the valve command mechanism [30], [78].

$$F = k\delta + P \tag{13}$$

$k - spring\ stiffness\ \left[\frac{N}{m}\right]$

$\delta - valve\ displacement\ [m]$

$P - preload\ of\ the\ spring\ [N]$

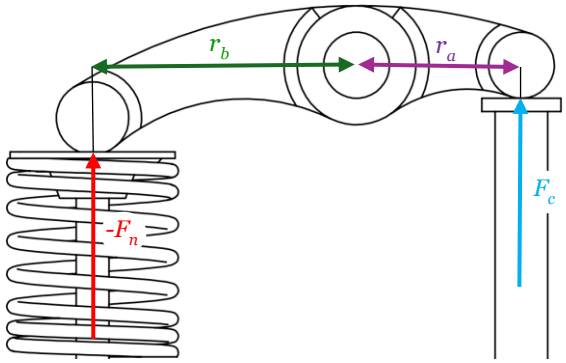

Figure 16 Rocker arm diagram from the valve train.

Equation 14 describes the balance of forces acting on the rocker arm, where F_n and F_c represent the forces exerted by the valve and the cam, respectively. These forces are influenced by the distances r_a and r_b, which are the lengths from the respective pivot points to where the forces are applied. Figure 17 illustrates the force vectors acting on the cam and the corresponding torque on the camshaft.

$$r_a F_c + r_b(-F_n) = 0 \tag{14}$$

$r_a - distance\ from\ the\ push\ rod\ to\ the\ rocker\ centre\ [m]$

$r_b - distance\ from\ the\ valve\ center\ to\ the\ rocker\ centre\ [m]$

$F_n - force\ from\ the\ rocker\ on\ the\ valve\ [N]$

$F_c - force\ from\ the\ cam\ on\ the\ rocker\ [N]$

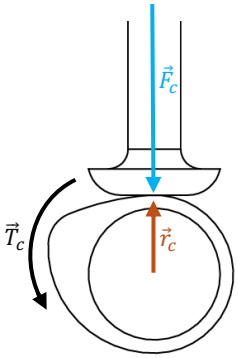

Figure 17 Force vectors acting on the cam and resulting resistive torque on the camshaft during valve operation.

$$\vec{T}_c + \vec{r}_c \times (-\vec{F}_c) = 0 \tag{15}$$

$\vec{T}_c - torque\ on\ the\ camshaft\ [Nm]$

$\vec{r}_c - vector\ from\ the\ center\ of\ the\ cam\ to\ the\ contact\ point\ with\ the\ follower\ [m]$

The interaction of these forces and torques, as described in Equation 15 and depicted in Figure 17, directly influence the resistive torque profiles generated by the intake and exhaust valve mechanisms throughout the engine cycle. Figure 18 illustrates the resulting instantaneous resistive torque profiles for the intake and exhaust valves as a function of the crank angle, showing how the intake and exhaust valves contribute to the overall resistive torque experienced by the camshaft.

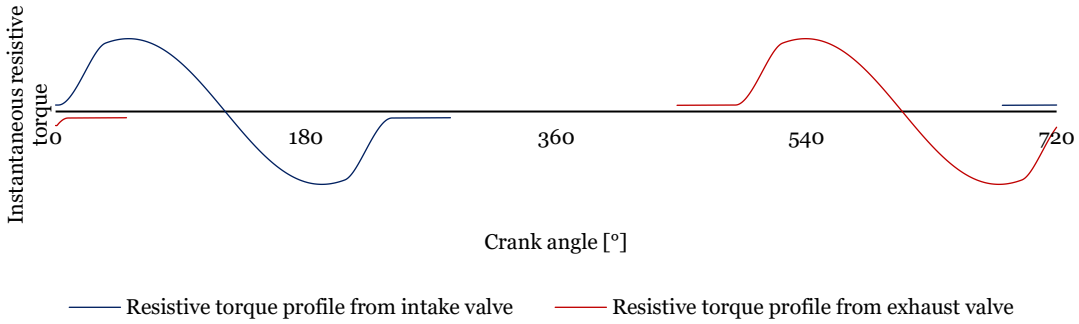

Figure 18 Sketch of resistive torque from intake and exhaust valve mechanism.

Another common source of resistive torque, but essential to the engine's operation, comes from the oil pump. This torque is relatively constant, driven by the need to circulate oil throughout the engine, maintaining lubrication and cooling. It is mainly

independent of the engine's rotational position, though it can vary with engine speed and oil viscosity [79].

In contrast, the resistive torque generated by the splash lubrication system is highly dependent on the crank angle. This system uses an oil dipper attached to the connecting rod, splashes oil onto engine components, providing lubrication. The torque resulting from this system varies sinusoidally, reaching its maximum when the dipper is fully submerged in the oil and dropping to zero when the dipper is out of the oil. This results in a fluctuating resistive torque that opposes the engine's movement at different crank angles [80],[81].

The resistive torque T_{dipper} from the splash lubrication system can be mathematically formulated as follow:

$$T_{dipper} = -\frac{1}{2}\rho\left(\omega r_{crank}\left|sin\left(\frac{\theta_{\text{crank}}}{2}\right)\right|\right)^2 C_d l_{dipper} t_{dipper} r_{crank} \tag{16}$$

$T_{dipper} - oil\ dipper\ torque\ [Nm]$

$\rho\ -\ density\ of\ the\ lubricant\ [kg/m^3]$

$C_d\ -\ drag\ coeficient$

$l_{dipper} - oil\ dipper\ length\ [m]$

$t_{dipper} - dipper\ thickness\ [m]$

Several variables can affect the resistive torque, the density of the lubricant directly influences the drag force experienced by the oil dipper, with a higher density lubricant resulting in a higher resistive torque. The angular velocity of the crankshaft affects the velocity of the oil dipper, where higher angular velocities lead to increased drag forces and, thus, higher resistive torques. The drag coefficient, which depends on the shape and surface roughness of the oil dipper, also plays a crucial role; higher drag coefficients result in greater resistive torques. The length and thickness of the oil dipper contribute to the effective area that interacts with the lubricant; longer and thicker oil dippers increase the resistive torque. Lastly, the crank angle determines the immersion depth of the oil dipper, with the resistive torque varying sinusoidally as the dipper moves through the oil.

The resistive torque profile due to the splash lubrication system can be visualized in Figure 19. This figure represents the resistive torque for a single-cylinder engine during

the 720° of a 4-stroke engine. This torque remains consistently negative, indicating a continuous resistive force opposing the engine's motion.

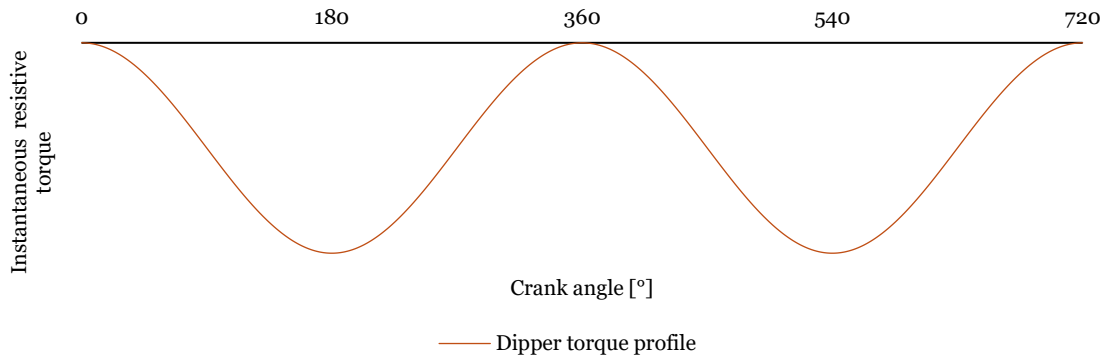

Figure 19 Sketch of resistive torque from a splash lubrication system.

Despite the resistive torque originating from different sources such as lubrication systems or valve trains, the primary sources derive from friction encountered in the crankshaft main bearing, crankpin bearing, and between the piston and cylinder wall. Two distinct friction forces act on the piston: hydrodynamic friction and dry friction. Hydrodynamic friction occurs where the oil film is abundant, while dry friction is observed where the oil film is weak. These friction forces between the piston and cylinder can be defined as follows [77]:

$$F_{horizontal} = F_{pressure} \frac{r_{crank}}{L_{rod}} sin(\theta_{crank}) \left(1 + \frac{r_{crank}^2}{2l_{rod}^2} sin^2(\theta_{crank})\right) \quad (17)$$

$$F_{\mu} = C_{pc} \dot{x} \quad (18)$$

$$F_u = \left|F_{ptangential}\right| \frac{\dot{x}}{|\dot{x}|} \quad (19)$$

$F_{horizontal}$ $-$ *horizontal force exerted by the piston on the cylinder* $[N]$

F_{μ} $-$ *hydrodynamic friction force on the piston* $[N]$

$\dot{x}$ $-$ *piston velocity* $[m/s]$

C_{pc} $-$ *hydrodynamic friction coefficient between the piston and cylinder* $[Nms/rad]$

F_u $-$ *dry friction force on the piston* $[N]$

The piston friction force acts in the opposite direction of piston movement. Here, the signum function is used to continuously adjust the direction of the dry friction force relative to the piston speed. The hydrodynamic friction moments occurring in the conrod bearing and crankshaft main bearing are determined by the following equations [77]:

$$M_y = C_{km}\dot{\phi} \tag{20}$$

$$M_B = C_{cb}\,\dot{\theta}_{crank} \tag{21}$$

M_y $-$ *hydrodynamic friction moment in the conrod bearing* $[Nm]$

$\dot{\phi}$ $-$ *absolute angular speed difference between the crankshaft and the conrod* $[rad/s]$

C_{km} $-$ *coefficient of hydrodynamic friction in the conrod bearing* $[Nms/rad]$

M_B $-$ *hydrodynamic friction moment in the crankshaft main bearing* $[Nm]$

$\dot{\theta}_{crank}$ $-$ *angular speed of the crankshaft* $[rad/s]$

C_{cb} $-$ *coefficient of hydrodynamic friction in the crankshaft main bearing* $[Nms/rad]$

Figure 20 presents the resistive torque resulting from friction forces mathematically formulated by the previously equations. The analysis indicates that a significant portion of this resistive torque arises from the friction between the pistons and the cylinder walls. This friction is directly proportional to both the inertial forces acting on the piston and the forces generated by the pressure exerted within the cylinder.

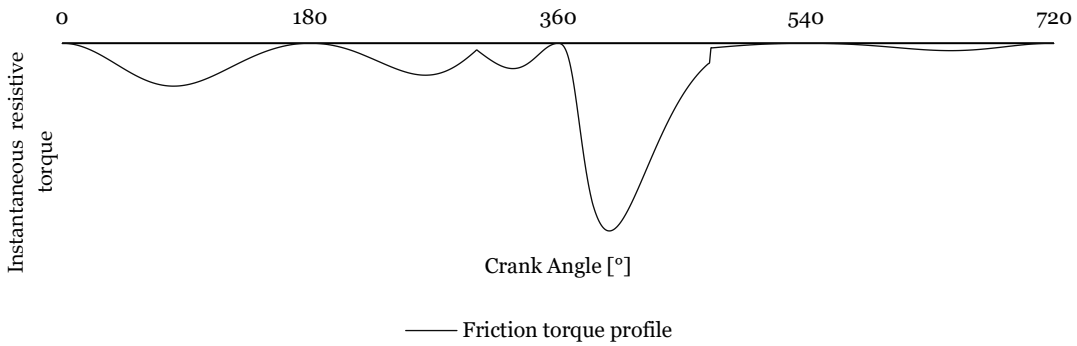

Figure 20 Sketch of resistive torque from the friction between the piston with the walls and the crankshaft bearing.

2.3.2. Instantaneous torque and velocity variations in different working cycles

As previously explained, the decomposition of the adequate torque in an engine reveals that the torque measured at the crankshaft results from the combination of all the torque components mentioned. Figure 21 illustrates the torque at the crankshaft output of a two-stroke engine. Compared to the previously discussed cycles, a clear advantage of this cycle is that it completes its operation within 360° of crankshaft rotation, unlike the 720° required for a four-stroke cycle or the 1440° for an eight-stroke cycle. Consequently, with only one expansion event per 360°, the two-stroke engine exhibits less torque variation

and speed fluctuation, resulting in a higher specific power output, as previously mentioned.

The chart provides a detailed view of the negative torque observed between 0 and 180°, primarily arising from the intake and compression events, with increased emphasis in the last 90° due to the rising pressure inside the cylinder as the intake port is fully closed. From 180° to 360°, the phenomena of combustion initiation, followed by expansion and exhaust, are observed, with a significant variation occurring around 270° when the exhaust port opens, and the gas exhaust process begins. In this cycle, the exhaust pressure is typically managed by using exhaust expansion chambers of various shapes and lengths to enhance engine efficiency. The torque profile presented for the two-stroke engine considers the torque resulting from pressure in the cylinder, the inertia of the internal components, and the resistive torque due to friction. Notably, due to the nature of the cycle, resistive torques arising from the valve mechanism and lubrication system are excluded from this profile, resulting in a more stable torque curve with fewer variations compared to other cycles discussed.

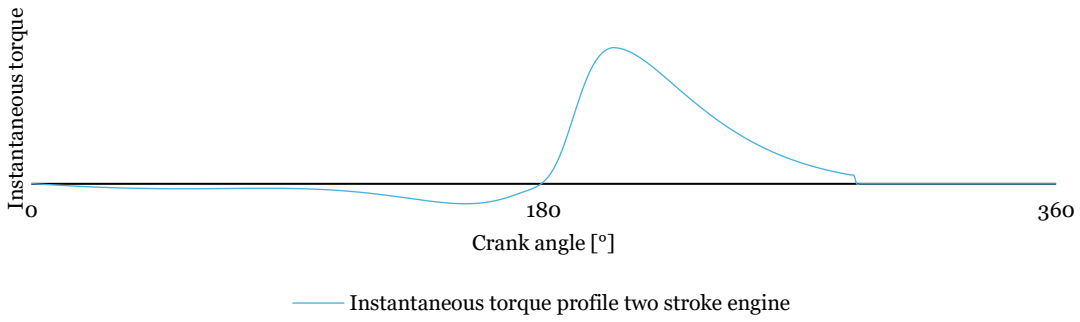

Figure 21 Sketch of instantaneous torque variation along a complete two stroke cycle.

Figure 22 represent the variation in speed over the 360° of the cycle. This variation in speed is analysed similarly to the torque profile discussed earlier. The speed variations are, of course, due to the events that cause fluctuations in torque, as speed variations are inherently linked to these torque changes. Additionally, these variations are influenced by the inertia of the engine's internal components.

Given this context, the introduction of flywheels becomes necessary, as they are essential for adequately operating internal combustion engines. The flywheel is a crucial component for the functioning of any reciprocating engine due to the reasons previously discussed regarding the mechanisms and events that enable the engine to convert the chemical energy of the fuel into mechanical energy [77]. The flywheel, which will be

explained in greater detail in page 47, complements the inertia of the engine's internal components. Its significance is less pronounced in two-stroke engines than four-stroke or eight-stroke engines, as the former completes an entire cycle every 360° of crankshaft rotation despite generally having lower inertia in their internal components.

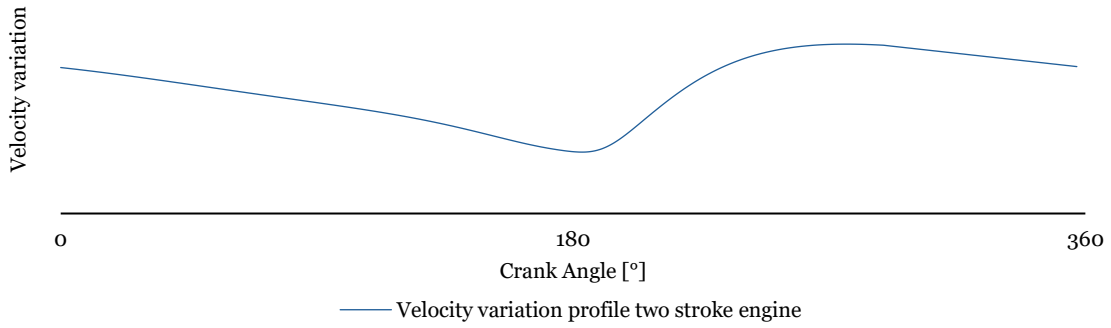

Figure 22 Sketch of velocity variation along a complete two stroke cycle.

In contrast to the two-stroke engine, the four-stroke engine requires 720° of crankshaft rotation to complete an entire cycle. As a result, a four-stroke engine's torque profile exhibits more significant variability than a two-stroke engine due to the working cycle.

Figure 23 illustrates the torque output at the crankshaft for a four-stroke engine. The analysis of this graph reveals the key moments where torque variations occur. Specifically, a negative torque is observed during the intake and compression strokes, which span the first 360° of crankshaft rotation. This negative torque is primarily due to the energy required to draw in the air-fuel mixture and compress it within the cylinder. Additionally, the depression caused by pressure losses in the intake system can further exacerbate the negative torque during the intake stroke as the engine works harder to overcome these losses.

The negative torque peaks towards the end of the compression stroke as the cylinder pressure increases significantly before ignition due to the higher compression ratio compared to the two strokes.

The positive torque is generated during the power stroke, which occurs between 360 and 540° of crankshaft rotation. During this phase, the combustion of the air-fuel mixture leads to rapid expansion, driving the piston downward and producing the maximum torque output.

The exhaust stroke occurs between 540° and 720° of crankshaft rotation following the power stroke. During this phase, a slight negative torque is again observed as the engine expels the exhaust gases. This negative torque is generally less pronounced than that during the intake and compression strokes but still contributes to the overall torque variability; this can be affected by the exhaust system design of the engines, for example, turbo system.

Due to the cyclical nature of the four-stroke engine, with only one power stroke every 720°, the torque profile inherently includes more fluctuations compared to a two-stroke engine. The presence of non-working strokes (intake, compression, and exhaust) introduces periods of negative or reduced torque, contributing to greater torque ripple. As a result, four-stroke engines often require additional components, such as heavier flywheels, to smooth out these fluctuations and maintain a more consistent output.

The torque profile presented for the four-stroke engine in Figure 23 also considers the effects of internal friction and inertial forces, the resistive torque due to friction, including that from the valve train and lubrication system, plays a more significant role in this cycle compared to the two-stroke engine, adding to the overall complexity of the torque characteristics.

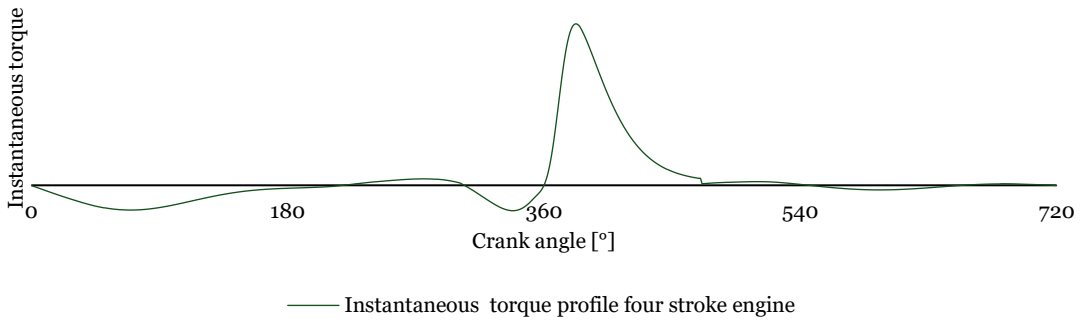

Figure 23 Sketch of instantaneous torque variation along a complete four stroke cycle.

In a four-stroke engine, the speed variation across the 720° of crankshaft rotation reflects the complexity of the engine's operation, which involves the intake, compression, power (expansion), and exhaust strokes. Unlike the two-stroke engine, where speed variations are observed over 360°, the four-stroke engine's extended cycle results in more pronounced and frequent fluctuations in speed, corresponding to the distinct phases of the cycle.

Figure 24 illustrates the variation in speed throughout the 720° cycle of the four-stroke engine. As with the two-stroke engine, these speed variations are intrinsically linked to the torque fluctuations, with each phase of the cycle contributing differently to the engine's speed profile. The intake and compression strokes, which occupy the first 360° of crankshaft rotation, typically result in a decrease in engine speed due to the energy expended to draw in and compress the air-fuel mixture. This decrease is particularly noticeable during the compression stroke, where the rising pressure in the cylinder further resists the piston's upward movement, thereby slowing down the crankshaft.

The power stroke, occurring between 360° and 540° of crankshaft rotation, reverses this trend, with a sharp increase in speed as the combustion of the air-fuel mixture generates a significant amount of energy, propelling the piston downward. This phase corresponds to the peak of the engine's speed variation, where the effective conversion of chemical energy into mechanical work results in a marked acceleration of the crankshaft.

The subsequent exhaust stroke, from 540° to 720°, observes a slight reduction in speed as the engine expels the combustion gases. Although this decrease is less pronounced than during the intake and compression strokes.

Given these speed variations, the role of the flywheel becomes even more critical in a four-stroke engine. This energy buffering effect is essential for maintaining a more consistent engine speed, particularly in the face of the more significant inertia and frictional forces present in four-stroke engines.

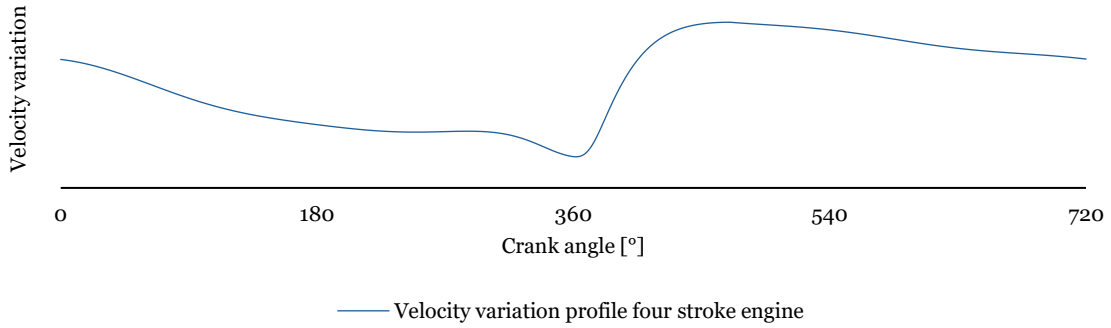

Figure 24 Sketch of velocity variation along a complete four stroke cycle.

Expanding on the analysis of the two-stroke and four-stroke engines, we now focus on the speed and torque variations in an eight-stroke engine cycle, as illustrated in Figure 25 and Figure 26.

Unlike the more conventional two-stroke and four-stroke engines, the eight-stroke engine operates over 1440° of crankshaft rotation, a unique feature that sets it apart. This extended cycle includes two sets of four strokes: the first set consists of the traditional intake, compression, power (expansion), and exhaust strokes, while the second set includes an additional intake of air, followed by compression, a second expansion (utilizing residual heat), and a final exhaust stroke.

Figure 25 illustrates the torque variation throughout the complete eight-stroke cycle. Therefore, there is a significant torque output during both expansion strokes—particularly at approximately 360° and 1080° of crankshaft rotation. The second expansion stroke, occurring after 1080°, as it harnesses the residual thermal energy from the previous cycle, this utilization of residual heat increases the engine's thermal efficiency, compensating for the inherently lower power-to-weight ratio from the eight-stroke cycle.

The torque profile indicates that the engine experiences lower torque levels between these expansion events, particularly during the intake, compression, and exhaust strokes. Resulting in a more complex torque variation pattern than simpler engine cycles.

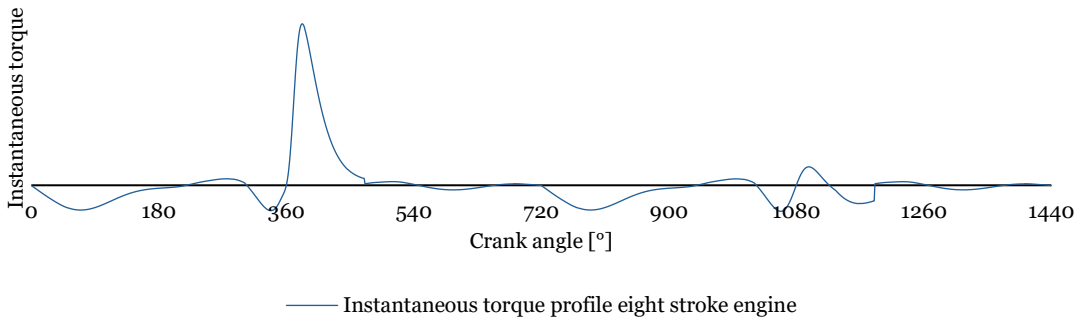

Figure 25 Sketch of instantaneous torque variation along a complete eight stroke cycle.

According to Figure 26, the corresponding speed variation across the 1440° cycle mirrors the torque variations, with two distinct increases in speed corresponding to the two expansion phases. During such phases, the conversion of thermal energy into mechanical work accelerates the crankshaft, leading to peaks in speed. Conversely, during the non-expansion phases, the speed decreases due to the lack of energy input and the resistance encountered during compression and exhaust strokes. Due to the reduced energy output during the second expansion stroke compared to the first, these engines require heavier flywheels to maintain rotational stability.

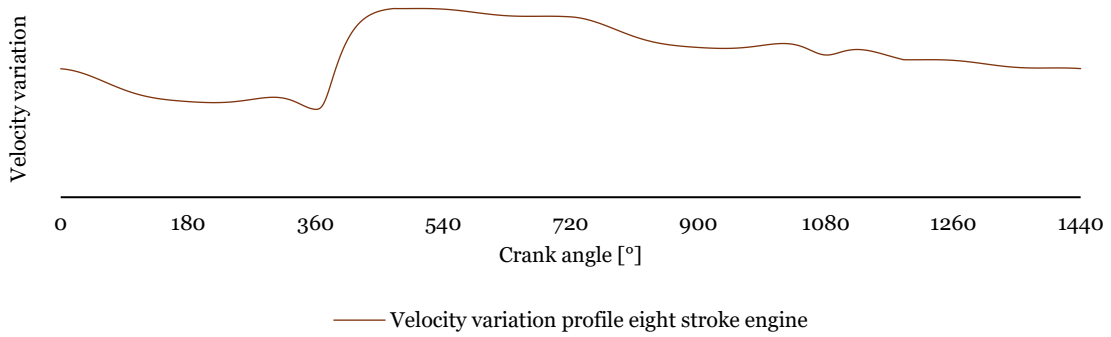

Figure 26 Sketch of velocity variation along a complete eight stroke cycle.

2.3.3. Instantaneous torque and velocity variations in engines with different piston arrangement

The two-cylinder four-stroke engine, combined with its cylinders operating 360° out of phase, presents a unique torque and speed profile compared to single-cylinder configurations. This stage difference ensures that while one cylinder is in its power stroke, the other is undergoing intake, compression, or exhaust, thus providing a more continuous torque output. Figure 27 highlights the torque variation across a complete cycle of this two-cylinder engine. The graph clearly shows the contributions from each cylinder individually, with Cylinder 1 and Cylinder 2 producing torque peaks at approximately 360° and 720° of crankshaft rotation, respectively. The overlap in these power strokes results torque distribution throughout the cycle, significantly reducing the severity of torque dips that would be more pronounced in a single-cylinder engine.

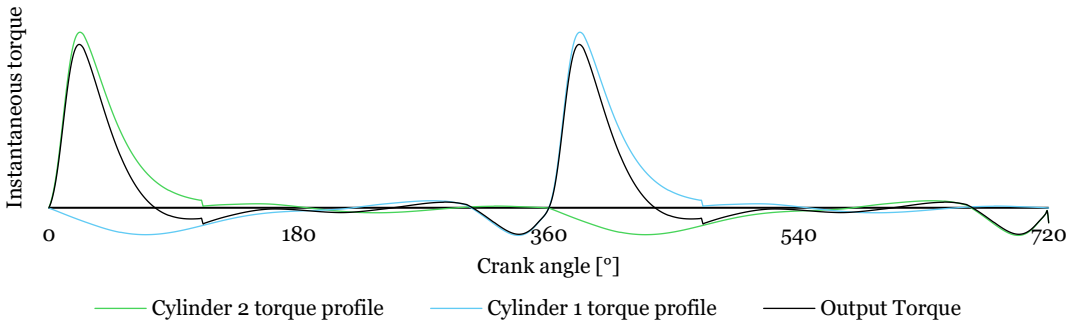

Figure 27 Sketch of instantaneous torque variation along a complete cycle of a two-cylinder engine with 360° of mismatch.

This overlap benefits result in a smooth torque profile by filling in the gaps left between the power strokes of the individual cylinders. While there are periods where neither

cylinder is in its power stroke—most notably between 180°- 270° and 540°- 630° the combined torque output remains more stable than a single-cylinder engine. This stability, however, is not absolute, and the engine still experiences some fluctuation, particularly where the power strokes of the two cylinders do not perfectly align.

Figure 28 illustrates the velocity variation over the same cycle, reflects the impact of these torque fluctuations on engine speed. As expected, the speed increases during the power strokes, where torque output is highest, and decreases during the non-power strokes, where the engine faces more resistance, and less energy is converted into mechanical work. The overlap of the power strokes mitigates these speed variations to some extent, but the 360° phase difference means that the engine still experiences notable speed fluctuations.

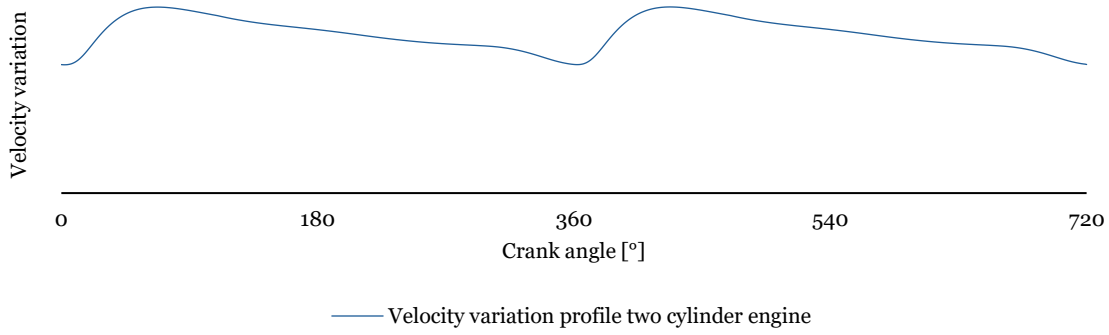

Figure 28 Sketch of velocity variation along a complete cycle of a two-cylinder engine with 360° of mismatch.

The three-cylinder engine, with each cylinder operates 240° out of phase with the others, presents a distinct torque and speed profile compared to two-cylinder and single-cylinder configurations. This phase difference means the power strokes are more evenly spaced throughout the 720° cycle, providing a continuous power delivery.

Figure 29 observes the torque variation from a complete cycle of this three-cylinder engine. Each cylinder contributes to the torque output, with cylinders producing torque peaks at approximately 120°, 360° and 600° of crankshaft rotation, respectively. This staggered timing ensures that as one cylinder completes its power stroke, another begins, resulting in an overlapping torque profile. However, despite this multi-cylinder arrangement, three-cylinder engines tend to experience imbalances in cylinder overlap, particularly noticeable after the expansion process of cylinder 1.

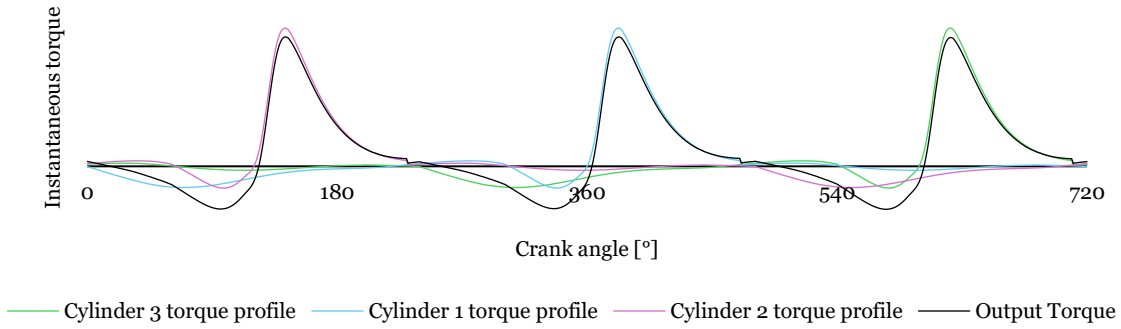

Figure 29 Sketch of instantaneous torque variation along a complete cycle of a three-cylinder engine with 240° of mismatch.

Figure 30 illustrates the velocity variation over the same cycle, reflecting how these torque fluctuations impact engine speed. The speed increases during the power strokes when torque output is at its peak and decreases during the intervals between them.

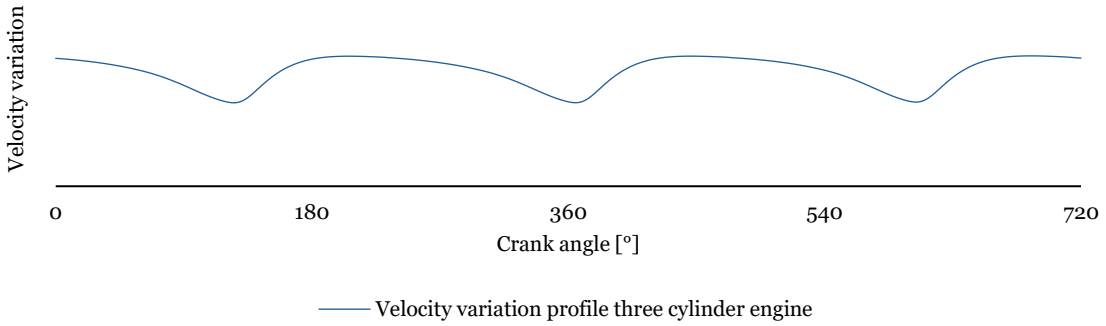

Figure 30 Sketch of velocity torque variation along a complete cycle of a three-cylinder engine with 240° of mismatch.

The four-cylinder, with each cylinder operating 180° out of phase with the others, presents a more refined torque and speed profile than engines with fewer cylinders. This phase difference ensures that the power strokes are more evenly distributed across the 720° cycle, providing a nearly continuous power delivery.

Considering Figure 31, the torque variation from a complete cycle of this four-cylinder engine. Each cylinder contributes to the torque output, with power strokes occurring at 180° intervals. This consistent spacing of power strokes ensures that as one cylinder completes its power stroke, another begins, resulting in an overlapping torque profile that significantly softens the torque curve, providing a reassuringly consistent performance.

This overlap is highly advantageous, as it almost eliminates the torque dips that are more pronounced in mono-cylindric, two-cylinder and three-cylinder engines. The torque peaks from each cylinder blend together, creating a seamless transition between the power strokes, leading to a soft and even torque profile with minimal fluctuations.

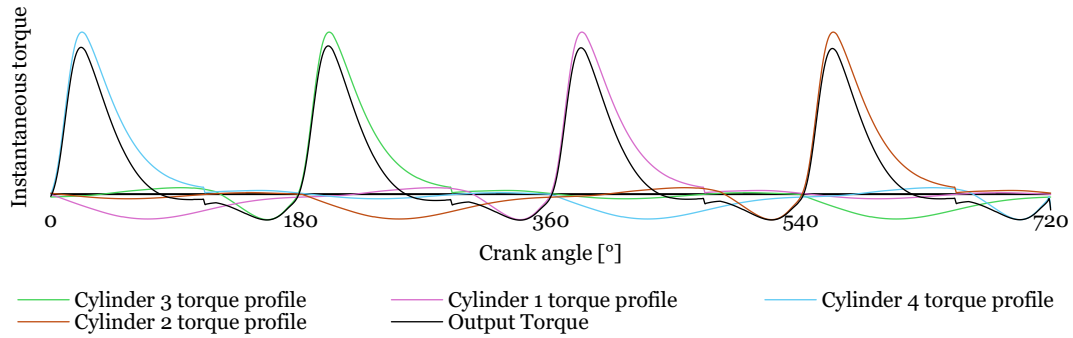

Figure 31 Sketch of instantaneous torque variation along a complete cycle of a fout cylinder engine with 180° of mismatch.

Figure 32 illustrates the velocity variation over the same cycle, reflects how these torque fluctuations impact engine speed. The speed remains relatively steady throughout the cycle, with only minor increases and decreases as the engine transitions between power strokes. These reduced speed fluctuations highlight the inherent stability of the four-cylinder engine. The adequate overlap of torque contributions from each cylinder ensures that the engine speed remains more consistent, contributing to a smooth and reliable operation. While the flywheel in a four-cylinder engine still significantly minimizes residual speed variations, its importance is less pronounced compared to configurations with fewer cylinders, where torque fluctuations are more significant.

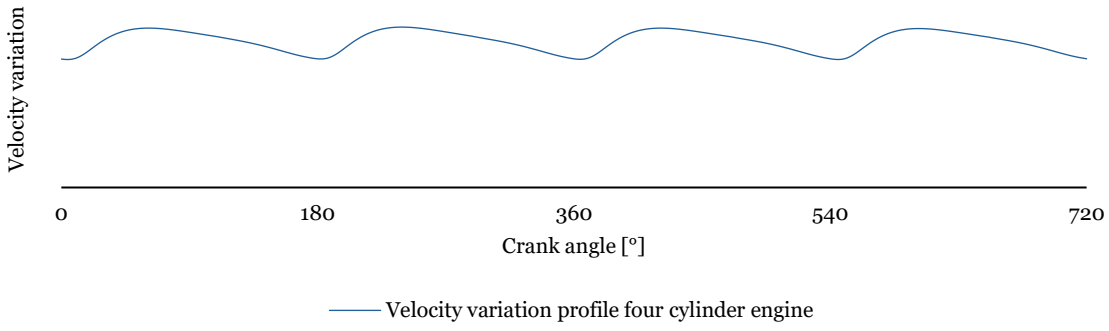

Figure 32 Sketch of velocity variation along a complete cycle of a four-cylinder engine with 180° of mismatch.

Although four-cylinder engines observe the most stable torque and speed variation profiles with minimal oscillations, two or three-cylinder engines are increasingly

replacing them. This shift is driven by the industry's trend toward engine downsizing and the critical relationship between cylinder capacity and thermodynamic efficiency in the ongoing effort to optimize internal combustion engines. The capacity of each cylinder within an engine directly impacts overall performance, with an ideal cylinder capacity of approximately 500 cubic centimetres (cc) being a key focus resulting in this ideal capacity for two, three, and four-cylinder engine configurations. Figure 33, included in this study, visually represents the relationship between cylinder capacity and normalized efficiency across various engine configurations, all with a total displacement of 900 cc.

The size of an engine's cylinders significantly influences its thermodynamic efficiency. A critical aspect of engine design is identifying the optimal cylinder capacity that maximizes efficiency while minimizing heat losses and mechanical friction. It is generally recognized that a cylinder capacity of around 500 cc is optimal, striking a balance that enhances both efficiency and performance [82], [83].

Figure 33 illustrates the trend in normalized efficiency as cylinder capacity increases. The x-axis shows the capacity per cylinder in cc, while the y-axis displays normalized efficiency as a percentage.

The figure highlights three key data points:

- **Two-cylinder engine**: This configuration, with each cylinder having a capacity of approximately 450 cc, exhibits the highest normalized efficiency among the three configurations. The larger cylinder size improves thermodynamic efficiency by minimizing heat losses and allowing the engine to operate closer to optimal thermal conditions.
- **Three-cylinder engine**: In this configuration, each cylinder has a capacity of around 300 cc. The normalized efficiency, while slightly lower than that of the two-cylinder engine, remains competitive. This three-cylinder arrangement offers a more balanced operation, reducing vibration and potentially enhancing mechanical efficiency, though with a modest trade-off in thermodynamic efficiency.
- **Four-cylinder engine**: Each cylinder in this configuration displaces about 225 cc, resulting in the lowest normalized efficiency in this comparison. The smaller cylinder size increases the surface area-to-volume ratio, leading to higher heat losses during combustion and, thus, lower overall efficiency.

As indicated by the green line in Figure 33, it suggests that as the capacity per cylinder increases, normalized efficiency improves. This trend supports the discussion that fewer, larger cylinders (as in the two-cylinder engine) can achieve higher efficiency than configurations with more numerous, smaller cylinders (as in the four-cylinder engine).

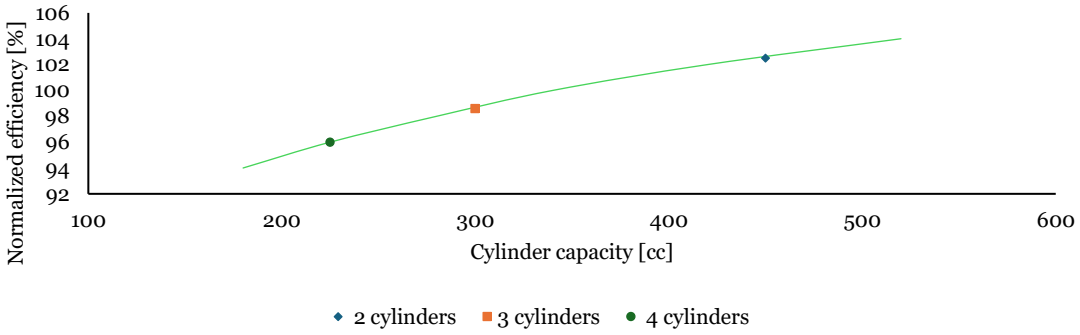

Figure 33 Normalized efficiency versus cylinder capacity for 900 cc engines: two-cylinder, three-cylinder, and four-cylinder, adapted from [82].

2.3.4. Flywheels in alternative engines

Flywheels are energy storage devices that absorb and release kinetic energy to mitigate engine speed fluctuations. By increasing their angular velocity, flywheels store mechanical energy, and by decreasing it, they release this stored energy. This process is particularly useful in stabilizing the energy flow between a power source and its load, such as engines where energy is delivered during only a portion of the cycle [82].

In this investigation, the study of flywheels focuses on understanding their influence on engine dynamics and exploring how they might be optimised or even replaced to improve engine performance. By analysing the impact of flywheels on engine inertia, this research aims to identify strategies to reduce the overall inertia of the engine system. Reducing engine inertia can enhance responsiveness and mitigate the adverse effects of high inertia on engine dynamics, such as slower acceleration and deceleration rates. The objective is to explore alternative methods or technologies to effectively manage energy flow and stabilize engine operation without relying on the traditional heavy flywheel.

Despite their benefits in smoothing energy delivery, flywheels have significant drawbacks. Their large inertia can negatively impact engine performance, particularly in terms of responsiveness to changes in rotational speed. Additionally, including a flywheel represents a notable increase in the engine's overall mass. Beyond automotive applications, flywheels are employed in various energy recovery systems, such as

regenerative braking in electric railways. They are increasingly used to stabilize energy output in renewable energy systems like solar and wind power generation, thanks to advancements in material technology [77].

Figure 34 presents a schematic representation of a flywheel. The flywheel's motion is defined by the angular coordinate θ and characterized by a mass moment of inertia I. An input torque T_i, associated with the coordinate θ_i, results in an increase in the flywheel's rotational speed. Conversely, a load or output torque T_o, related to the coordinate θ_o, extracts energy from the flywheel, causing a speed reduction. If we consider work entering the system as positive and work leaving the system as negative, the equation of motion governing the flywheel can be expressed as [77], [78]:

$$I\alpha = T_i(\theta_i, \omega_i) - T_o(\theta_o, \omega_o) \tag{22}$$

$I\ -\ moment\ of\ inertia\ [kgm^2]$

$\alpha\ -\ angular\ acceleration\ [rad/s^2]$

$T_i(\theta_i, \omega_i)\ -\ input\ torque\ as\ a\ function\ of\ \ \theta_i\ and\ \omega_i\ [Nm]$

$T_o(\theta_o, \omega_o)\ -\ output\ torque\ as\ a\ function\ of\ \ \theta_o\ and\ \ \omega_o\ [Nm]$

$\theta_i\ -\ input\ angular\ position\ [rad]$

$\omega_i\ -input\ angular\ velocity\ [rad/s]$

$\theta_o\ -\ output\ angular\ position\ [rad]$

$\omega_o\ -\ output\ angular\ velocity\ [rad/s]$

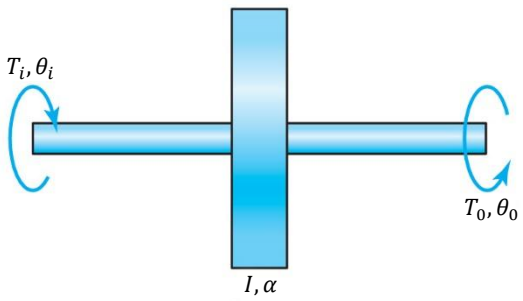

Figure 34 Schematic representation of a flywheel system, adapted from [77].

It is important to note that both T_i and T_o may depend on their respective angular positions, θ_i and θ_o , as well as their angular velocities, ω_i and ω_o. Typically, the torque characteristic is a function of either position or velocity. When the input and output torque functions are known, the equation of motion can be solved to determine the

flywheel's motion. Assuming rigid shafting, the equation consequently simplifies as follows:

$$I\alpha = T_i(\theta, \omega) - T_o(\theta, \omega) \tag{23}$$

When the torque functions and initial values of displacement θ and velocity ω are known, the flywheel's motion can be determined. However, the primary focus often lies in understanding the flywheel's overall performance, including the mass moment of inertia and the system's performance characteristics. To explore this, consider a scenario where a constant input torque T_i is applied as the shaft rotates from θ_1 to θ_2. The energy input to the flywheel during this phase, as illustrated Figure 35, is proportional to the product of the torque and the angular displacement. Similarly, when a constant output torque T_o is applied as the shaft rotates from θ_3 to θ_4, the energy output, also shown in Figure 35, can be calculated. The change in kinetic energy of the flywheel as it transitions from one angular velocity to another is a function of the mass moment of inertia I and the difference in the squares of the angular velocities. To quantify how the speed fluctuates, we define the coefficient of speed fluctuation C_s, which relates the difference in angular velocities to the nominal or average angular velocity. This coefficient is crucial for determining the necessary flywheel inertia to manage the kinetic energy changes in the system. The following equations can substantiate the previous explanation:

$$U_2 - U_1 = \frac{1}{2} I(\omega_2^2 - \omega_1^2) \tag{24}$$

$$C_s = \frac{\omega_2 - \omega_1}{\omega} \tag{25}$$

$$\omega = \frac{1}{2}(\omega_2 + \omega_1) \tag{26}$$

$$U_2 - U_1 = C_s I \omega^2 \tag{27}$$

$U_i - energy\ input\ [J]$

$U_o - energy\ output\ [J]$

$C_s - coefficient\ of\ speed\ fluctuation\ (dimensionless)$

$\omega - nominal\ angular\ velocity\ [rad/s]$

$I - moment\ of\ inertia\ [kgm^2]$

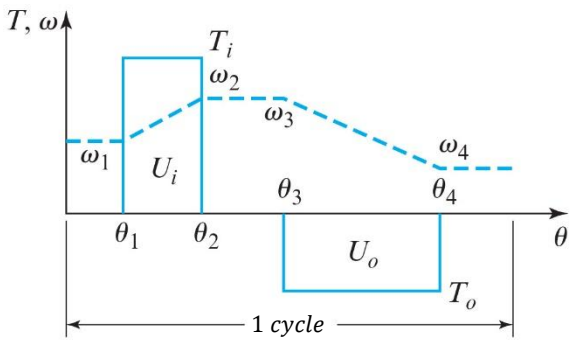

Figure 35 Flywheel torque and angular velocity over one cycle, showing energy input U_i during θ_1 to θ_2 and energy output U_o during θ_3 to θ_4, adapted from [77].

Nowadays, engine development focuses on two key strategies: downsizing and down speeding. Downsizing involves reducing engine capacity, as previously presented, by decreasing the number of cylinders, such as shifting from a four-cylinder to a two-cylinder configuration while maintaining power through advanced techniques like turbocharging and direct injection. Down speeding, on the other hand, aims to achieve peak torque at lower engine speeds, for example, reducing the operating speed from 2500 rpm to 1500 rpm, using technologies such as dual-stage turbocharging. While these strategies improve efficiency by optimizing the engine's operating range, they also increase torque irregularities, which lead to rotational vibrations at the crankshaft. The combination of lower inertia and higher torque at low speeds amplifies these vibrations, transmitting them to the driveline [82].

Several technologies exist to mitigate crankshaft rotational vibrations, which can be categorized into three main types. The first is Active Damping, where an active damper generates a counteracting force to cancel out vibrations, ensuring smooth rotation. While this method is effective, it is costly, requiring an external power source, lacking the reliability for automotive applications. The second is Semi-Active Damping, similar to active damping but with reduced external power requirements, offering a balance between performance and energy consumption. The third is Passive Damping, which relies on a passive system, typically a combination of springs and dampers, to dissipate energy without needing external power. This method is the most cost-effective solution and provides vibration reduction.

A particularly and widely used passive damping solution is the Dual Mass Flywheel (DMF). As illustrated in Figure 36, a standard DMF consists of two masses—a primary mass and a secondary mass—connected through a system of springs and friction washers. The primary mass is securely bolted to the crankshaft and houses the starter

ring gear. In contrast, the secondary mass is connected via a flange that enables efficient torque transfer between the two. This design increases the mass moment of inertia on the gearbox side and aids heat dissipation during clutch operation.

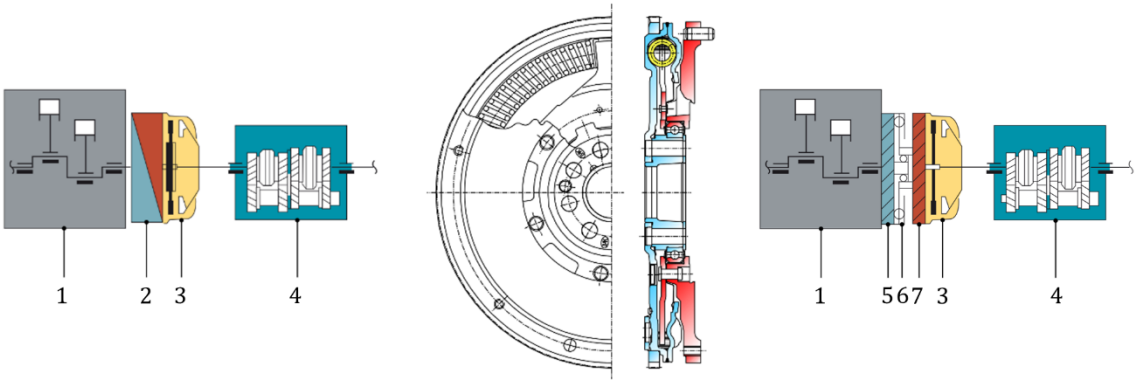

Figure 36 Illustration of a dual mass flywheel system. The left side shows a schematic of a traditional flywheel, the centre presents a cutaway view of a DMF, and the right side depicts a schematic of the DMF. Key components are labelled: 1 – engine; 2 – traditional flywheel; 3 – clutch; 4 – transmission; 5 – primary mass; 6 – torsion damper; 7 – secondary mass.

A dual-mass flywheel features a primary mass directly attached to the crankshaft, forming a coupled inertia essential for maintaining overall stability. Unlike conventional flywheels, the primary mass in a DMF is designed with elasticity, helping to reduce the load on the crankshaft while ensuring smoother engine operation. A key component of the DMF is the arc springs, which are vital for absorbing and dampening vibrations caused by torque fluctuations. These springs work with friction washers and control plates, all aligned sequentially to manage high angular deflections and handle significant loads, such as those experienced during sudden gear engagements [21], [25], [38], [84].

Dual-mass flywheels are widely used in modern engines to mitigate vibrations and enhance driving comfort by isolating torsional vibrations from the drivetrain. However, DMFs have several drawbacks affecting long-term reliability and engine performance.

One of the primary disadvantages of DMFs is their complex design, which can lead to increased maintenance requirements. Components such as arc springs and friction washers are subject to wear over time, especially under high-stress conditions like sudden gear engagement. This wear reduces the DMF's effectiveness, leading to increased vibrations and noise, often necessitating costly repairs or even the replacement of the entire unit.

Additionally, incorporating a DMF into an engine system inherently increases the system's inertia. Although designed to smooth out engine speed fluctuations, the added

mass can negatively impact the engine's overall dynamics. This increased inertia can slow the engine's response to throttle inputs, making the vehicle feel less responsive, particularly in performance-oriented driving conditions. The additional weight also puts more strain on the crankshaft and other engine components, potentially reducing the engine's overall efficiency [85], [86].

Furthermore, the friction washers within the DMF dissipate energy as heat during operation, directly contributing to a reduction in overall efficiency. This energy loss, though necessary for damping vibrations, represents a trade-off, as it reduces the amount of useful energy transmitted from the engine to the drivetrain [87], [88].

2.4. Mechanical actuators

Mechanical actuators are vital for converting hydraulic, pneumatic, and electrical energy into mechanical motion, enabling the efficient operation of various engine systems. The selection and application of these actuators significantly influence the performance of critical engine components, including variable valve timing devices, turbochargers, throttle controls, and fuel injection systems. In this research, mechanical actuators are examined to understand existing engine mechanisms and explore new ones that could support the development of a balancing mechanism to address torque irregularities.

Mechanical actuators are generally classified into four categories: mechanical, hydraulic, pneumatic, and electric. Purely mechanical actuators, a subgroup within this classification, transmit mechanical input into controlled mechanical output without the involvement of hydraulic, pneumatic, or electrical systems. These actuators play a crucial role in engine operation by providing precise control and energy storage through mechanical linkages, springs, cams, and levers [77] [89].

Some primary mechanical actuators utilized in internal ICEs include camshaft actuators, rocker arms, pushrods, and mechanical governors. Camshaft actuators, mainly driven by the crankshaft, have lobes that allow the valves to open and close at precisely the correct times, ensuring consistent engine performance. Rocker arms and pushrods work together to transmit motion from the camshaft to the valves in a typical arrangement, particularly in overhead-valve engines. Mechanical governors, on the other hand, adjust fuel delivery based on changes in centrifugal force within the governor, thereby maintaining a constant engine speed despite variations in load.

Innovative mechanical solutions have also been developed to address vibrations in ICEs, both in translational and rotational contexts. For instance, the centrifugal pendulum vibration absorber is optimised to mitigate vibrations in rotating systems, enhancing the smoothness and stability of engine operation. Additionally, cam-based centrifugal pendulum designs offer active solutions for vibration control and input torque balancing in high-speed machinery, effectively reducing drive speed fluctuations and improving engine stability.

ICEs encounter challenges related to torque fluctuations. These fluctuations can lead to uneven power delivery and increased wear on engine components, making it crucial to address this issue to enhance engine performance and longevity. This study will adopt an approach similar to the one outlined in the study of the balancing cam mechanism to address torque irregularities in the camshaft. The study details a balancing cam mechanism designed to generate a counteracting torque that directly opposes the resistive torque fluctuations experienced by the camshaft. This concept will serve as the foundation for developing a balancing cam mechanism applicable to the entire engine, capable of supporting all the components contributing to the engine's output torque [30].

Unlike traditional methods that rely on external dampers or heavier flywheels, the balancing cam mechanism offers an integrated solution within the engine capable of addressing these fluctuations. Building on the study's findings, this mechanism aims to develop a flexible solution that can be applied across multiple engine types and configurations.

2.4.1. Plate Cam

A cam is a mechanical element that drives a follower, transmitting specific motion through direct contact. In this research, the study of cams, particularly the plate cam, is relevant due to its use in controlling the mechanism developed to address engine torque irregularities. Mechanisms involving cams and followers are widely used for their simplicity, cost-effectiveness, minimal moving parts, and versatility in design [77].

Cams are divided into four classes according to their geometric shapes. The type is shown in Figure 37, including a plate cam—also called a disk cam or radial cam—a wedge cam, a cylindric cam also called a barrel cam and an end cam, or face cam. The wedge cam is much less common because it requires reciprocating instead of continuous input. The most common is the plate cam, which will be considered in this work [78].

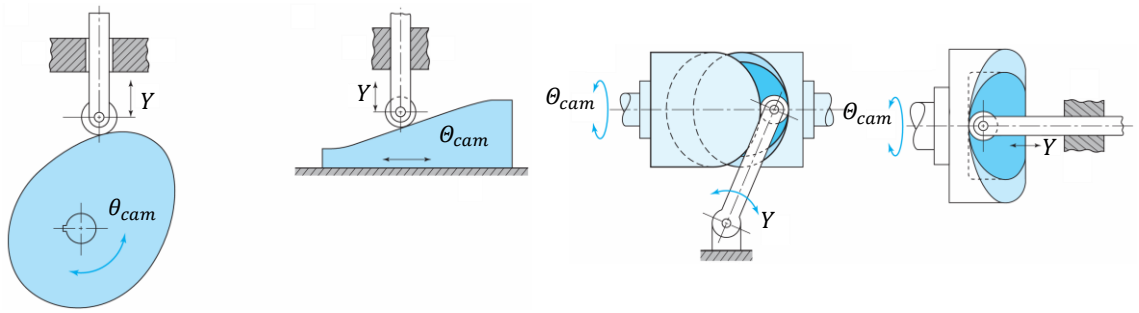

Figure 37 From left to right, plate cam, wedge cam, barrel cam and face cam, adapted from [77].

The cam systems can be further classified by the shape of the follower, as observed in Figure 38. This figure shows how the plate cams operate with several prominent followers in accommodation, such as knife-edged, flat-faced, roller, spheric, or curved-shoe followers. The follower's face is usually of a simple geometric shape, so the cam's profile may be strictly designed to suit the shape. However, in some exceptional cases, like inverse cams, a more complex form is machined into the follower.

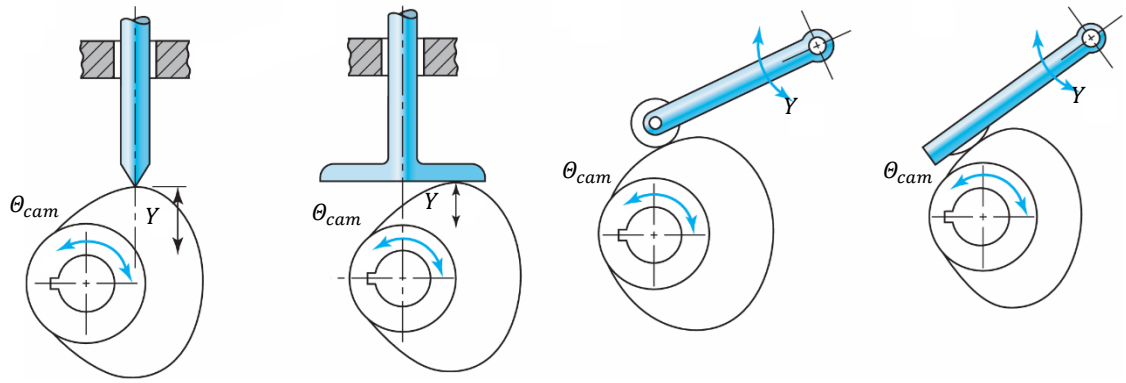

Figure 38 From left to right, plate cams with an offset reciprocating knife-edge follower, a reciprocating flat-face follower, an oscillating roller follower and oscillating curved-shoe follower, adapted from [77].

Cams can also be classified based on the output motion between the follower and the frame. Some cams have reciprocating or translating followers, whereas others produce an oscillating or rotating motion. The follower can oscillate and rotate in its plane, any cam system must be in continuous contact to prevent the loss of contact between the follower and the cam. This can be achieved by several means, such as a proper spring, gravity, or mechanical constraint.

In what follows, we let Θ_{cam} denote the general motion of the cam, and Y denote the general displacement of the follower. In regular cam design, $\Theta_{cam}(t)$ is

given, and Y is the quantity to be determined. Study Figure 37 and Figure 38 to check some standard cam models' definitions of Θ_{cam} and Y. Usually, Θ_{cam} designates an angle for most cams, although it may as well be a distance. Similarly, Y is a translation distance for a reciprocating follower and an angle for an oscillating follower.

A cam and follower system refers to one having a single degree of freedom, driven by a prescribed input motion, usually by a shaft rotating at a constant speed, to deliver a periodic output motion of the follower in a certain way. During one cycle of rotation of a cam, the follower goes through a sequence of events that are usually plotted graphically in the form of a displacement diagram such as the one shown in Figure 39. In the diagram, the horizontal axis is one cycle of input, Θ_{cam} (typically one revolution of the cam) whereas the ordinate is the follower travel, Y. For the reciprocating follower, these diagrams can use the full scale to aid in laying out the follower. Essential features are the *rise*, where the follower moves off the cam centre, and the *return*, where it moves back to the cam centre. Portions where the follower does not move are called *dwells* [77].

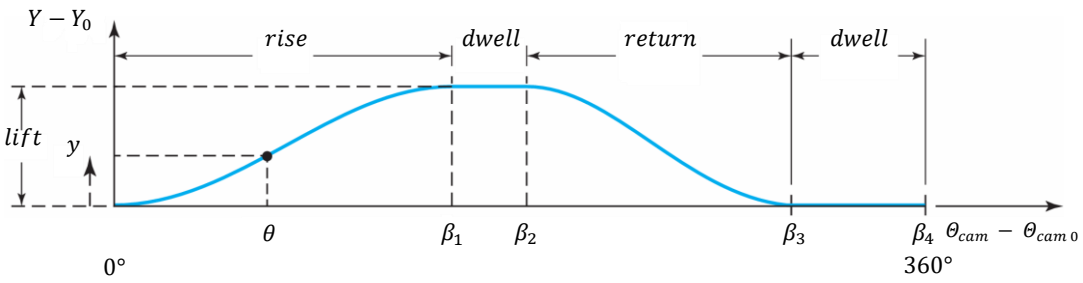

Figure 39 Displacement diagram for a cam, adapted from [77].

For a particular motion segment number z of the total cam, the rotation lies in the range starting with Θ_z and extending by θ within the segment to:

$$\Theta_{z+1} = \Theta_z + \beta_z \tag{28}$$

$z - segment\ number$

$\Theta_z - cam\ rotation\ angle\ at\ segment\ z\ [rad]$

$\beta_z - cam\ angle\ for\ segment\ z\ [rad]$

Similarly, the displacement of the follower is in the range starting from $Y_z + y(0)$ and extending by $y(\theta)$ within the segment to:

$$Y_{z+1} = Y_z + y(\beta_z) \tag{29}$$

Thus, within a single segment, the displacement y is expressed as a function of the cam angle θ:

$$y = y(\theta) \tag{30}$$

These essential features of a displacement diagram total lift, positioning, and duration of dwells are generally specified by application requirements. The follower's motion in a rise and return segment can take several forms; some are more desirable under certain conditions. The most crucial part of cam design is selecting the proper motion profile for these segments of a follower's motion. Once the motions are determined, the relationship between the input Θ and output Y is defined, the displacement diagram may be constructed with complete accuracy as a graphical representation of the functional relationship:

$$Y = Y(\Theta) \tag{31}$$

The characteristic of uniform motion is the displacement diagram in a straight line. The slope of this line is constant, and the velocity of the follower remains constant with a constant input speed. However, due to the sharp corners formed at the junctions with neighbouring segments of a displacement diagram, this is not good for obtaining full lift during motion. Nevertheless, it is extensively used in combination with other curve segments to smooth the sharp corners and represents modified uniform motion [77].

Parabolic motion is a case of modified uniform motion. Here, uniform motion of the central part of the displacement diagram is taken; however, the ends are shaped into a form that results in parabolic motion. This will give constant acceleration to the follower. In order to match the slopes of the parabolic motion with that of the uniform motion, the cam angles and lifts are divided into segments based on the total lift L and the individual lifts. The x-axis and the y-axis are marked off in increments of equal, convenient dimensions and, at each point of the parabola, are drawn in the manner defined.

Cycloidal motion is based upon the geometric curve of a cycloid, which is generated by the rolling of a circle along the ordinate from the origin $y = 0$ to the total lift $y = L$. Since

the circle rolls with no slip, the graph of the vertical displacement y versus the cam angle θ gives the displacement diagram.

The displacement curve for simple harmonic motion is a semicircle with a diameter equal to the segment lift L with the diameters of the semicircle and abscissa divided into some number of equal parts and construction using the method stated.

Considering the case of a plate cam with a radial roller follower, as shown in Figure 40 many essential terms must be defined to understand the process: Trace Point: A point on the follower that is kinematically identified as a theoretical point of contact. Usually, it is assumed to be at the tip of the follower as it would be if it were a knife-edge follower. Usually, it is considered at the centre of a roller follower and along the surface of a flat-faced follower [77].

- Pitch curve: It is the locus of the follower's point of contact when it traverses over the follower's displacement with respect to the cam. In the case of a knife-edge follower, this curve is the cam profile. However, this offset is made from the roller's radius for a roller follower.
- Prime circle: The circle of the smallest radius that can be drawn tangential to the pitch curve at the contacts; centre the axis of the cam.
- Base circle: The smallest circle that can be circumscribed about the cam profile, having its centre coincident with the centre of the cam. In the case of a roller follower or any other kind of follower that requires clearance, the radius of the base circle is decreased by the radius of the follower.

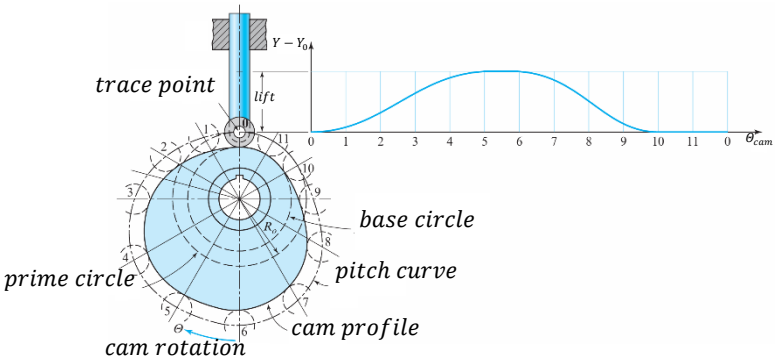

Figure 40 Cam nomenclature, adapted from [77].

While designing the cam profile, the principle of kinematic inversion is used. Considering the working surface as fixed to the cam, and on the rotation of the cam, the follower seems to rotate in the opposite direction concerning this fixed surface. The prime circle

is divided into equal divisions and assigned station numbers. Corresponding graduations on the displacement diagram allow the $Y - Y_0$ displacements to be transferred directly to the cam profile as radial measurements from the base circle to the trace point. Joining these points with a smooth curve generates the pitch curve. In the case of a roller follower, the cam profile is produced as a smooth curve tangent to the position of the roller at each station.

The process for an offset roller follower is different. Hence, an offset circle is constructed with a radius equal to the offset. Stations are numbered around the prime circle. A centreline is constructed tangent to the offset circle at each station. The roller centres for each station are located by transferring $Y - Y_0$ distances from the displacement diagram directly to these follower centerlines. Then, the cam profile is sketched through as a smooth curve tangent to the roller circles.

Each type of cam-and-follower system transfers the displacement diagram into the cam profile using a specific graphic method. From the displacement diagram, the shape of a cam's detail is mainly determined, while factors such as prime circle radius affect the general size of a cam. The shape of a cam is derivative directly from the imposed motion requirements.

2.4.2. Compression Springs

Springs are generally categorized into three primary types: wire, flat, and specially shaped springs. Each category offers variations tailored to specific applications. Wire springs, particularly helical springs made from round or square wire, are extensively utilized due to their ability to resist and deflect under tensile, compressive, or torsional loads. The versatility of wire springs makes them integral to a wide range of mechanical systems. Compression springs are particularly relevant to this work due to their function in storing and delivering energy to the engine according to the cam profile [77].

Understanding the distribution of shear stress is influenced by several factors, including the applied force F, the mean coil diameter D , and the wire diameter d. The spring index C , is a critical parameter that measures coil curvature. A lower spring index indicates a tighter coil, which can increase the stress within the spring. Considering these effects, particularly the non-uniform distribution of stress due to coil curvature, the shear stress-correction factor K_s is applied. This factor is essential for providing a more accurate estimate of the stress, ensuring the reliability and longevity of the spring in its application. The correction is particularly significant when regarding the increased stress

on the inside of the spring wire compared to the outside. These concepts are illustrated in Figure 41 [77].

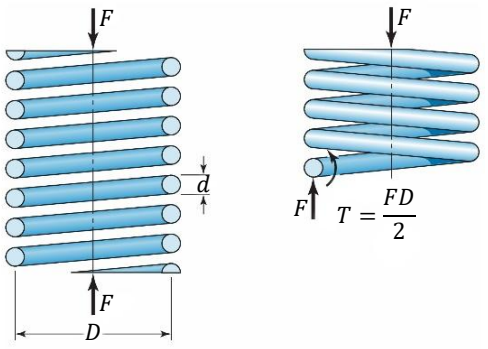

Figure 41 Axially loaded helical spring on left and diagram showing that the wire is subjected to a direct shear and a torsional shear on right, adapted from [78].

Compression springs, widely recognized for their ability to store and release energy efficiently, being used across various industries, from automotive to aerospace. Their performance and reliability are influenced by several design factors, including the type of end configuration, material selection, and manufacturing processes. The ends of compression springs, in particular, play a crucial role in determining their load transfer capabilities and overall performance.

Compression spring ends can be configured in several ways, each affecting the spring's performance. The four common types of ends are plain ends, plain and squared ends, plain and ground ends, and squared and ground ends. Plain ends maintain a continuous helicoid, similar to a long spring cut into sections, and are the simplest type, though they may not offer the best load transfer. Plain and squared ends involve deforming the ends to achieve a zero-degree helix angle, which improves load transfer but still lacks the stability provided by grinding. Plain and ground ends are similar to plain and squared but include additional grinding to ensure a flat surface, offering better load distribution. Finally, squared and ground ends provide the best load transfer, making them the preferred choice in critical applications where stability and precision are paramount [77].

The choice of ending type significantly impacts the spring's performance, particularly in critical applications where load transfer and stability are essential. Springs with squared and ground ends are often selected for superior load transfer capabilities, making them ideal for high-precision environments. The careful selection and design of these end configurations ensure that compression springs can meet the rigorous demands of their

applications, providing reliable performance and durability across a wide range of mechanical systems.

Much like columns under compressive forces, compression springs can experience buckling when subjected to large deflections. The critical deflection y_{cr}, marking the onset of buckling, is a crucial design parameter. This deflection is calculated using specific elastic constants (C_1 and C_2) and the effective slenderness ratio λ_{eff}, which is determined by the spring's geometry and end conditions [77]:

$$y_{cr} = L_0 C_1 \left(1 - \sqrt{1 - \frac{C_2}{\lambda_{eff}^2}}\right) \tag{32}$$

$$\lambda_{eff} = \frac{\alpha L_0}{D} \tag{33}$$

y_{cr} $-$ *critical deflection* $[m]$

L_0 $-$ *free length of the spring* $[m]$

C_1 $-$ *elastic constant*

C_2 $-$ *elastic constant*

λ_{eff} $-$ *effective slenderness ratio*

α $-$ *constant depending on spring's end conditions*

D $-$ *mean coil diameter* $[m]$

Where y_{cr} represents the critical deflection, L_0 is the free length of the spring and λ_{eff} is the effective slenderness ratio; α is a constant depending on the spring's end conditions, and D is the mean coil diameter. These parameters are crucial for predicting and mitigating buckling in compression springs, ensuring their stability and functionality under load.

Material selection directly influencing the tensile strength S_{ut} and torsional yield strength S_{sy} of the spring. The tensile strength, which is the maximum stress a material can withstand while being stretched or pulled before breaking, A and m are material constants, and d is the wire diameter. This equation is vital for determining the material's capability to endure applied forces without failure. The torsional yield strength, approximately 45% of the tensile strength for most spring materials, is estimated by [77]:

$$S_{ut} = Ad^{-m} \tag{34}$$

$$S_{sy} \approx 0.45 S_{ut} \tag{35}$$

S_{ut} $-$ $tensile\ strength\ [Pa]$

S_{sy} $-$ $torsional\ yield\ strength\ [Pa]$

A $-$ $material\ constant\ [Pam^m]$

m $-$ $material\ constant$

The manufacturing process whether hot-working or cold-working significantly impacts a spring's final properties. Cold working is generally preferred for springs with a high spring index, as it induces beneficial residual stresses that enhance performance through strain hardening. These residual stresses improve the spring's resistance to fatigue, making it more durable and reliable in cyclic loading conditions [77].

In cyclic loading, the actual stress experienced by a spring is influenced by factors like coil curvature. Stress correction factors such as the Wahl factor K_W and the Bergsträsser factor K_B are employed to account for this. These factors correct the nominal stress to account for additional stresses due to coil curvature:

$$K_W = \frac{4C - 1}{4C - 4} + \frac{0.615}{C} \tag{36}$$

$$K_B = \frac{4C + 2}{4C - 3} \tag{37}$$

$$C = \frac{D}{d} \tag{38}$$

K_W $-$ $Wahl\ factor$

K_B $-$ $Bergsträsser\ factor$

C $-$ $spring\ index$

d $-$ $wire\ diameter\ [m]$

These correction factors ensure that the calculated stress accurately reflects the actual conditions within the spring, particularly at critical points where failure is most likely to occur. The curvature correction factor K_c can be obtained by combining the B K_B factor with the shear stress-correction factor K_s:

$$K_c = \frac{K_B}{K_s} = \frac{2C(4C+2)}{(4C-3)(2C+1)} \tag{39}$$

K_W $-$ $curvature\ correction\ factor$

K_B $-$ $shear\ stress - correction\ factor$

The maximum shear stress τ in the spring, incorporating this correction, is then given by:

$$\tau = K_B \frac{8FD}{\pi d^3} \tag{40}$$

τ $-$ $shear\ stress\ [Pa]$

F $-$ $applied\ force\ [N]$

Analysing the deflection-force relationships for helical springs involves employing Castigliano's theorem to derive the total strain energy U, which comprises both torsional and shear components:

$$U = \frac{T^2 l}{2GJ} + \frac{F^2 l}{2GA} \tag{41}$$

$$T = \frac{FD}{2} \tag{42}$$

$$l = \pi DN \tag{43}$$

$$J = \frac{\pi d^4}{32} \tag{44}$$

$$A = \frac{\pi d^2}{4} \tag{45}$$

A $-$ $cross - sectional\ area\ [m^2]$

G $-$ $transverse\ modulus\ of\ elasticity\ [pressure]$

N $-$ $number\ of\ active\ coils$

$J - polar\ moment\ of\ inertia\ [m^4]$

To determine the total deflection y of the spring, Castigliano's theorem is applied, resulting in:

$$y = \frac{\partial U}{\partial F} = \frac{8FD^3N}{d^4G}\left(1 + \frac{1}{2C^2}\right) \tag{46}$$

This formulation allows for a more straightforward calculation of the spring rate k, which defines the force required for a unit deflection:

$$k = \frac{d^4G}{8D^3N} \tag{47}$$

Additionally, the solid length L_s of a spring, defined as the length when all coils are fully compressed, can be determined by:

$$L_s = (N_t - a)d \tag{48}$$

L_s $-$ *solid length of the spring* $[m]$

N_t $-$ *total number of coils*

a $-$ *empirical factor*

a is a factor that accounts for the space occupied by the wire when fully compressed, typically averaging around 0.75.

3. Engine torque simulation and experimental validation

3.1. Alternative internal combustion engine simulation

The computational simulation in this study is designed to model the theoretical Otto cycle to calculate cylinder pressure, enabling a detailed analysis of the engine's dynamic behaviour and instantaneous torque. While alternative approaches could have been employed such as applying an experimentally derived or literature-based pressure profile to the crank-connecting rod mechanism the primary objective is to develop a flexible and adaptable tool for research in various areas. This tool is intended to evolve as new variables and parameters are introduced, allowing us to study the effects of engine inertia and the outcomes resulting from changes in this inertia. To ensure the accuracy and reliability of the simulation, the results will be validated by comparing them with both literature data and experimentally obtained results.

Currently, several commercial software tools are available for solving problems related to the design and optimization of ICEs. The main programs used in the automotive industry include Ricardo Wave, Lotus Engine Simulation, and GT-Power [90]. Although these programs have different graphical interfaces, their purposes and functionalities are similar. However, they fall short of the objectives of this work, which seeks to study and decompose the instantaneous torque of an alternative internal combustion engine.

This study focuses primarily on the production and analysing instantaneous torque output from an alternative mechanism throughout the engine cycle. Calculating cylinder pressure is crucial in understanding the dynamic forces acting on the crankshaft, directly influencing the torque output. The pressure data obtained from the simulation allows an examination of the torque fluctuations during different phases of the engine cycle, providing insights into the factors that contribute to irregularities in torque production. Heat transfer phenomena in an ICE are three-dimensional and vary across the entire surface of the cylinder walls, with potential differences between consecutive cycles [91], [92], [93]. The heat flux between the working fluid and the cylinder walls is directly related to energy losses that can negatively affect combustion efficiency and influence the stress distribution across ICE components [94].

Different approaches to engine simulation offer varying levels of complexity and accuracy. Though less precise, zero-dimensional simulations provide satisfactory results related to the engine mechanism with minimal simulation times but often need more

detailed temperature distributions near the top dead centre. Multizone simulations, which include additional geometric parameters, offer more detailed information, particularly regarding thermodynamic effects in the engine. For the most accurate representation of an ICEs behaviour, multidimensional models using computational fluid dynamics tools are employed. These models solve the Navier-Stokes equations with mass and energy conservation laws, providing detailed insights into pressure distribution and torque production. However, the complexity of these simulations leads to significantly longer computation times [94].

3.2. Alternative four-stroke Otto engine modelling

To explore the dynamic behaviour of torque fluctuations in small internal combustion engines, a numerical model was developed and implemented in MATLAB®. The simulation adopts a stepwise crank-angle-resolved approach, advancing in discrete increments of crankshaft rotation to model the complete four-stroke cycle. This methodology allows for high-resolution tracking of thermodynamic and kinematic changes at each stage of the process. While simplified compared to high-fidelity commercial software, this tailored implementation offers a computationally accessible yet detailed foundation for validating torque prediction and evaluating balancing mechanisms. Figure 42 illustrates the simulation structure, providing a flowchart of the algorithm that governs the progression of engine states across each crank angle increment.

The simulation is centred around a single-cylinder 116 cm³ engine, selected for its suitability in validating the computational model and as a foundation for future studies on balancing mechanisms.

The simulation begins with initializing engine geometry parameters, including critical dimensions such as bore, stroke, and connecting rod length. These parameters are essential for accurately representing the engine's physical characteristics. Once the engine geometry is set, the simulation starts by initializing the crank angle θ_{crank} at 0°, incrementally progressing to 720°. This range covers two crankshaft rotations and an additional degree to reset the cycle.

The simulation checks whether the crank angle has reached 720° at each step. If it has reached this mark, the cycle is complete, and the simulation ends. If not, the simulation continues by modelling the slider-crank mechanism, which converts the piston's linear movement in rotational motion into crankshaft's.

The next phase of the simulation involves determining the specific engine phase based on the crank angle. In case the crank angle falls within the range defined by the intake valve opening (IVO) and intake valve closing (IVC) angles, the simulation enters the Intake phase, where the air-fuel mixture is drawn into the cylinder. As the crank angle progresses beyond the intake phase but remains before ignition (IGN), the simulation transitions to the Compression phase, during which the air-fuel mixture is compressed within the cylinder.

Once the crank angle surpasses the ignition point, the simulation enters the Combustion phase, where the compressed air-fuel mixture ignites, generating pressure that drives the piston downward. If the crank angle lies between the expansion and the exhaust valve opening (EVO), the simulation proceeds to the Expansion phase, where the expanding combustion gases perform work on the piston.

Finally, if the crank angle indicates that the engine has entered the exhaust phase, the simulation expels the exhaust gases from the cylinder, thus completing the cycle's sequence of events. After each phase, the simulation calculates the engine torque and the corresponding velocity variation, which is crucial for evaluating the engine's performance characteristics throughout the cycle.

The simulation continues by incrementally increasing the crank angle until it reaches 720°, at which point the process concludes.

This modelling framework enables a structured and transparent evaluation of phase-dependent torque output, offering insight into how transient pressure and piston dynamics influence rotational irregularities. By integrating it within MATLAB®, the model remains flexible for parameter tuning and is easily coupled with experimental datasets. As such, it forms a critical computational foundation for the later development and assessment of the balancing cam mechanism, supporting both design iteration and real-time analysis of the application.

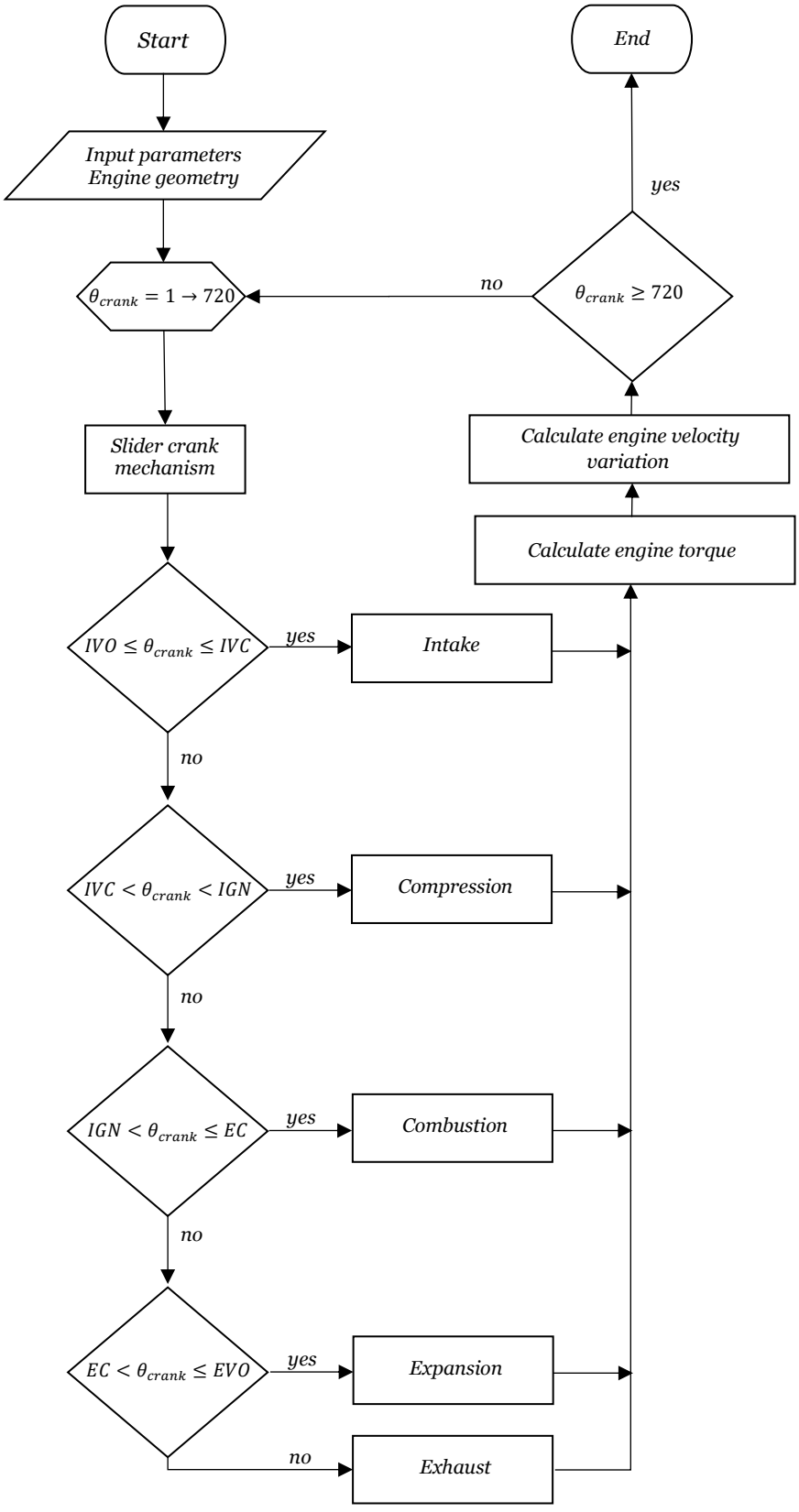

Figure 42 Flowchart of the crank-angle-resolved engine simulation, showing phase detection, torque calculation, and cycle progression from 0° to 720°.

3.2.1. Engine geometry and kinematics

The dynamic behaviour of the piston within a slider-crank mechanism, as depicted in Figure 43, is fundamental to understanding the operation of alternative engines. This mechanism converts the piston's linear motion into the crankshaft's rotational motion. The equations presented below describe the piston's position, velocity, and acceleration during the engine cycle and the torque generated by the slider-crank mechanism [77].

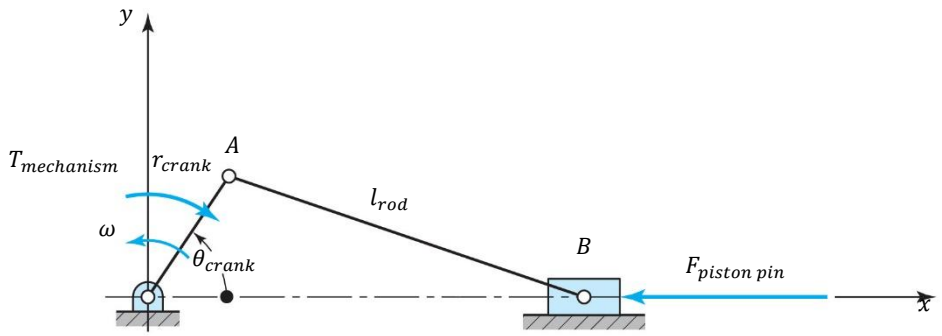

Figure 43 Graphic analysis of slider-crank mechanism, adapted from [77].

The position of the piston x, as shown in Figure 43, can be mathematically expressed by the following equation [77]:

$$x = l_{rod} - \frac{{r_{crank}}^2}{4l_{rod}} + r_{crank}\left(cos\,\theta_{crank} + \frac{r_{crank}}{4l_{rod}} cos\,2\,\theta_{crank}\right) \quad (49)$$

$x - piston\ position\ [m]$

This equation describes the linear position of the piston in relation to the crankshaft's angular displacement.

The velocity $\dot{x}$ of the piston is obtained by differentiating the position equation with respect to time:

$$\dot{x} = -r_{crank}\omega\left(sin\,\theta_{crank} + \frac{r_{crank}}{2l_{rod}}\ sin\,2\theta_{crank}\right) \quad (50)$$

$\dot{x} - piston\ velocity\ [m/s]$

This velocity equation shows how the piston's speed changes during the engine cycle.

The acceleration $\ddot{x}$ of the piston, which is crucial for understanding the forces acting within the engine, is given by:

$$\ddot{x} = -r_{crank}\alpha\left(sin\,\theta_{crank} + \frac{r_{crank}}{2l_{rod}}\,sin\,2l_{rod}\right) - r_{crank}\omega^2\left(cos\,\theta_{crank} + \frac{r_{crank}}{l_{rod}}cos\,2\,\theta_{crank}\right) \quad (51)$$

$\ddot{x}\ -\ piston\ acelaration\ [m/s^2]$

$\alpha\ -\ engine\ acelaration\ [rad/s^2]$

Here, α is the angular acceleration of the crankshaft. This expression provides insights into the dynamic forces acting on the piston, especially under varying engine speeds and loads.

The force $F_{piston\,pin}$, acting on the piston pin, results from the combination of friction forces (calculated as described in section 2.3.1.3), inertia forces, and the pressure applied to the piston. These forces can be expressed in terms of the crankshaft angle. This force directly influences the torque $T_{mechanism}$ generated by the slider-crank mechanism. The torque can be calculated using the following equation, which accounts for the interactions between the forces at the piston pin and the geometry of the slider-crank mechanism [77].

$$T_{mechanism} = F_{piston\,pin}\frac{r_{crank}}{l_{rod}}sin\,\theta_{crank}\left(1 + \frac{{r_{crank}}^2}{2{l_{rod}}^2}sin^2(\theta_{crank})\right)\left[l_{rod} - \frac{{r_{crank}}^2}{4l_{rod}} + r_{crank}\left(cos(\theta_{crank}) + \frac{r_{crank}}{4l_{rod}}cos(2\theta_{crank})\right)\right] \quad (52)$$

$T_{mechanism}\ -\ torque\ resulting\ from\ the\ slyder\ crank\ mechanisn\ \ [Nm]$

$F_{piston\,pin} -\ forces\ acting\ on\ the\ piston\ pin\ \ [N]$

3.2.2. Engine rotational inertia

The engine's dynamic behaviour, particularly its rotational dynamics, is significantly influenced by the moments of inertia of its various components. Understanding these moments of inertia is essential for analysing the engine's performance, particularly how it responds to changes in speed and load. The moments of inertia of different engine components contribute to the total moment of inertia of the engine, which impacts its rotational stability and overall efficiency.

The moment of inertia of the piston, I_{piston}, reflects how the piston's mass influences the engine's rotational dynamics, particularly its impact on the crankshaft system's resistance to changes in rotational speed. In calculating rotational inertia, the piston's mass and its effective radius of rotation are considered, demonstrating the piston's role in the overall inertia of the engine[77], [95].

$$I_{eq.piston} = m_{piston} r_{crank}^2 \left(1 + \frac{1}{2}\left(\frac{r_{crank}}{L_{crod}}\right)^2\right) \quad (53)$$

$I_{eq.piston} - equivalent\ rotational\ inertia\ of\ the\ piston\ at\ the\ crankshaft\ [kgm^2]$

$m_{piston} - mass\ of\ the\ piston\ [kg]$

$l_{crod} - length\ of\ the\ connecting\ rod\ [m]$

This equation demonstrates how the effective moment of inertia associated with the piston's reciprocating motion depends on both its mass and the square of the crank radius. An increase in either parameter results in a higher equivalent moment of inertia, making the engine more resistant to angular velocity fluctuations and contributing to smoother rotational dynamics.

The moment of inertia of the connecting rod, I_{crod}, is more complex because the rod both rotates about the crankshaft and has its own internal mass distribution. It can be calculated by considering the rod's moment of inertia about its centre of mass and applying the parallel axis theorem [95]:

$$I_{crod} = \frac{1}{12} m_{crod} l_{crod}^2 + m_{crod} {r_{crank}}^2 \quad (54)$$

$I_{crod} - moment\ of\ inertia\ of\ the\ connecting\ rod\ [kg\ m^2]$

$m_{crod} - mass\ of\ the\ connecting\ rod\ [kg]$

This formula considers the rotational inertia due to the connecting rod's mass and distribution along its length. Similar to the piston, the connecting rod's inertia increases with its mass and the square of the crank radius. This inertia plays a role in the dynamic forces transmitted through the connecting rod during engine operation.

The crankshaft, as presented in Figure 46, comprises several components that contribute to its moment of inertia: the main shaft, crankpins, crank arms, and counterweights. The moment of inertia for each part is calculated based on its geometry and the material's density, typically steel, instead of using the mass directly.

For the cylindrical segments like the main journal and crankpin [95]:

$$I_{main\ shaft} = \frac{1}{2}\rho\pi r_{main\ shaft}^4 l_{main\ shaft} \tag{55}$$

$$I_{crankpin} = \frac{1}{2}\rho\pi r_{crank\ pin}^4 l_{crank\ pin}$$

$I_{main\ shaft}$ $-$ $moment\ of\ inertia\ of\ the\ main\ shaft$ $[kgm^2]$

$I_{crankpin}$ $-$ $moment\ of\ inertia\ of\ the\ cranckpin$ $[kgm^2]$

ρ $-$ $density\ of\ the\ material$ $[kg/m^3]$

$r_{main\ shaf}$ $-$ $radius\ of\ the\ main\ shaft$ $[m]$

$l_{main\ shaft}$ $-$ $length\ of\ the\ main\ shaft$ $[m]$

$r_{crank\ pin}$ $-$ $radius\ of\ the\ crankpin$ $[m]$

$l_{crank\ pin}$ $-$ $length\ of\ the\ crankpin$ $[m]$

For the crank arms, which are considered rectangular sections:

$$I_{crank\ arm} = \frac{1}{12}\rho wht(w^2 + h^2) + \rho wht r_{crank}^2 \tag{56}$$

w $-$ $width\ of\ the\ crank\ arm$ $[m]$

h $-$ $height\ of\ the\ crank\ arm$ $[m]$

t $-$ $thickness\ of\ the\ crank\ arm$ $[m]$

This equation includes both the inertia of the crank arm about its own centre of mass and its rotational effect about the crankshaft axis.

The counterweights are essential for balancing the rotating assembly. Their moment of inertia is:

$$I_{counterweight} = \frac{1}{12}\rho w_{cw} h_{cw} t_{cw}(w_{cw}^2 + h_{cw}^2) + \rho w_{cw} h_{cw} t_{cw} r_{cw}^2 \tag{57}$$

w_{cw} $-$ $width\ of\ the\ counterweight$ $[m]$

h_{cw} $-$ $height\ of\ the\ counterweight$ $[m]$

t_{cw} $-$ $thickness\ of\ the\ counterweight$ $[m]$

r_{cw} $-$ $distance\ from\ the\ crankshaft\ centerline\ to\ the\ counterweight's\ center\ of\ mass$ $[m]$

The flywheel, designed to smooth out the fluctuations in the engine's rotational speed, has a huge amount of inertia compared to the engine inertia, $I_{flywheel}$, given by [78][95]:

$$I_{flywheel} = \frac{1}{2}\rho\pi\left(t_1 R_1^4 + t_2(R_2^4 - R_1^4)\right) \quad (58)$$

$I_{flywheel} - moment\ of\ the\ flywheel\ [kgm^2]$

$t_1 - thickness\ of\ section\ 1\ [m]$

$t_2 - thickness\ of\ section\ 2\ [m]$

$R_1 - radius\ of\ section\ 1\ [m]$

$R_2 - radius\ of\ section\ 2\ [m]$

The flywheel's moment of inertia is critical for maintaining consistent engine operation, particularly in balancing the energy produced during the power strokes with the energy needed during the other phases of the engine cycle.

Finally, the total moment of inertia of the engine, I_{total}, is the sum of the individual moments of inertia of all these components:

$$I_{total} = I_{piston} + I_{crod} + 2(I_{counterweight} + I_{crank\ arm} + I_{main\ shaft}) + I_{crankpin} + I_{flywheel} \quad (59)$$

$I_{total} - total\ engine\ moment\ of\ inertia\ [kgm^2]$

This total inertia is a key parameter in determining how the engine responds to changes in rotational speed and load. A higher total inertia generally results in a smoother running engine, as it resists rapid changes in speed, contributing to overall stability and efficiency.

3.2.3. Otto cycle modelling

The modelling of the Otto cycle is derived from the analysis of the p-V (pressure-volume) and T-s (temperature-entropy) diagrams of the Otto cycle, as shown in Figure 44. These diagrams depict the key processes of compression, heat addition, expansion, and heat rejection that occur during the engine's operation. The simulation model developed in this study is based on the theoretical principles illustrated in these diagrams [61].

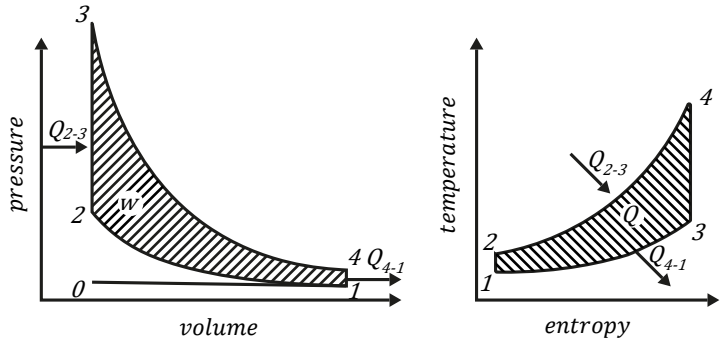

Figure 44 Diagram (p-V) and (T-s) of the theoretical Otto cycle, adapted from [61].

The cycle begins at BDC, the mass of air m_1 in the cylinder is calculated using the ideal gas law [62]:

$$m_1 = \frac{p_1 V_1}{R T_1} \tag{60}$$

$m_1 \; - \; mass \; of \; air \; in \; the \; cylinder \; [kg]$

$p_1 \; - \; initial \; pressure \; [Pa]$

$V_1 \; - \; initial \; volume \; [m^3]$

$R \; - \; ideal \; gas \; constant \; [J/(kgK)]$

$T_1 \; - \; initial \; temperature \; [K]$

And the mass of air trapped in the cylinder m_{air} , can be expressed as:

$$m_{\text{air}} = \frac{p_1 V_{\text{displaced}}}{R T_1} \tag{61}$$

$m_{air} \; - \; mass \; of \; air \; trapped \; in \; the \; cylinder \; [kg]$

$V_{displaced} \; - \; displaced \; volume \; by \; the \; piston \; [m^3]$

Where $V_{displaced}$ is the volume displaced by the piston and R is the ideal gas constant. The mass of fuel trapped m_{fuel} is then determined by:

$$m_{fuel} = \frac{m_{air}}{AFR} \tag{62}$$

$m_{fuel} \; - \; mass \; of \; fuel \; trapped \; [kg]$

$AFR \; - \; air/fuel \; ratio$

Where AFR is the air/fuel ratio conventional SI engines using gasoline as fuel typically operate with an AFR between 12 and 18. To account for variations in the air/fuel ratio, the relative air/fuel ratio λ for SI engines is introduced. Using measured data, the combustion efficiency η_c of gasoline-type fuel can be expressed in this relative air/fuel ratio [62].

$$AFR = \frac{m_{air}}{m_{fuel}} \tag{63}$$

$$\lambda = \frac{AFR}{AFR_{stoich}} \tag{64}$$

$$\eta_c = \eta_{c_{max}}(-1.6082 + 4.6509\lambda - 2.0764\lambda^2) \tag{65}$$

$AFR_{stoich} - stoichiometric\ Air/Fuel\ ratio$

$m_{air} - mass\ flow\ rate\ of\ air\ [kg/s]$

$m_{fuel} - mass\ flow\ rate\ of\ fuel\ [kg/s]$

$\lambda - relative\ air/fuel\ ratio$

$\eta_c - combustion\ efficiency$

$\eta_{c_{max}} - maximum\ combustion\ efficiency$

For λ values between 0.75 and 1.2, the maximum value for $\eta_{c_{\max}}$ is typically 0.9 for SI engines using gasoline fuel [62].

The equations used to describe these relationships are as follows the heat transfer at TDC is equivalent to the heat energy in the fuel, where η_c is the combustion efficiency and QHV is the lower heating value of the fuel:

$$Q_2^3 = \eta_c m_{fuel} QHV \tag{66}$$

$Q_2^3 - heat\ transfer\ at\ TDC\ [J]$

$\eta_c - combustion\ efficiency$

$QHV - lower\ heating\ value\ of\ the\ fuel\ [J/kg]$

The pressure p_2 and temperature T_2 at the end of the compression process, described as an adiabatic and isentropic compression process, are given by [62]:

$$p_2 = p_1 \left(\frac{V_1}{V_2}\right)^{\gamma} \tag{67}$$

$$T_2 = T_1 \left(\frac{V_1}{V_2}\right)^{\gamma-1} \tag{68}$$

$p_2 \; - \; pressure \; after \; compression \; [Pa]$

$V_2 \; - \; volume \; after \; compression \; [m^3]$

$\gamma \; - \; specific \; heat \; ratio$

$T_2 \; - \; temperature \; after \; compression \; [K]$

The work W_1^2 and the change of internal energy $U_2 - U_1$ during the compression are then expressed as:

$$W_1^2 = -m_1 C_v (T_2 - T_1) \tag{69}$$

$$U_2 - U_1 = m_1 C_v (T_2 - T_1) \tag{70}$$

$W_1^2 \; - \; work \; done \; during \; compression \; [J]$

$C_v \; - \; specific \; heat \; at \; constant \; volume \; [J/(kg \cdot K)]$

$U_2 - U_1 \; - \; change \; in \; internal \; energy \; during \; compression \; [J]$

Applying the first law of thermodynamics to the constant volume combustion process, we can obtain p_3 and T_3 describes the heat transfer as [62]:

$$Q_2^3 = U_3 - U_2 + W_2^3 = m_1 C_v (T_3 - T_2) + 0 \tag{71}$$

$$T_3 = T_2 + \frac{Q_2^3}{m_1 C_v} \tag{72}$$

$$p_3 = p_2 \frac{V_2}{V_3} \frac{T_3}{T_2} = p_2 \frac{T_3}{T_2} \tag{73}$$

$$U_3 - U_2 = Q_2^3 \tag{74}$$

$U_3 \; - \; internal \; energy \; after \; combustion \; [J]$

$W_2^3 \; - \; work \; done \; during \; combustion \; [J]$

$T_3 \; - \; temperature \; after \; combustion \; [K]$

$p_3 \; - \; pressure \; after \; combustion \; [Pa]$

$V_3 \; - \; volume \; after \; combustion \; [m^3]$

$U_3 - U_2 \; - \; change \; in \; internal \; energy \; during \; combustion \; [J]$

The pressure p_4 and temperature T_4 at the end of the expansion process, after undergoing an adiabatic and isentropic expansion are given by [62]:

$$p_4 = p_3 \left(\frac{V_3}{V_4}\right)^{\gamma} = \epsilon^{-\gamma} \tag{75}$$

$$T_4 = T_3 \left(\frac{V_3}{V_4}\right)^{\gamma-1} = \epsilon^{1-\gamma} \tag{76}$$

$p_4 - pressure\ after\ expansion\ [Pa]$

$V_4 - volume\ after\ expansion\ [m^3]$

$\epsilon - compression\ ratio$

$T_4 - temperature\ after\ expansion\ [K]$

The work done W_3^4 and the change in internal energy $U_4 - U_3$ during the expansion process are expressed as [62]:

$$W_3^4 = -m_1 C_v (T_4 - T_3) \tag{77}$$

$$U_4 - U_3 = m_1 C_v (T_4 - T_3) \tag{78}$$

$W_3^4 - work\ done\ during\ expansion\ [J]$

$U_4 - U_3 - change\ in\ internal\ energy\ during\ expansion\ [J]$

$Q_4^1 - heat\ rejected\ [J]$

$W_4^1 - work\ done\ during\ heat\ rejection\ [J]$

$U_1 - U_4 - change\ in\ internal\ energy\ during\ heat\ rejection\ [J]$

Finally, the heat rejected during the process of constant volume heat rejection, completing the cycle as given by:

$$Q_4^1 = U_1 - U_4 + W_4^1 = m_1 C_v (T_1 - T_4) \tag{79}$$

$$U_1 - U_4 = Q_4^1 = m_1 C_v (T_1 - T_4) \tag{80}$$

For simulation purposes, the ideal Otto cycle offers limited accuracy; the first step involves incorporating a combustion process that accounts for the fuel burning rate over time to enhance the precision of engine performance predictions. The subsequent improvement in accuracy is achieved by introducing heat transfer losses into the

simulation, thereby deviating from the ideal characteristics of the Otto cycle. As a result, the cycle is no longer considered ideal, with the processes no longer being strictly isentropic and adiabatic.

The engines are modelled as a closed system, where the mass within the system remains constant despite changes in volume, pressure, and temperature; the model assumes that the gas within the cylinder is entirely contained when all valves or openings are sealed and that the piston rings create a perfect seal with the cylinder walls. The volume decreases from V_1 to V_2 during the compression process, and the pressure increases from p_1 to p_2. The piston must perform work to achieve this compression; conversely, if the piston were descending, an expansion process would occur.

When a gas performs work δW within a closed system, it is observed as a change in volume dV under pressure p. This can be mathematically expressed as:

$$\delta W = pdV \tag{81}$$

$\delta W - infinitesimal\ work\ done\ [J]$

$p - pressure\ [Pa]$

$dV - infinitesimal\ change\ in\ volume\ [m^3]$

Using the first law of thermodynamics for a closed system, any work change δW can be related to changes in heat transfer δQ and internal energy dU through the equation:

$$\delta Q = dU + \delta W \tag{82}$$

$\delta Q - infinitesimal\ heat\ transfer\ [J]$

$dU - infinitesimal\ change\ in\ internal\ energy\ [J]$

When these quantities are expressed per unit mass, the specific heat transfer specific δq work δw and specific internal energy du can then be divided by the mass m to derive a specific formulation of the first law of thermodynamics.

$$\delta q = \frac{\delta Q}{m} \tag{83}$$

$$du = \frac{dU}{m} \tag{84}$$

$$\delta w = \frac{\delta W}{m} \tag{85}$$

$$\delta q = du + \delta w \tag{86}$$

$\delta q \ - \ specific\ heat\ transfer\ [J/kg]$

$m \ - \ mass\ of\ the\ system\ [kg]$

$du \ - \ specific\ internal\ energy\ [J/kg]$

$\delta w \ - \ specific\ work\ done\ [J/kg]$

3.2.4. Heat release model

The combustion process can be thermodynamically characterized as a heat addition process within a closed system, occurring in a chamber with a variable volume; the minimum volume in this chamber is defined as combustion chamber volume V_c.

In single-zone models, heat release prediction is typically based on a mass fraction burn curve, often represented by the Wiebe function. This function models the fraction of chemical energy released during fuel combustion as a function of crank angle; the curve follows an S-shape, starting at 0% at the beginning of combustion and reaching 100% at the end, and is mathematically expressed by [44]:

$$\chi_b = 1 - e^{-a_{wiebe}\left(\frac{\theta_{crank}-\theta_{ic\ crank}}{\Delta\theta_{c\ crank}}\right)^{m_{wiebe}+1}} \tag{87}$$

$\chi_b \ - \ mass\ fraction\ burned$

$a_{wiebe} \ - \ Wiebe\ function\ constant$

$\theta_{ic\ crank} \ - \ crank\ angle\ at\ the\ start\ of\ combustion\ [degrees]$

$\Delta\theta_{c\ crank} \ - \ crank\ angle\ duration\ for\ combustion\ [degrees]$

$m_{wiebe} \ - \ Wiebe\ function\ exponent$

Here, $\theta_{ic\ crank}$ is the crank angle at which combustion begins, and $\Delta\theta_{c\ crank}$ is the duration of combustion. The constants a_{wiebe} and m_{wiebe} are determined experimentally, with real burn fraction curves often fitting the Wiebe function using $a_{wiebe} = 5$ and

$m_{wiebe} = 2$ The total heat release during combustion can then be calculated using the following equation:

$$\delta Q = \eta_c(\chi_b - \chi_{b0})m_{\text{fuel}}QHV \tag{88}$$

$\delta Q - heat\ release\ [J]$

$\eta_c - combustion\ efficiency$

$\chi_{b0} - mass\ fraction\ burned\ at\ a\ reference\ point$

$m_{fuel} - mass\ of\ fuel\ [kg]$

$QHV - lower\ heating\ value\ of\ the\ fuel\ [J/kg]$

3.2.5. Heat transfer model

The primary modes of heat transfer in this context include conduction, convection, and radiation. The heat transfer model considered in this study is the Annand model, which is widely recognized as one of the most effective and accurate methods for calculating heat transfer from the cylinder during the closed cycle of a spark-ignition engine. Annand's theory provides an expression for the Nusselt number Nu, which is subsequently used to determine the convection heat transfer coefficient C_h. To correlate the Reynolds number Re with Nu, Annand recommends the expression with $a_{\text{Nu}} = 0.49$ for 4-stroke engines. The Nusselt number is derived from the following equation when the Reynolds number is calculated using the relationship, where B is the cylinder bore. The values of density, mean piston velocity $\overline{V}_p$, and viscosity μ_{gas} can be calculated as described. Once these values are obtained, the convection heat transfer coefficient C_h can be derived from the Nu [62].

$$Nu = a_{Nu} Re^{0.7} \tag{89}$$

$$Re = \frac{\rho_{cyl} \overline{V}_p B}{\mu_{cyl}} \tag{90}$$

$$\rho_{Cyl} = \frac{p_{cyl}}{R T_{gas}} \tag{91}$$

$$\overline{V}_p = \frac{2\ stroke\ \omega_{RPM}}{60} \tag{92}$$

$$\mu_{gas} = 7.457 \times 10^{-6} + 4.1547 \times 10^{-8} T_{gas} - 7.4793 \times 10^{-12} {T_{gas}}^2 \tag{93}$$

$$C_h = \frac{C_k Nu}{B} \tag{94}$$

$Nu\ -\ Nusselt\ number$

$Re\ -\ Reynolds\ number$

$a_{Nu}\ -\ Nusselt\ number\ coefficient$

$\rho_{gas}\ -\ cylinder\ gas\ density\ [kg/m^3]$

$\overline{V}_p\ -\ mean\ piston\ velocity\ [m/s]$

$B\ -\ cylinder\ bore\ [m]$

$\mu_{gas}\ -\ cylinder\ gas\ viscosity\ [Pas]$

$p_{cyl}\ -\ cylinder\ pressure\ [Pa]$

$R\ -\ constant\ of\ perfect\ gases$

$T_{gas}\ -\ cylinder\ temperature\ [K]$

$\omega_{RPM}\ -\ engine\ velociy\ [RPM]$

$C_h\ -\ convection\ heat\ transfer\ coefficient\ [W/(m^2K)]$

$C_k\ -\ thermal\ conductivity\ of\ cylinder\ gas\ [W/(mK)]$

The thermal conductivity of the cylinder gas, denoted as C_k, is assumed to be the same as that of air at the cylinder gas temperature T_{gas} and is calculated based in this assumption. The cylinder wall T_{wall} is typical considered to be the average temperature of the wall, and may be assumed to be 350K. Additionally, Annand also considers the radiation heat transfer C_r to be [62]:

$$C_k = 6.1944 \times 10^{-3} + 7.3814 \times 10^{-5} T_{gas} - 1.2491 \times 10^{-8} {T_{gas}}^2 \quad (95)$$

$$C_r = 4.25 \times 10^{-9} \left(\frac{T_{gas}^4 - T_{wall}^4}{T_{gas} - T_{wall}} \right) \quad (96)$$

$C_k - thermal\ conductivity\ of\ cylinder\ gas\ [W/(mK)]$

$C_r - radiation\ heat\ transfer\ coefficient\ [W/(m^2K)]$

$T_{wall} - cylinder\ wall\ temperature\ [K]$

The heat transfer δQ_L can be calculated over a crankshaft angle interval $d\theta_{crank}$ and a corresponding time interval dt. This calculation provides the mean heat value transmitted to the total surface area exposed to the cylinder gases.

The surface area of the cylinder A_{cyl} includes the areas of the cylinder liner, piston crown, and cylinder head.

The equations corresponding to these concepts are as follows:

$$dt = \frac{60 d\theta_{crank}}{360\ \omega_{RPM}} \quad (97)$$

$$\delta Q_L = (C_h + C_r)\left(T_{gas} - T_{wall}\right) A_{cyl} dt \quad (98)$$

$$A_{cyl} = A_{cylinder\ liner} + A_{piston\ crown} + A_{cylinder\ head} \quad (99)$$

$dt - time\ interval\ [s]$

$d\theta_{crank} - crankshaft\ angle\ interval\ [degrees]$

$C_r - radiation\ heat\ transfer\ coefficient\ [W/(m^2K)]$

$\delta Q_L - heat\ transfer\ [J]$

$A_{cyl} - surface\ area\ of\ the\ cylinder\ [m^2]$

$A_{cylinder\ liner} - surface\ area\ of\ the\ cylinder\ liner\ [m^2]$

$A_{piston\ crown} - surface\ area\ of\ the\ piston\ crown\ [m^2]$

$A_{cylinder\ head} - surface\ area\ of\ the\ cylinder\ head\ [m^2]$

3.2.6. Fuel vaporization model

During the closed cycle of an engine, fuel vaporization occurs, particularly in spark-ignition engines, where this process typically occurs during the compression phase and just before combustion. The interval between the closing of the intake valve and the ignition point is represented by θ_{vap}. It is assumed that fuel vaporization happens

linearly during this interval. The rate at which fuel vaporizes concerning the crank angle denoted as $\dot{m}_{vap}$ can be determined using this assumption. The corresponding heat loss from the cylinder due to fuel vaporization over a specific crankshaft interval, $d\theta$, can be calculated based on this vaporization rate [62].

The following equations apply to this model:

$$\dot{m}_{vap} = \frac{m_{\text{fuel}}}{\theta_{\text{vap}}} \tag{100}$$

$$\delta Q_{\text{vap}} = \dot{m}_{vap} h_{\text{vap}} d\theta \tag{101}$$

$\dot{m}_{vap} - rate\ of\ fuel\ vaporization\ [kg/degree]$

$m_{fuel} - mass\ of\ fuel\ [kg]$

$\theta_{vap} - crankshaft\ angle\ interval\ for\ vaporization\ [degrees]$

$\delta Q_{vap} - heat\ loss\ due\ to\ vaporization\ [J]$

$h_{vap} - latent\ heat\ of\ vaporization\ [J/kg]$

$d\theta - crankshaft\ angle\ interval\ [degrees]$

3.3. Simulation parameters and results

The Honda® GX 120 engine was selected as the basis for the simulation due to its versatility, simplicity of construction, and widespread use in applications ranging from electric power generators to agricultural machinery. This engine will also be used for experimental measurements to validate the simulation results and, subsequently, to incorporate the balancing mechanism to correct the output torque. The engine was disassembled to determine the geometric parameters, allowing for the characterization of its internal components and mechanisms. The parameters used in the simulation are provided in Table 3.

Table 3 Honda® GX 120 engine main geometric characteristics and other simulation parameters.

Parameters	Value
Stroke	$0.0435\ m$
Bore	$0.060\ m$
Crank radius	$0.02175\ m$
Connecting rod length	$0.073\ m$
Piston mass	$0.144\ kg$
Rod mass	$0.123\ kg$
Rocker arm intake	$0.022\ m$
Rocker arm exhaust	$0.022\ m$
Valve spring stiffness	$5.88 \times 10^{-6}\ kN/m$
Valve spring preload	$4.7 \times 10^{-2}\ kN/m$
Engine rotational inertia	$1.254 \times 10^{-3}\ \mathrm{kg}\ m^2$
Flywheel inertia	$1.349 \times 10^{-2}\mathrm{kg}\ m^2$
Compression ratio	8.3
Atmospheric pressure	$101325\ Pa$
Atmospheric temperature	$293.15\ K$
Air-Fuel Ratio	15.03
Intake valve open	0°
Intake valve close	220°
Exhaust valve open	470°
Exhaust valve close	720°
Splash system thickness	$0.003\ m$
Splash system length	$0.043\ m$
Oil density	$895\ \mathrm{kg}\ m^3$

Figure 45 illustrates the rocker arm, piston, and connecting rod. The geometric analysis of these components, along with the crankshaft depicted in Figure 46, helps to determine the slider-crank mechanism and the inertia torque generated by linear forces acting on the crankshaft.

Figure 45 Rocker arm from valve mechanism, piston and connecting rod from Honda® GX 120 engine.

Figure 46 illustrates the crankshaft and flywheel. Building on the previous analysis, the crankshaft transforms the piston's linear motion into rotational motion, while the flywheel maintains a consistent engine speed by storing rotational energy.

Figure 46 Crankshaft and flywheel from Honda® GX 120 engine.

The results obtained from the simulations align with the theoretical foundations discussed earlier. The following figures present graphs that demonstrate the behaviour of the simulation in determining the cylinder pressure within the alternative engine configuration. Figure 47 illustrates the variation of pressure throughout the engine cycle, while Figure 48 shows its relationship with the cylinder volume.

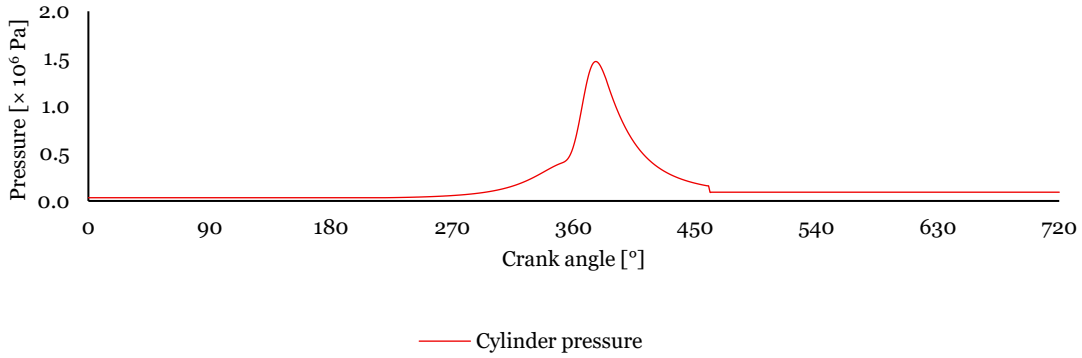

Figure 47 Cylinder pressure as a function of the crank angle, showing the variation of pressure throughout the engine cycle.

The graph in Figure 47 illustrates the variation in cylinder pressure over a complete engine cycle. During the intake stroke (0° to 220°), the pressure dips below atmospheric levels, reaching approximately 0.3×10^5 Pa, as the piston descends, drawing in the air-fuel mixture. In the compression stroke (220° to 360°), the pressure rises to nearly 5×10^5 Pa as the piston compresses the mixture until reaching the top dead centre. In the expansion or power stroke (360° to 470°), combustion leads to a pressure peaking at about 20×10^5 Pa, driving the piston downward. Finally, during the exhaust stroke (470° to 720°), the pressure decreases sharply, dropping from 1.5×10^5 Pa when the exhaust valve opens back to around the atmospheric values as the exhaust gases are expelled.

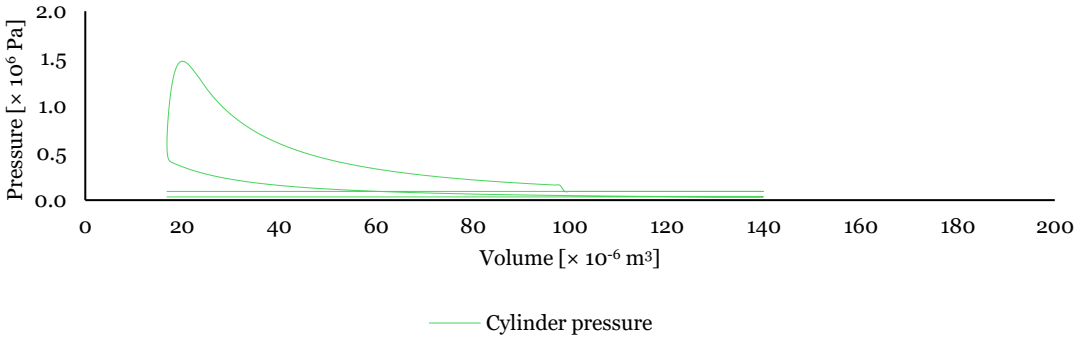

Figure 48 Cylinder pressure as a function of volume throughout the engine cycle.

The graph in Figure 48 outlines the relationship between cylinder pressure and volume throughout the engine cycle. Starting at the maximum volume of approximately 140×10^{-6} m^3, the pressure rises sharply as the volume decreases to around 20×10^{-6} m^3, corresponding to the combustion chamber. After combustion, during the expansion phase, the volume increases as the piston moves downward, causing the pressure to decrease steadily.

Compared to the theoretical Otto cycle, where ideal isentropic compression and expansion curves represent the pressure-volume relationship, the simulated graph shows some deviations. The peak pressure is rounded rather than sharp, reflecting the more realistic combustion process captured in the simulation.

3.3.1. Output torque components

The driving torque generated by an ICE is a direct result of the pressure forces acting on the piston, which are then converted into rotational motion by the crankshaft. Figure 49 reflects the driving torque profile as a function of the crankshaft angle derived from the pressure in the cylinder formulated earlier.

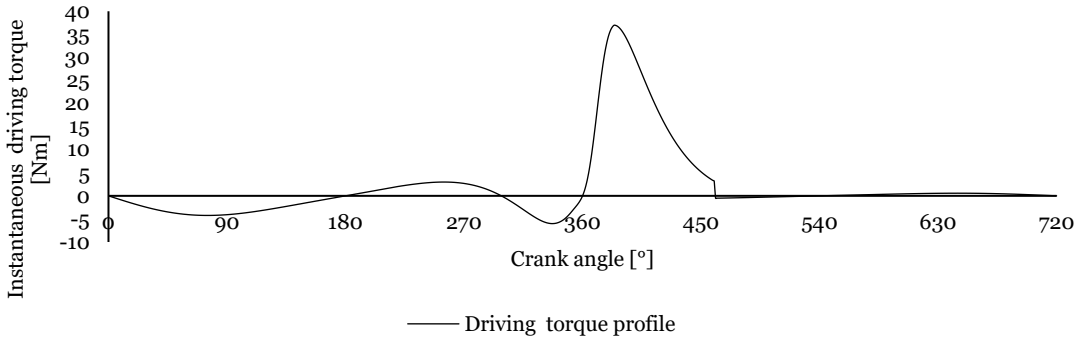

Figure 49 Simulated driving torque profile for the Honda® GX 120 engine, showing the torque generated by cylinder pressure throughout the engine cycle.

Observing the graph in Figure 49, the instantaneous driving torque profile over a complete engine cycle, the torque remains relatively low during the intake and compression strokes, fluctuating between -7 Nm and 3 Nm due to restrictions in the intake process. There is a significant spike around the 360° crank angle, corresponding to the combustion process, with torque peaking at approximately 40 Nm. Following the expansion stroke, the torque rapidly decreases, dropping back to values near 0 Nm as the exhaust gases are expelled, marking the end of the cycle.

The graph in Figure 50 displays the inertia torque profile as a function of the crank angle over a 720° rotation.

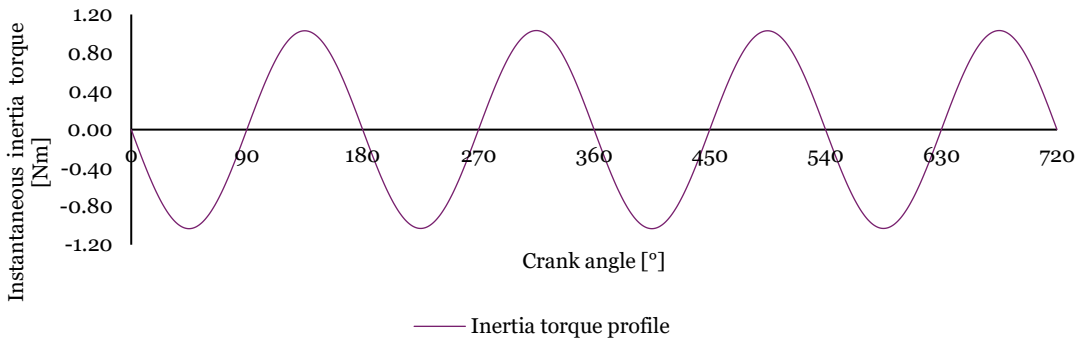

Figure 50 Inertia torque simulated for the Honda® GX 120 engine.

The sinusoidal nature of the curve presented in the graph in Figure 50 reflects the oscillatory motion of the engine's internal components. The torque oscillates between approximately ±1 Nm, the amplitude and frequency of these oscillations emphasize the alternating accelerations and decelerations of the piston and connecting rod within the engine.

In the graph from Figure 51, the blue line represents the resistive torque profile associated with the intake valve, while the red line shows the profile for the exhaust valve.

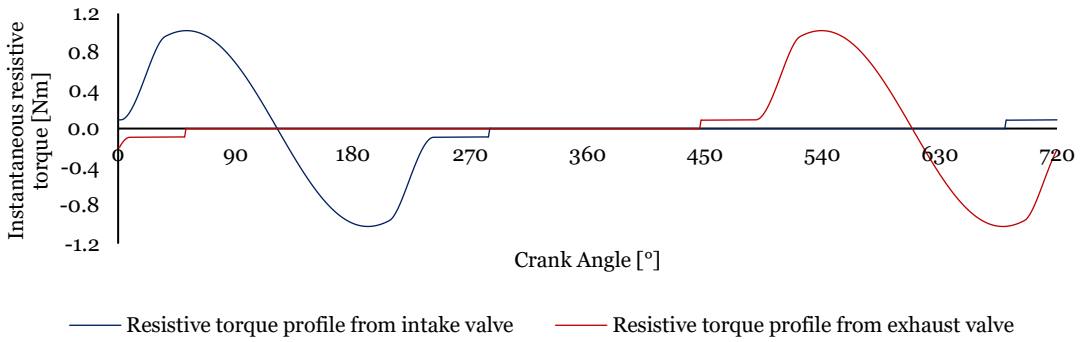

Figure 51 Instantaneous resistive torque profiles from the intake and exhaust valves simulated for the Honda® GX 120 engine.

The intake valve torque peaks at around 30° and dips near 180° as the crankshaft rotates, reflecting the phases of negative torque during spring compression and positive torque during spring release. Similarly, the exhaust valve's resistive torque fluctuates, peaking around 450° and dipping at approximately 630°. The torque variation follows the camshaft's rise and dwell phases acting on the spring, ranging within ±1 Nm.

The graph from Figure 52 shows the resistive torque profile generated by the splash lubrication system used by the Honda® GX 120 engine. Unlike the torque analysed above

from the valve system and the linear inertia of the system's internal components, the torque from the lubrication system always has a negative component that always opposes the engine's movement.

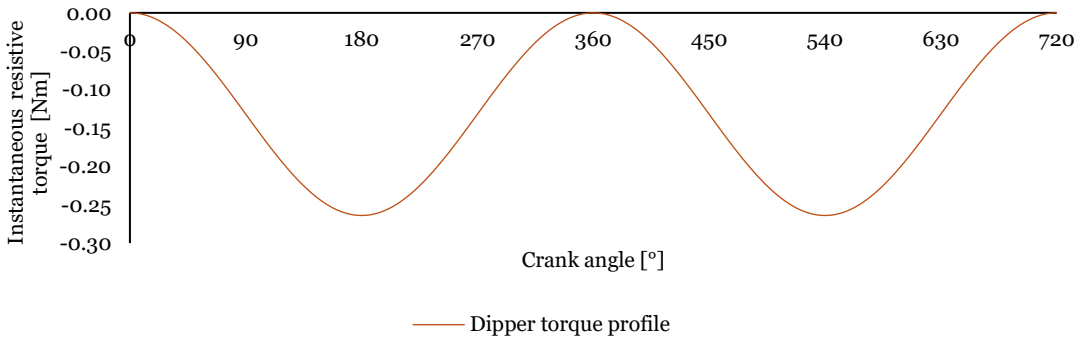

Figure 52 Simulated instantaneous resistive torque profile generated by the oil dipper in the Honda® GX 120 engine.

In Figure 52, the resistive torque generated by the dipper varies sinusoidally, with the torque reaching a peak negative value of approximately -0.28 Nm at around 180° and 540° when the dipper is fully submerged in the oil. The torque decreases to about 0 Nm near 0°, 360°, and 720° as the dipper moves out of the oil. This fluctuation in torque is consistent with the behaviour of the splash lubrication system, where the resistance is higher when the dipper encounters the most significant drag force from the oil.

Another type of torque that consistently represents a negative component is shown in Figure 53. This figure illustrates the instantaneous resistive torque profile resulting from friction within the engine, specifically focusing on the torque generated by the friction between the piston and cylinder walls and the friction in the crankshaft bearings.

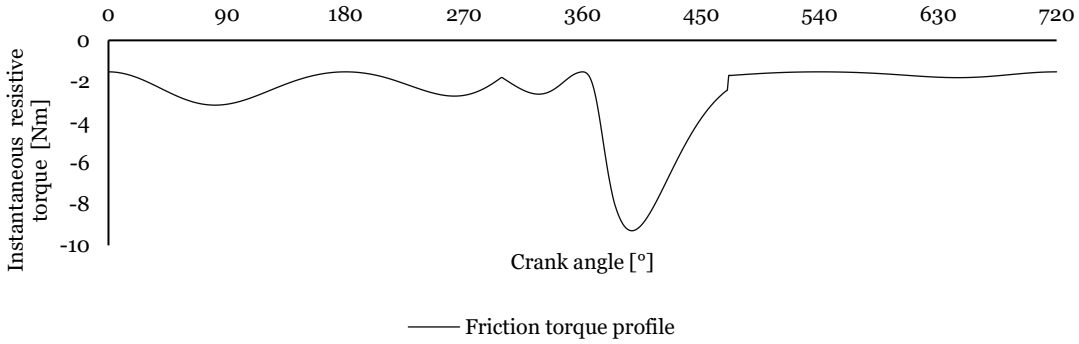

Figure 53 Instantaneous friction torque simulated for the Honda® GX 120 engine.

The graph in Figure 53 shows the fluctuating resistive torque caused by friction throughout the engine cycle, with values ranging from approximately -2 Nm at the beginning of the cycle to around -9 Nm after 360°. The resistive torque remains negative throughout, primarily due to friction between the piston and cylinder walls and forces acting on the crankshaft bearings. The profile reveals two distinct components: a constant friction component in the crankshaft bearings, maintaining a value around -0.2 Nm, and a varying component influenced by crank angle and crankshaft velocity. Peaks in the friction torque occur around 90° and 360°, according to points where forces on the piston are higher, leading to increased friction.

Figure 54 and Figure 55 show the results of the torque decomposition, and the total instantaneous torque simulated for the Honda® GX 120 engine.

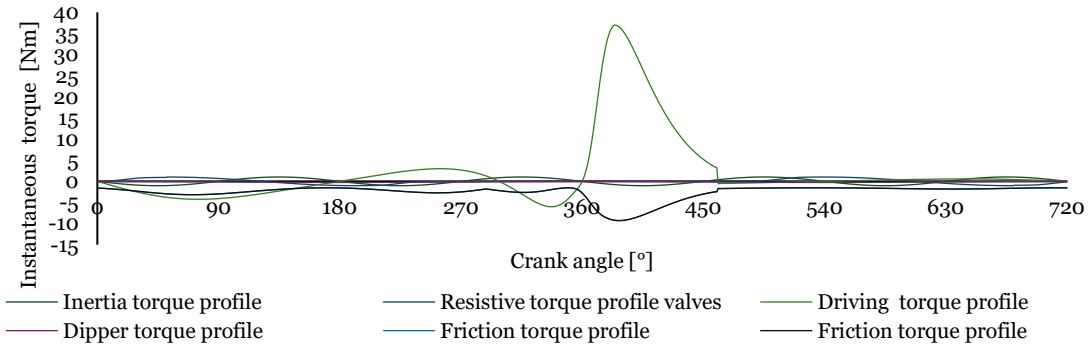

Figure 54 Simulated torque components for the Honda® GX 120 engine, including inertia torque, driving torque, resistive torque from valves, dipper torque, and friction torque, as a function of crank angle.

For instance, Figure 55 overlays all the components of the torque profile, including inertia torque, driving torque, resistive torque from the intake and exhaust valves, dipper torque, and friction torque. By comparing these components, we can observe that the driving torque, which reaches a peak of approximately 37 Nm around the 385° crank angle, is the dominant force. The inertia torque, depicted by a sinusoidal profile, fluctuates between approximately ±1 Nm, suggesting its influence throughout the entire engine cycle. However, it is significantly lower in magnitude than the driving torque and contributes relatively little to the overall torque profile.

The resistive torques from the intake and exhaust valves exhibit minor fluctuations, reaching maximum values of about ±1 Nm during peak activities. These profiles suggest how the resistive forces from the valve train introduce complexities into the overall torque profile, even though they remain relatively minor compared to the driving torque.

The dipper and friction torque, both consistently negative across the cycle, contribute to the resistive forces opposing the engine's motion. The dipper torque, varying sinusoidally, peaks at approximately -0.28 Nm, while the friction torque fluctuates between -0.2 Nm and -0.9 Nm, particularly around the 360° crank angle, during the power stroke. The friction torque is most significant during this phase, emphasizing its role in opposing engine movement, especially when the forces acting on the piston and cylinder walls are at their highest.

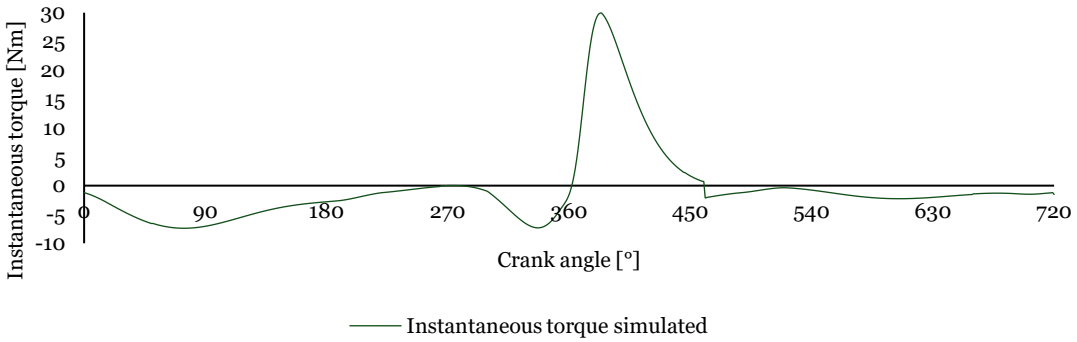

Figure 55 Overall instantaneous torque simulated for the Honda® GX 120 engine, combining all torque components.

Figure 55 presents the cumulative effect of all torque components, showing the overall instantaneous torque output of the Honda® GX 120 engine. The resultant profile follows the driving torque curve, with modulation introduced by resistive forces, inertia, and frictional effects. The peak torque reaches approximately 30 Nm around the 385° crank angle, coinciding with the combustion event and the expansion stroke. After the peak, the torque rapidly declines, influenced by the resistive torque and frictional forces during the exhaust stroke. The simulation illustrates that while the driving torque primarily contributes to the engine's output, resistive and inertia torques introduce fluctuations that significantly shape the torque profile, particularly during the intake and exhaust phases.

3.3.2. Velocity variation

The engine velocity variation is computed based on the engine torque, with the crankshaft speed fluctuating in response to the varying torque generated during different phases of the engine cycle. This velocity is calculated using the engine's inertia. Figure 56 illustrates the variation in angular velocity as a function of the crank angle, allowing to observe speed changes caused by the torque fluctuations analysed in the previous sections. These changes highlight the dynamic forces within the engine impact its

rotational speed stability, with deceleration and acceleration occurring due to the alternating torque contributions.

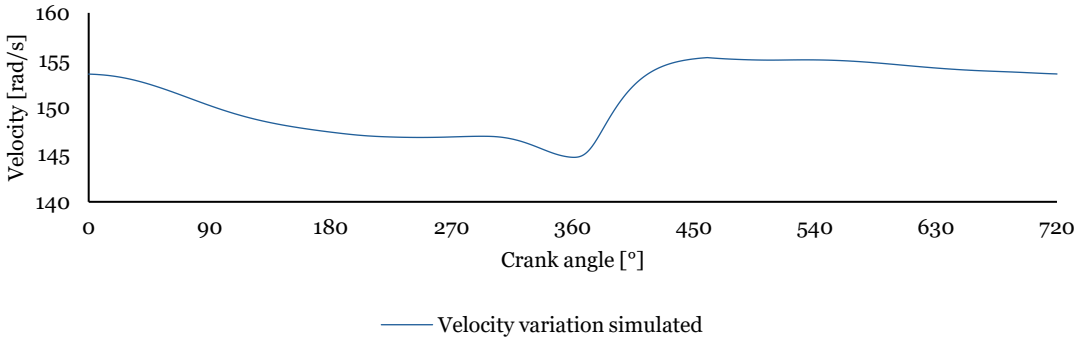

Figure 56 Simulated velocity variation for the Honda® GX 120 engine as a function of crank angle.

The graph in Figure 56 depicts the velocity variation over a complete engine cycle, influenced by the engine and flywheel's combined rotational inertia. The total inertia of the engine 14.74×10^{-3} kg m², comprises the engine's rotational inertia of 1.254×10^{-3} kg m² and the significantly larger inertia from the flywheel at 13.49×10^{-3} kg m².

As the graph shows, the velocity gradually decreases during the compression stroke, dropping to a minimum of around 145 rad/s just before the 360° mark, converging with the peak pressure and torque produced by the combustion process. At this point, the flywheel plays a crucial role in limiting the drop in velocity despite the large resistive forces and increasing torque demand. After combustion, a sharp increase in velocity is observed, reaching approximately 155 rad/s due to the rapid expansion of gases and the resulting power stroke. This increase highlights the engine's response to the significant driving torque generated by the combustion, which accelerates the crankshaft.

Based on the previously discussed velocity variations, Figure 57 compares how engine's velocity fluctuates when different percentages reduce the flywheel's inertia. The graph illustrates four scenarios where the flywheel inertia is decreased by 20%, 40%, 60%, and 80%, respectively, demonstrating the significant impact of flywheel inertia on engine speed stability.

As the flywheel inertia decreases, the velocity variations become more pronounced, with the engine speed experiencing more significant dips, particularly during the compression stroke. For instance, a 60% reduction in flywheel inertia, promotes a velocity decrease to around 120 rad/s, compared to approximately 145 rad/s with only a 20% reduction. This shows that the flywheel's role in moderating fluctuations is diminished as its inertia

decreases, leading to more rapid deceleration during high torque demand periods and less damping of these variations.

The graph highlights that lower flywheel inertia promotes greater instability in the engine's rotational speed, which could negatively affect engine performance and smoothness. This insight reinforces the flywheel's importance in maintaining speed stability and suggests that any reductions in flywheel inertia must be carefully considered to balance performance, efficiency, and stability.

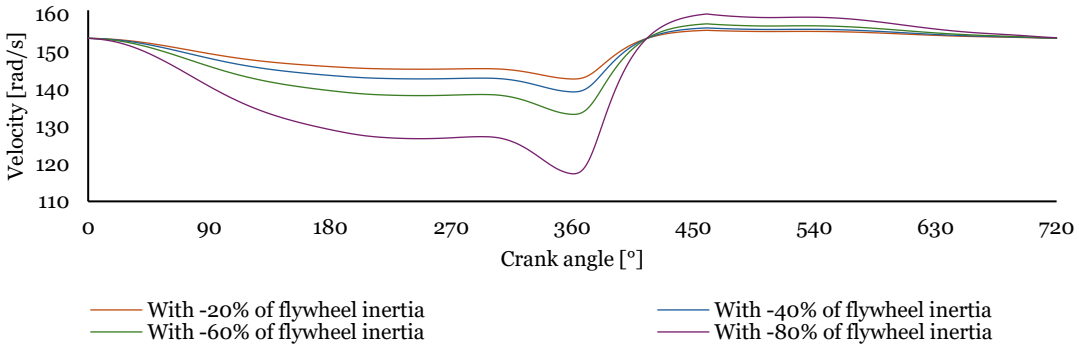

Figure 57 Simulated velocity variation for the Honda® GX 120 engine with different reductions in flywheel inertia, illustrating the impact of inertia on engine angular velocity.

As the flywheel inertia decreases, the velocity variations become more pronounced, with the engine speed experiencing more significant dips, particularly during the compression stroke. For instance, a 60% reduction in flywheel inertia lead to a velocity drops to around 120 rad/s, compared to approximately 145 rad/s with only a 20% reduction. This shows that the flywheel's role in moderating fluctuations is diminished as its inertia decreases, leading to more rapid deceleration during high torque demand periods and less damping of these variations.

The analysis continues with Figure 58, which compares the velocity variation with and without the flywheel.

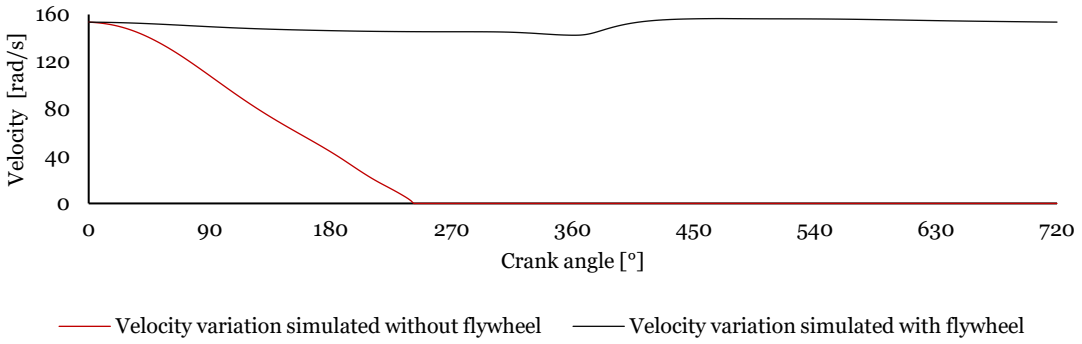

Figure 58 Velocity variation comparison between simulated engine operation with and without the flywheel.

This graph illustrates the flywheel's essential role in maintaining speed stability throughout the engine cycle and highlights how the absence of the flywheel significantly affects the engine's ability to sustain rotational motion, particularly during critical phases such as compression and expansion.

Without the flywheel (represented by the red line), the engine's velocity declines sharply during the intake and compression strokes, dropping almost linearly after the crankshaft rotates past 90°. This prompt deceleration persists through the compression phase, with the engine's speed eventually reaching 0 rad/s just before the 180° mark. This abrupt halt means that the engine cannot continue its motion beyond this point without additional external energy or stored inertia to overcome the resistive forces. In actual operating conditions, such a scenario would lead to engine stalling, as the momentum from earlier strokes is insufficient to push the piston through the cycle.

In contrast, the graph's black line, representing the flywheel simulation, shows how the flywheel stabilizes performance. The velocity decreases gradually during the intake and compression strokes, remaining within a stable range of 145 to 155 rad/s throughout the cycle. The flywheel's stored inertia compensates for the torque deficits during compression, preventing the engine from stalling and enabling smoother transitions between strokes. As the engine nears the compression peak, the flywheel ensures that velocity stays well above zero, showcasing its critical role in mitigating the sharp deceleration seen in the no-flywheel scenario.

3.4. Experimental validation

3.4.1. Experimental setup

Two types of sensors were employed in the experimental procedure: a variable reluctance sensor (VR) and a Light Dependent Resistor (LDR) sensor. The LDR sensor was selected

for its higher precision and shorter switching time. In contrast, the VR sensor was chosen due to its widespread use in internal combustion engines, commonly applied for position and speed measurement. The VR sensor is extensively used for position and speed control in internal combustion engines, whereas the LDR sensor, offering greater precision, is typically utilized in industrial environments.

The velocity was calculated based on the time interval between two teeth of the trigger wheel, measuring the time between the points at which the voltage read by the oscilloscope crossed the X-axis, both in the descending and ascending directions, to minimize potential errors. The toothed wheel generates a sinusoidal wave due to the variation in the magnetic field induced by the VR sensor, allowing accurate determination of the voltage crossing points. The same procedure was applied to the LDR sensor, with the difference that, in this case, the signal variation was caused by the teeth of the wheel blocking the light to the sensor as they passed [37].

The experimental process involved using a Keysight® EDUX1052A oscilloscope, which has the main characteristics detailed in Table 4. This oscilloscope was used to acquire and analyse the sensor signals during the experiments. Figure 59 shows the image of the Keysight® EDUX1052A oscilloscope used in the setup.

Table 4 Keysight® EDUX1052A main characteristics table.

Characteristic	Description
Model	Keysight® EDUX1052A
Channels	2 Analog Channels
Sampling Rate	1 GSa/s maximum
Memory Depth	1 Mpts (per channel)
Vertical Resolution	8 bits
Vertical Sensitivity	1 mV/div to 5 V/div
Time Base Range	5 ns/div to 50 s/div
Connectivity	USB 2.0, LAN interface

Figure 59 Oscilloscope Keysight® EDUX1052A.

The process began with adjusting the variable reluctance sensor and a trigger wheel with 36 teeth. It was determined that the tests would be conducted with a time window of 20 ms per division on the X-axis and a voltage amplitude of 2 V per division. The data were stored with 10 000 points, even though the oscilloscope could store up to 50 000 points. After some trials, it was concluded that increasing the number of points did not provide significant improvements in resolution or signal quality and only served to prolong the acquisition process unnecessarily.

To validate the acquisition system, a reading mechanism driven by an electric motor was created, as illustrated in Figure 60. Once this setup was established, tests were conducted using both sensors, and the results were validated by averaging the readings from 10 tests. The tests conducted with the electric motor revealed comparable results between the LDR and VR sensors.

Subsequently, a new series of tests were carried out using the internal combustion engine. The analysis of these results indicated that both sensors provided valid readings. However, the variable reluctance sensor exhibited better results, likely due to the greater susceptibility of the LDR sensor to the laboratory conditions or vibrations generated by the internal combustion engine.

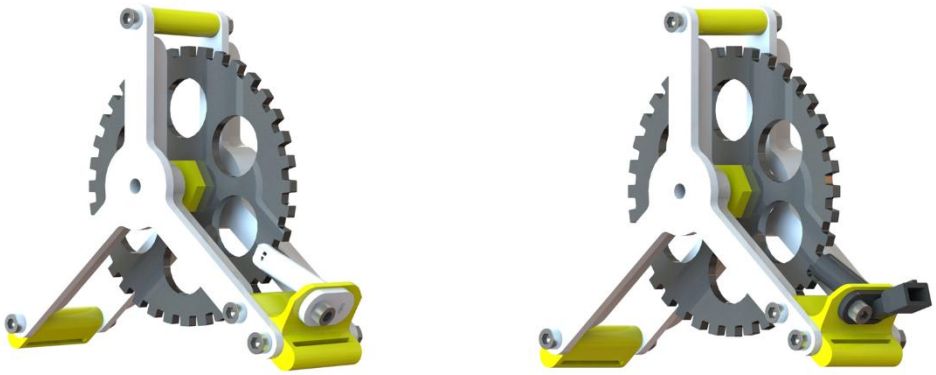

Figure 60 Reading mechanism driven by an electric motor used to validate the acquisition system, with the LDR sensor on the left and the VR sensor on the right.

Figure 61 and Figure 64 show the voltage signals recorded by the LDR and VR sensors, respectively, during the motor's rotational motion. These signals reflect each sensor's response to the periodic voltage variations induced by the rotation of the toothed wheel.

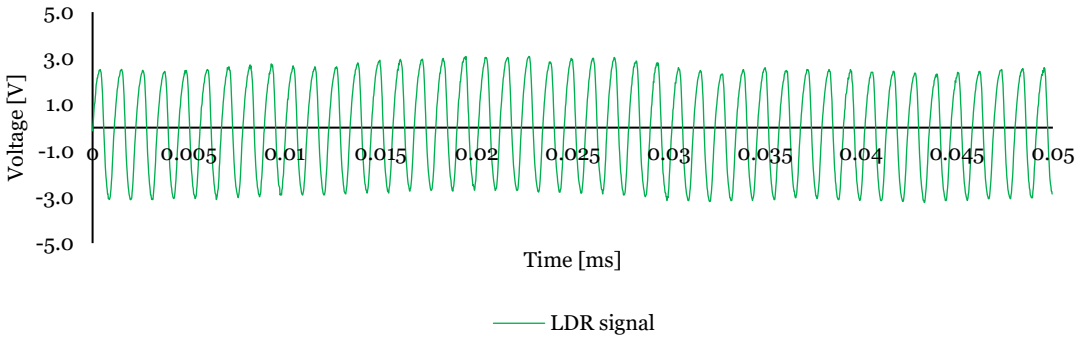

Figure 61 Voltage signal recorded by the LDR sensor during the rotational motion of the motor.

Figure 61 shows the voltage signal recorded by the LDR sensor throughout 0.05 ms. The voltage oscillates between approximately -3.0 V and +3.0 V, with a regular pattern of peaks and troughs, indicating the response of the sensor as the trigger wheel's teeth alternately block and unblock the light path. This sinusoidal-like pattern represents the periodic nature of the LDR sensor's detection as it responds to the changing presence of light due to the rotation of the toothed wheel.

Figure 62 illustrates the velocity variation profiles obtained from 10 tests conducted with the LDR sensor. Each test was performed under identical conditions, allowing for a direct comparison of the sensor's readings across multiple cycles.

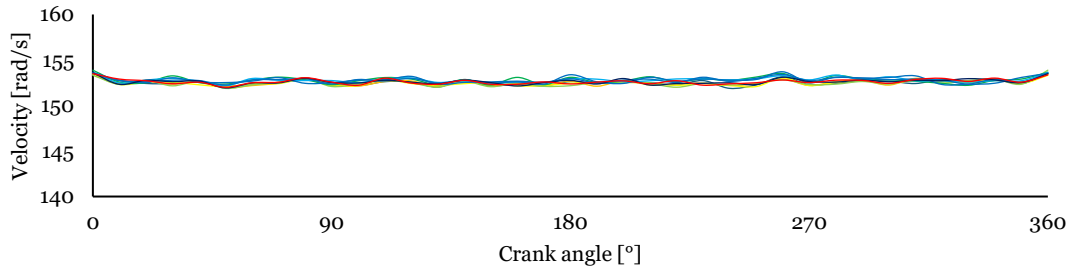

Figure 62 Velocity variation profiles across 10 tests conducted with the LDR sensor.

The graph in Figure 62 displays the velocity variation profiles across ten tests, with each test showing similar patterns of fluctuations. A key observation is that the irregularities in the velocity profile occur at consistent crank angles, with the magnitude of these fluctuations remaining nearly identical across all tests. This consistency suggests that repeatable, systematic factors, such as minor imperfections in the sensor setup or mechanical irregularities in the toothed wheel, caused the irregularities.

Figure 63 shows the comparison between the average velocity profile obtained from the 10 LDR sensor tests and the reference velocity.

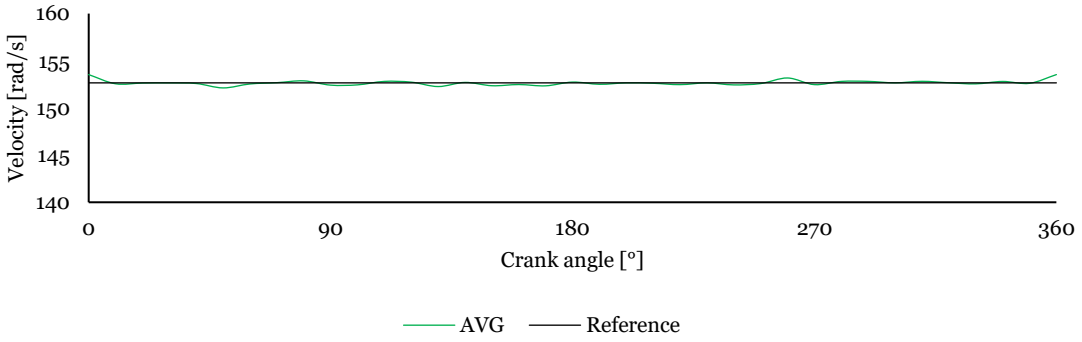

Figure 63 Comparison between the average from 10 tests conducted with the LDR sensor (green) and the reference constant speed (black).

Similarly to Figure 61, Figure 64 presents the voltage signal captured by the VR sensor during the motor's rotational motion, illustrating how the sensor responds to changes in the magnetic field induced by the movement of the toothed wheel. Slight variations in amplitude were observed due to imperfections in the wheel geometry, magnetic artefacts, or surface finish, but the signal remained stable and periodic.

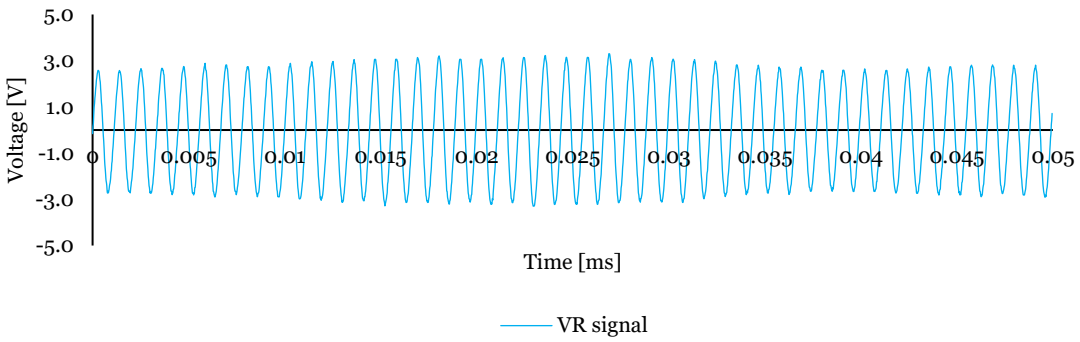

Figure 64 Voltage signal recorded by the VR sensor during the rotational motion of the motor.

Figure 64 presents the voltage signal obtained from the VR sensor during the same period. Like the LDR sensor, the VR sensor generates a sinusoidal voltage signal, oscillating between approximately -3.0 V and +3.0 V. The VR sensor's signal results from changes in the magnetic field caused by the movement of the toothed wheel. One crucial observation is the slight variation in the amplitude of the signal, which is influenced by the process of magnetization and demagnetization of the sensor. This variation is likely caused by minor irregularities in the geometry of the trigger wheel's teeth or imperfections in its surface, leading to fluctuations in the magnetic flux as the wheel rotates. These irregularities affect the consistency of the magnetic field strength and, consequently, the amplitude of the output signal, but not the periodicity of the signal.

The analysis for Figure 65 and Figure 66 follows a similar structure as the evaluation for Figure 62 and Figure 63, with a focus on the performance of the VR sensor in capturing velocity variations across 10 tests. Figure 65 displays the velocity variation profiles obtained from the VR sensor during the 10 tests. As with the LDR sensor, consistent fluctuations can be observed across all tests. However, in this case, although the VR sensor shows slightly more pronounced variations around the 0° and 360° crank angles, it still delivers more reliable results overall. This improved performance is likely due to the VR sensor’s greater robustness to magnetic field changes, making it less sensitive to noise, minor mechanical imperfections, and environmental effects that could otherwise distort the signal.

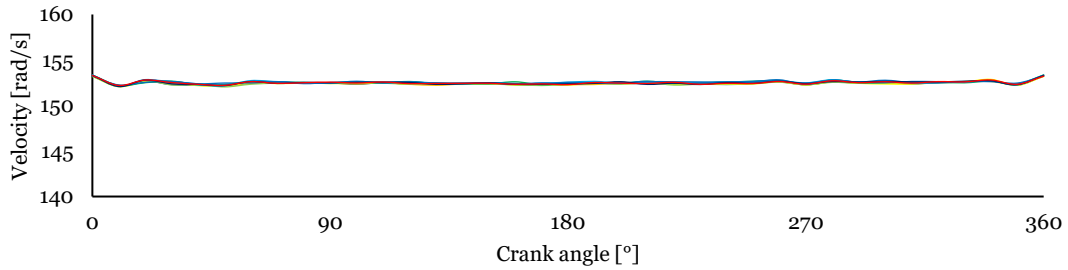

Figure 65 Velocity variation profiles across 10 tests conducted with the VR sensor.

Figure 66 presents the average velocity variation from the 10 VR sensor tests and the reference velocity. The velocity remains relatively stable with only minor deviations.

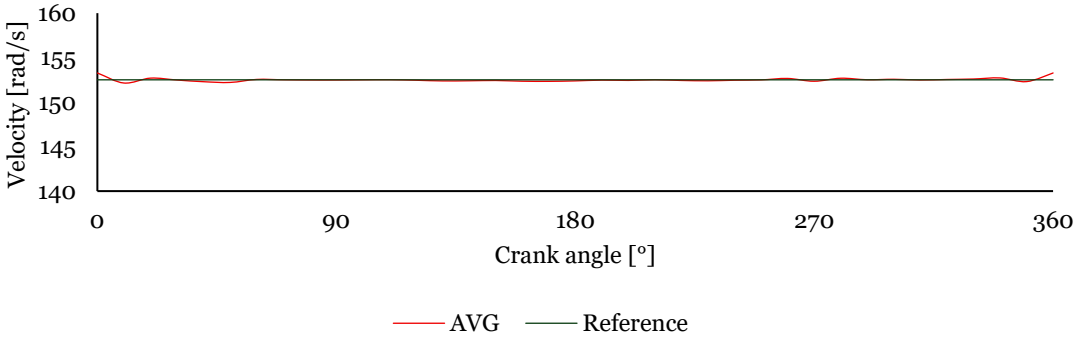

Figure 66 Comparison between the average from 10 tests conducted with the VR sensor (red) and the reference constant speed (black).

Figure 67 provides a direct comparison between the average velocity profiles obtained from the 10 tests using the VR sensor (red) and the LDR sensor (green), plotted against the reference constant speed (black) corresponding to the disc driven by the electric motor. The close alignment of both sensor signals with the reference confirms the effectiveness of the measurement setup. Quantitatively, the VR sensor exhibited a standard deviation of 0.22 rad/s and an amplitude of 1.13 rad/s, while the LDR sensor showed slightly higher values, with a standard deviation of 0.28 rad/s and an amplitude of 1.41 rad/s. These analytical results reinforce the graphical interpretation, demonstrating that both sensors offer consistent and repeatable measurements, with the VR sensor displaying marginally lower dispersion and oscillation amplitude.

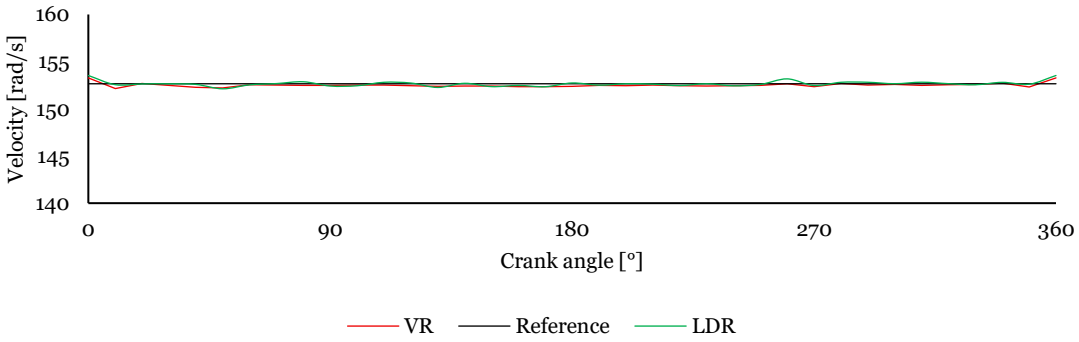

Figure 67 Comparison between the average values from 10 tests conducted using the VR sensor (red) and the LDR sensor (green), against the reference constant speed (black).

Figure 68 shows the mount designed to position the LDR and VR sensor accurately for data acquisition in the Honda® GX 120 engine. This mount ensures the sensor is fixed during testing, allowing consistent signal readings as the engine operates. The design accommodates the sensor and the toothed wheel, ensuring the sensor is aligned correctly for optimal performance.

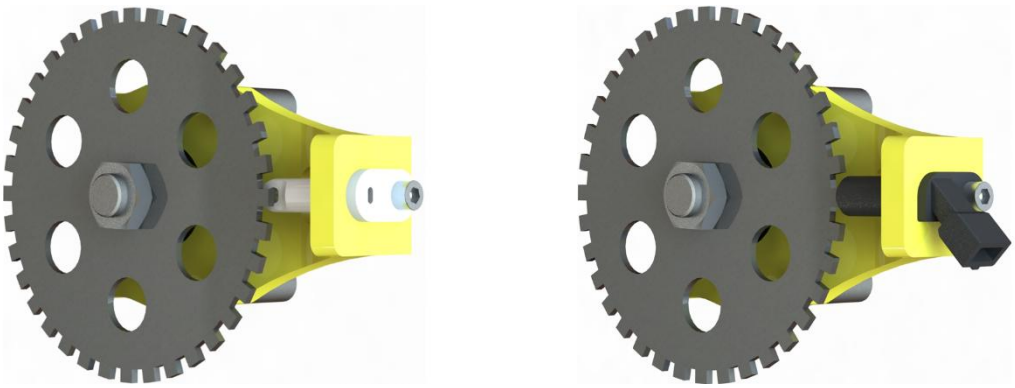

Figure 68 Mount created to position the sensor for data acquisition in the Honda® GX 120 engine, with the LDR sensor on the left and the VR sensor on the right.

The results in Figure 69 and Figure 70 provide the data obtained using the LDR sensor during the engine tests. Figure 69 presents the velocity variation profiles from 10 tests conducted under the same engine conditions, showing consistent behaviour across the tests. Figure 70 displays the average velocity variation, consolidating the data from all tests to give a more precise overview of the overall trend.

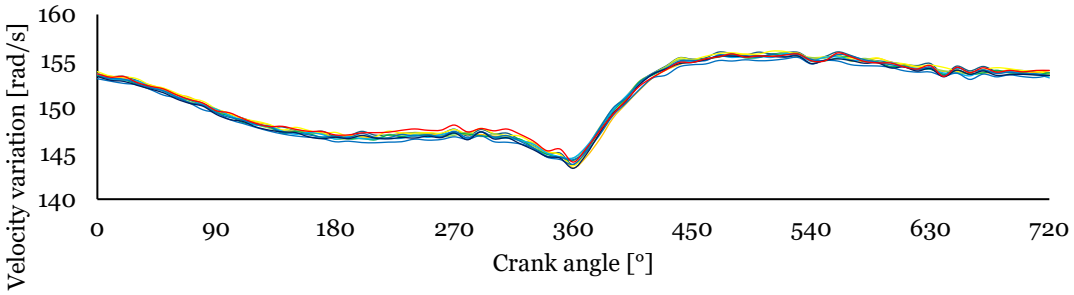

Figure 69 Velocity variation profiles across 10 tests conducted with the LDR sensor conducted in the Honda® GX 120 engine.

The velocity variation profiles in Figure 69 observe a consistent behaviour across the ten tests, with minimal deviations between them. However, it is noticeable that test represented in red displays a slight displacement from the other profiles, especially around the 360° mark, where the most significant variations occur. Despite this, the alignment of the majority of the profiles indicates that the LDR sensor provided reliable and repeatable measurements even in the more demanding environment of the internal combustion engine. The slight deviations in this test could result to specific external factors during that trial. Nevertheless, the curves remain relatively soft overall, with no significant erratic behaviour, suggesting that the sensor-maintained stability and accuracy during the tests. The presence of minimal noise in the signal further highlights the sensor's robustness in capturing variations of velocity under these conditions.

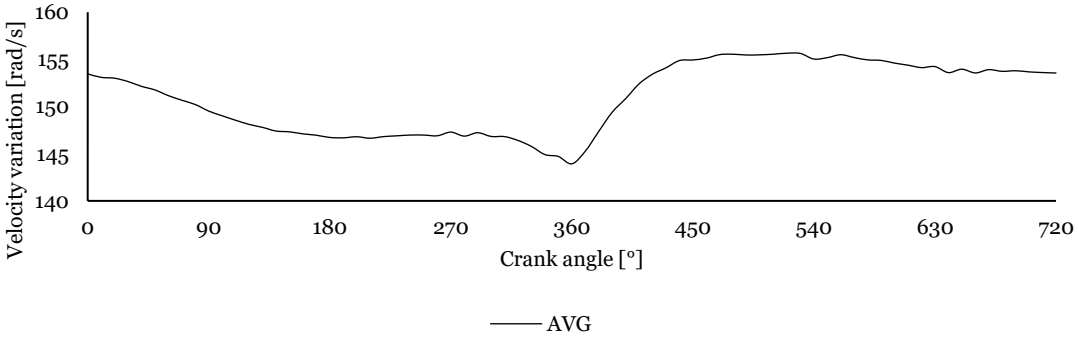

Figure 70 Average velocity variation profile variation profiles across 10 tests conducted with the LDR sensor conducted in the Honda® GX 120 engine.

Figure 70 presents the average velocity variation profile, observing the quality of the signal captured by the LDR sensor. The averaging process softens the minor deviations observed in the individual tests, providing a clear and stable trend. The overall shape of

the curve remains smooth, with no sharp spikes or irregularities, indicating that the sensor consistently captured the velocity variation throughout the engine cycle.

The results in Figure 71 and Figure 72 illustrate the velocity variation data obtained using the VR sensor during engine testing. These figures provide a comprehensive look into how the VR sensor captured the engine's dynamic behaviour throughout the operating cycle. Figure 71 presents the velocity variation profiles from 10 tests, each conducted under the same engine conditions, allowing for an evaluation of the consistency and accuracy of the VR sensor measurements. Figure 72 shows the average velocity variation across these tests, providing an aggregated view highlighting the overall trend without the noise in individual test runs.

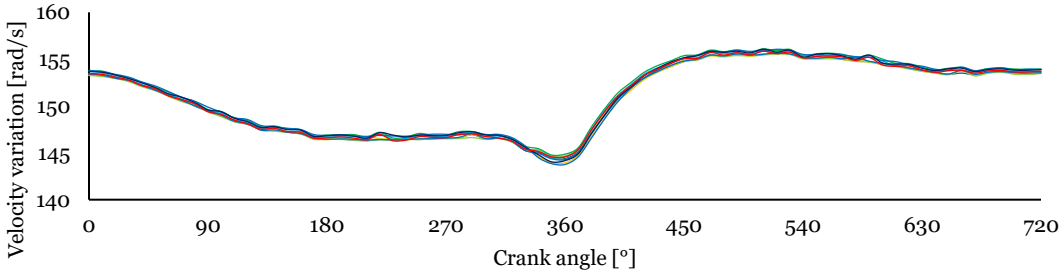

Figure 71 Velocity variation profiles across 10 tests conducted with the VR sensor conducted in the Honda® GX 120 engine.

Upon analysing the data observation in Figure 71 show that the velocity variation profiles exhibit a similar pattern across the tests. The consistency between the tests suggests that the VR sensor can provide repeatable measurements despite the engine's operating conditions. The profiles display smooth variations, with a significant dip in velocity around the 360° mark, corresponding to the engine's compression and combustion strokes, followed by a recovery during the power stroke. While general behaviour remains consistent, there are minor deviations in the individual tests, particularly around the 360° and 450° marks, where the engine experiences rapid changes in velocity.

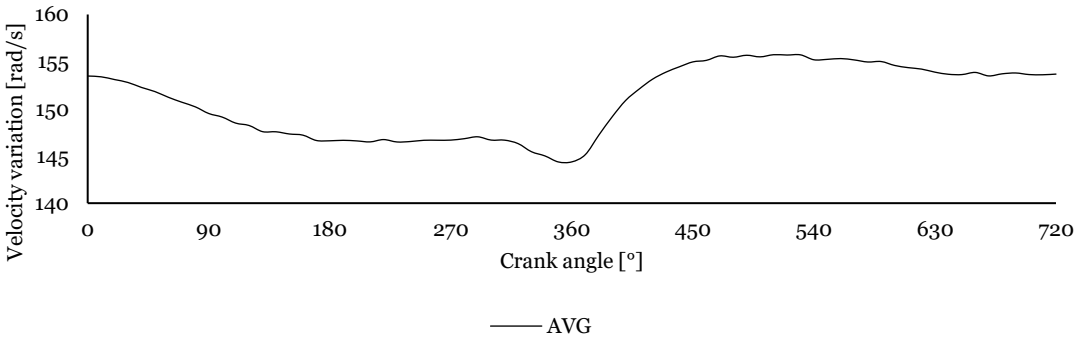

Figure 72 Average velocity variation profile variation profiles across 10 tests conducted with the VR sensor conducted in the Honda® GX 120 engine.

Figure 72 presents the average velocity variation measured using the VR sensor. The consistent pattern observed confirms the VR sensor's ability to capture the engine's rotational dynamics reliably.

Like the LDR sensor, the VR sensor demonstrated stable and repeatable behaviour across multiple tests. However, while the LDR sensor is more sensitive, this increased sensitivity makes it more susceptible to external influences, such as mechanical vibrations and variations in operating conditions. As a result, the LDR data tends to exhibit higher measurement noise, which can obscure subtle variations in the engine's motion.

Figure 73 compares the average velocity profiles obtained from both sensors. The results highlight that, although both provide reliable data, the VR sensor offers a cleaner signal with less noise, allowing for better identification of finer details in the engine's behaviour. In contrast, the LDR sensor's greater sensitivity introduces more variability, which may mask minor but relevant dynamic changes.

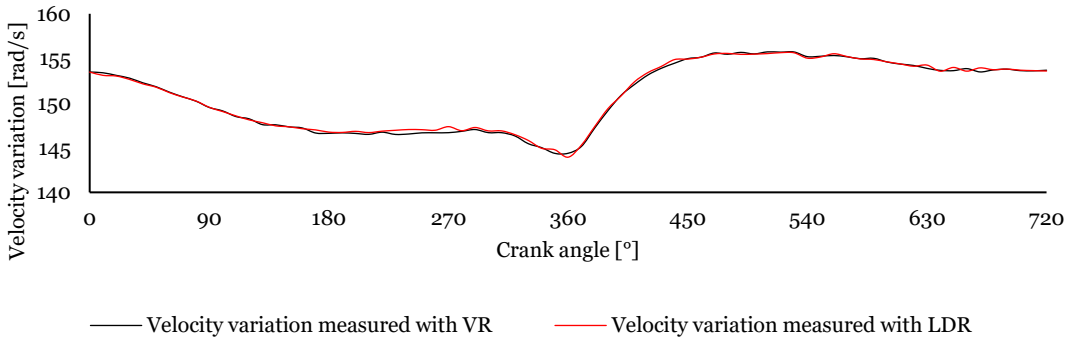

Figure 73 Comparison of velocity variation measurements obtained using a VR sensor and an LDR sensor.

Ultimately, the results obtained from both sensors are consistent and support one another. The standard deviation of the LDR signal was 3.67 rad/s, while that of the VR sensor was 3.75 rad/s, indicating that both sensors provide similar levels of signal stability. Although the LDR sensor exhibits slightly lower variation, the VR shows more repeatability in the test. The sensor's ability to function reliably in harsher operating conditions makes it a practical choice for ongoing engine tests.

3.4.2. Experimentally obtained results

This section presents the experimental results obtained from the Honda® GX 120 engine operating at 1500 RPM, including both the velocity variation and the instantaneous torque profiles, offering a detailed understanding of the engine's dynamic behaviour. Figure 74 displays the average velocity variation profile, illustrating how the engine's rotational speed changes across different crank angles. Figure 75 shows the instantaneous torque values measured throughout the engine cycle, comparing the raw experimental data with a soften version using a moving average to highlight the underlying trends. Figure 76 integrates the velocity variation with the moving average torque, providing a comprehensive view of the engine's dynamic response correlating torque changes with rotational speed fluctuations.

The torque was determined using the velocity variation data, applying the angular acceleration and inertia principle. By selecting the angular acceleration from the changes in velocity over time and multiplying it by the known rotational inertia of the engine and flywheel, the instantaneous torque values were derived, allowing for an analysis of the forces acting on the crankshaft during the engine cycle.

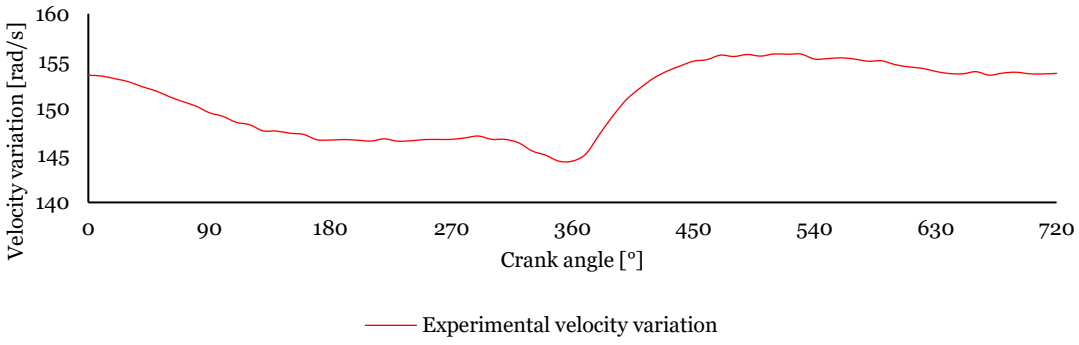

Figure 74 Average velocity variation profile measured in the Honda® GX 120 engine at 1500 RPM.

Figure 74 illustrates the average velocity measured during the engine's operation. The curve remains relatively stable throughout the cycle, with a minor dip occurring just

before the 360° mark, corresponding to the compression stroke, and a significant increase in velocity during the power stroke. The velocity peaks at around 157 rad/s after 360° before gradually returning to a lower value as the cycle progresses.

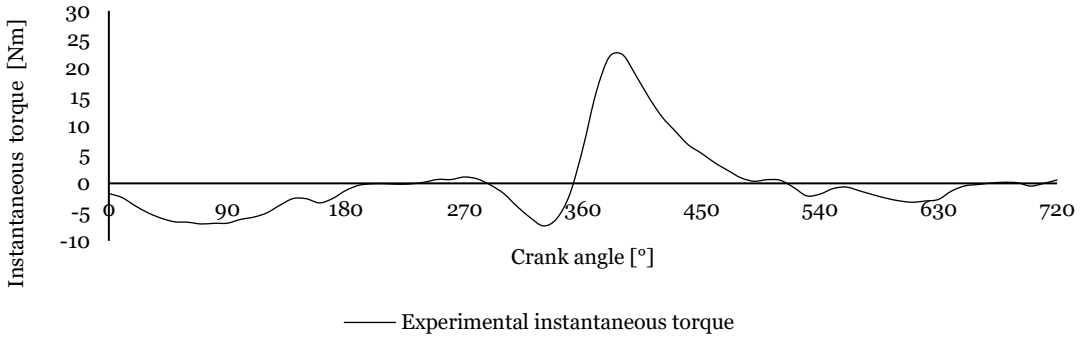

Figure 75 Experimental instantaneous torque measured at 1500 RPM in the Honda® GX 120 engine.

Figure 75 displays the torque profile that shows a sharp peak reaching approximately 25 Nm around the 360° crank angle, which coincides with the ignition and power stroke of the engine. Before this, the torque fluctuates slightly around zero during the intake and compression strokes. After the power stroke, the torque decreases rapidly and exhibits minor variations during the exhaust stroke.

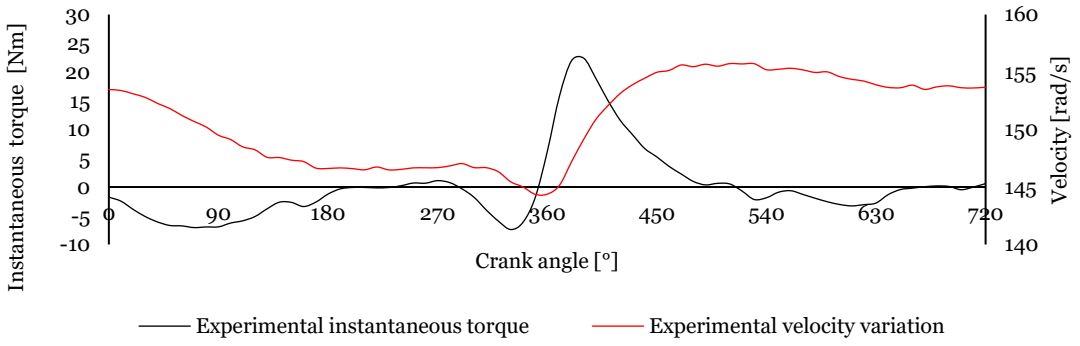

Figure 76 Comparison of experimental instantaneous torque and velocity variation measured in the Honda® GX 120 engine at 1500 RPM. The black line shows torque, and the red line shows the velocity variation.

Figure 76 compares the instantaneous torque with the measured velocity variation. As expected, the velocity variation follows a similar pattern to the torque profile, peaking during the power stroke when the torque is at its maximum and reducing during the compression and exhaust phases. The relationship between the torque and velocity variations is evident, as the increase in torque during the power stroke directly drives the increase. Conversely, the reduction in torque after the power stroke corresponds to a decrease in velocity.

These figures demonstrate the engine's characteristic behaviour during a complete cycle. The velocity and torque profiles follow expected trends, with torque peaking during the power stroke and velocity variations reflecting the changes in torque output. The moving average applied to the torque profile helps to clarify the overall trend while reducing noise from the raw data, making the results easier to interpret. This analysis provides valuable insight into the engine's operational efficiency and dynamic response under a constant load at 1500 RPM.

3.5. Comparative analysis

This section compares the simulated and experimentally measured velocity variations of the Honda® GX 120 engine at 1500 RPM. The comparison aims to validate the accuracy of the simulation model by evaluating its ability to replicate the engine's real dynamic behaviour. By analysing the velocity variations throughout the engine cycle, we can assess how well the simulated results align with the experimental data, providing insights into the simulation's fidelity and the influence of physical factors such as friction and mechanical losses in the actual engine operation.

The graph in Figure 77 compares the simulated and experimentally measured velocity variations over a complete engine cycle, providing a clear picture of the engine's dynamic performance. Both curves follow a similar trend, indicating that the simulation closely matches the real-world measurements, albeit with minor discrepancies in specific regions.

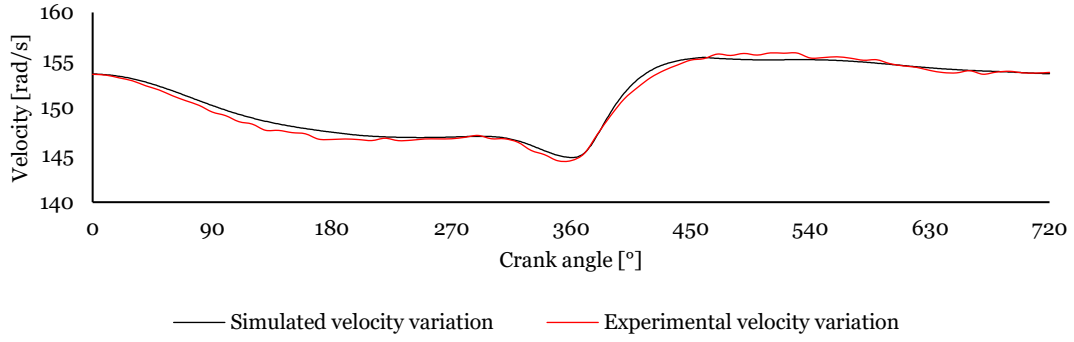

Figure 77 Comparison between simulated and measured velocity variation in the Honda® GX 120 engine at 1500 RPM. The green line represents the simulated velocity variation, while the black line shows the experimentally measured velocity variation.

At the beginning of the cycle, from 0° to around 270°, both the simulated and measured curves show a steady decline in velocity, starting at approximately 155 rad/s and gradually decreasing to around 145 rad/s by the time the crank angle reaches 270°.

The most significant divergence between the simulated and measured values occurs between 270° and 360°. In this region, the measured velocity dips to a minimum of about 142 rad/s just before 360°, whereas the simulated velocity only drops to approximately 145 rad/s. This discrepancy could be the result of factors such as frictional losses or slight mechanical irregularities in the engine, which are more difficult to model and simulate accurately.

Following this point, both curves display a sharp increase in velocity between 360° and 450°, converging with the power stroke, where the expanding gases accelerate the piston. The measured velocity peaks at around 157 rad/s just after 360°, while the simulated curve reaches a slightly lower peak at approximately 155 rad/s. Despite this slight difference, the general shape of the curves is nearly identical, indicating that the simulation effectively captures the essential dynamics of the power stroke.

From 450° to 720°, both curves gradually return to a more stable velocity, fluctuating between 150 and 155 rad/s as the engine completes the exhaust and intake strokes. The close alignment of the curves in this region suggests that the simulation accurately models the less dynamic portions of the engine cycle, where the torque variations are minor and more consistent.

Overall, the comparison reveals that the simulation provides a reliable representation of the engine's velocity variation, with minor deviations likely caused by real-world factors not fully accounted for in the model. The agreement between the measured and simulated curves validates the simulation approach, making it helpful in analysing the engine's behaviour under various operating conditions.

Figure 78 compares the simulated and experimentally measured instantaneous torque profiles for the Honda® GX 120 engine at 1500 RPM, allowing an assessment of the model’s ability to replicate real engine torque behaviour. The experimental torque profile was derived from the measured angular velocity variation and the known rotational inertia of the engine system. It represents the torque required to maintain engine operation under idle conditions, where the engine produces just enough torque to overcome internal losses and sustain rotation.

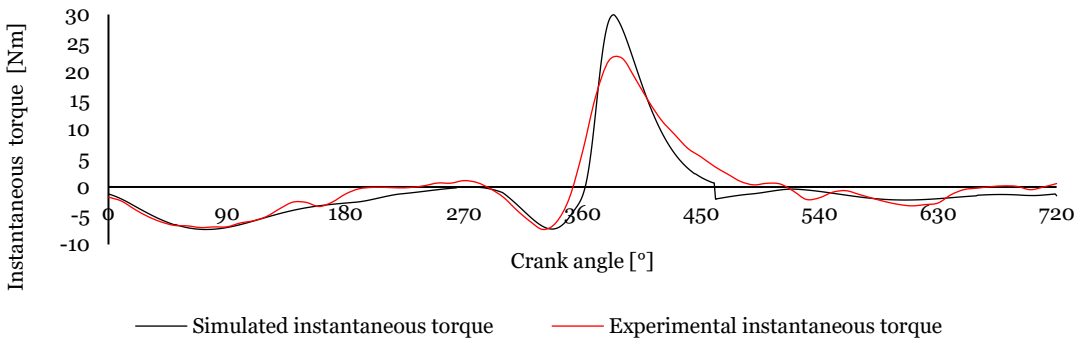

Figure 78 Comparison between the simulated and experimental instantaneous torque profiles for the Honda® GX 120 engine at 1500 RPM. The black line represents the simulated torque, while the red line shows the experimentally measured torque.

The graph in Figure 78 compares the instantaneous torque obtained from the simulation with the experimentally measured torque during the engine cycle. Both curves demonstrate a clear correlation in the overall torque trend but exhibit differences in magnitude, particularly around the peak torque values.

In the experimental torque curve, the red line shows a more gradual rise in torque leading up to the 360° mark, corresponding to the engine's power stroke. The peak torque experimentally measured reaches around 25 Nm, whereas the simulated torque (black line) reaches significantly higher at approximately 30 Nm during the same crank angle. This discrepancy suggests that the simulation overestimates the combustion forces acting on the piston, possibly due to assumptions in the model regarding combustion efficiency or mechanical losses.

After the ignition, the experimental and simulated curves decrease, with the torque gradually dropping as the expansion stroke concludes. The experimental curve softens out more gradually, showing more dampened fluctuations, whereas the simulated curve exhibits sharper declines and variations between 360° and 450°. These fluctuations could be attributed to the idealized conditions assumed in the simulation, which may not account for real-world factors such as frictional losses or engine vibrations that dampen these fluctuations in practice. Despite the magnitude differences, the phase alignment between the simulated and experimental torque profiles is quite close. Both show a dip in torque before the power stroke and similar behaviour through the compression and intake strokes, suggesting that while the magnitude discrepancies are notable, the overall shape and timing of the torque generation align well between the two data sets, suggesting that the simulation captures the general engine dynamics.

4. Mechanical actuator - Balancing cam mechanism

4.1. Design concept

Following the analysis of the internal combustion engine's instantaneous torque, velocity variation and a deeper understanding of the effects caused by interrupted and irregular torque, a balancing cam mechanism is proposed to generate a counteracting torque aimed at minimizing fluctuations in the engine's torque output. The components of this system include a spring for energy storage and a cam specifically designed to align with the engine's torque profile. A CAD model representing this mechanism implemented as an example in an engine is shown in Figure 79. The mechanism is structured to produce a counteracting torque at each rotation angle of the crankshaft, matching the output torque in magnitude but in the opposite direction.

Figure 79 CAD model of the proposed balancing cam mechanism, designed to produce a counteracting torque at various crankshaft angles, with direct implementation in the camshaft.

The designed cam must replicate the engine's opposing torque to achieve the desired mechanism response. It can be installed on the camshaft or with a 2:1 transmission ratio relative to the crankshaft, like the engine's distribution system. It may increase friction and resistive torque, leading to a more complex system. This is due to the torque-contributing events dispersed over the 720º crankshaft rotation in a 4-stroke cycle. The direct integration of this mechanism into the crankshaft would simplify implementation but is impractical for addressing resistive and driving torque irregularities. However, it would be adequate for inertia torque, as shown in Figure 50 with its 360º periodicity. Figure 79 illustrates a potential implementation in a single-cylinder engine using the existing distribution system and camshaft to simplify the system and minimize friction. This implementation assumes available space on the camshaft for the cam and that the

camshaft and transmission ratio can support the counteracting torque. These premises are valid for a demonstrative implementation in this specific engine construction.

4.2. Determination of the balancing cam profile

The cam's profile used for controlling the actuator in response to the engine's needs, was developed by considering the torque acting upon it, which is then transformed and stored in the spring. To design the cam profile, the cam radius must be determined as a function of the crankshaft rotation angle for a previously defined torque profile. Figure 80 is a diagram of the forces acting on the cam [30], [96], [97].

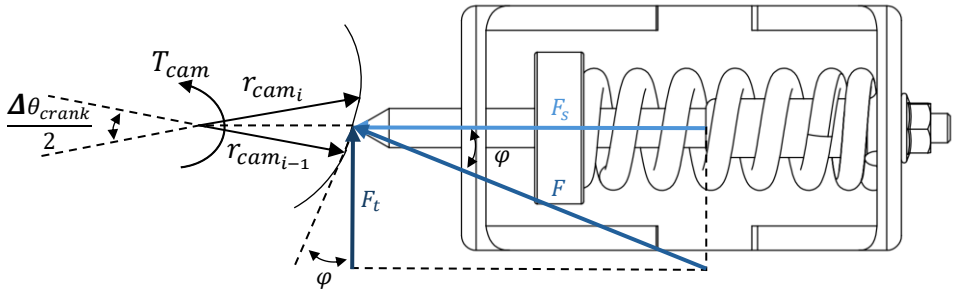

Figure 80 Diagram of the mechanism used to derive the equations necessary to design the balancing cam that mimics the desired torque profile.

The torque on mechanism camshaft T_{cam} is the product of the tangential force F_t by cam radius:

$$T_{cam} = \mathrm{F_t} r_{cam} \tag{102}$$

$T_{cam} - torque\ on\ mechanism\ camshaft\ [Nm]$

$F_t - \ tangential\ force\ [N]$

$r_{cam} - cam\ radius\ [m]$

From Figure 80, F_t is the product from the F_s by the $tan\,\varphi$ as presented in Equation 103, and F_t can be directly substituted into Equation 102, which gives the torque as a function of F_s as presented in Equation 104, F_s depends on the spring conditions and the displacement induced by the cam on the spring, as shown by Equation 105.

$$F_t = F_s \tan\varphi \tag{103}$$

$$T_{cam} = F_s \tan\varphi \, r_{cam} \tag{104}$$

$$F_s = k(r_{cam} - r_{base}) + P \tag{105}$$

$F_s - \ spring\ force[N]$

$r_{base} - cam\ base\ radius\ [m]$

$P - preload\ of\ the\ spring\ [N]$

$k - spring\ stiffness\ \left[\frac{N}{m}\right]$

Based on the defined torque for the cam T_{cam} , $tan\,\varphi$ can be determined using Equation 106. Then, following Equation 107, which arises from the analysis of the diagram in Figure 80, the radius of the cam can be calculated as a function of the crankshaft angle.

$$\tan\varphi = \frac{T_{cam}}{r_{cam}(k(r_{cam} - r_{base}) + P)} \tag{106}$$

$$r_{cam_i} = r_{cam_{i-1}} + \frac{\Delta\theta_{crank}}{2} r_{cam_{i-1}} \tan\varphi_i \tag{107}$$

$\Delta\theta_{crank} - cranckshaft\ angle\ variation\ [rad]$

To convert the previously obtained polar coordinates into cartesian coordinates for better visualization and plotting of the cam, Equations 108 and 109 are used.

$$x_i = r_{cam_i} \cos\left(\frac{\theta_{crank_i}}{2}\right) \tag{108}$$

$$y_i = r_{cam_i} \sin\left(\frac{\theta_{crank_i}}{2}\right) \tag{109}$$

Finally, when integrating a roller follower, including the roller's radius in the cam profile calculation is necessary. This is done using Equations 110 and 111, ensuring the cam profile meets all specified conditions for the roller follower. This crucial step assures that the cam design is effectively customized for the specific follower type in the engine mechanism.

$$x_{r_i} = x_i - r_{roller}\, cos(\left(\frac{\theta_{crank_i}}{2}\right) - \varphi_i) \tag{110}$$

$$y_{r_i} = y_i - r_{roller}\, sin(\left(\frac{\theta_{crank_i}}{2}\right) - \varphi_i) \tag{111}$$

$r_{roller} - \ roller\ radius\ [m]$

The determination of the cam profile relies on the application of kinematic inversion principles in combination with an analysis of the torque profile that the mechanism aims to counteract. By treating the working surface of the cam as fixed and considering the follower's movement relative to this fixed reference, the cam profile can be effectively designed to generate the desired compensatory torque. The design begins with a detailed examination of the torque profile, focusing on fluctuations requiring mitigation.

The characteristics of the spring, particularly its capacity to store or release energy per unit of displacement, are fundamental in determining the required displacement induced by the cam. This displacement is calculated to ensure that the spring effectively stores energy during compression and releases energy during decompression, thereby providing compensatory torque in synchronization with the engine's operational cycle. Using the kinematic inversion approach, the cam's movement is analysed to ensure that the spring is compressed or allowed to decompress in a controlled manner, thus counteracting torque fluctuations and contributing to a more uniform torque output throughout the cycle.

The final cam profile is generated by integrating the specified displacement with design constrains, ensuring that the resulting cam geometry accurately produces the necessary force interactions between the spring and the cam follower.

4.3. Implementation and integration with engine

4.3.1. Balancing mechanism design

A torque profile established from the process described earlier was used. The mechanism and cam, crafted based on equations detailed previously, aim to correct the torque profile illustrated in Figure 75, which represents a Honda® GX 120 engine idle at 1500 RPM. For defining the cam profile, in addition to the torque profile, the input parameters are the spring's stiffness k, spring preload P, initial cam radius r_{base}, and as this mechanism uses a roller follower the radius of the roller r_{roller}; When applied, for easy implementation, the cam will be positioned outside the engine with a reduction ratio of

2:1. Although this solution is characterized by increased friction, it offers a more straightforward approach to creating a functional and robust prototype for practical testing. The prototype was constructed using the torque obtained during the experimental phase of computational validation. This torque profile required a smoothing process due to irregularities caused by the acquisition method. This resulted in segments with extreme accelerations and decelerations, which are artefacts of the acquisition process, making the raw cam profile impractical.

After selecting the torque profile, a spring was designed with characteristics allowing it to produce the desired torque through the mechanism. These characteristics are detailed in Table 6 . Once the spring was detailed, it was necessary to identify a commercially available spring that most closely matched the designed specifications. After selecting a suitable spring, it was tested using a force versus displacement test to determine this stiffness constant. This test was conducted using a Shimadzu® machine shown in Figure 81, with specifications in Table 5; the results obtained for the spring are shown in Figure 82.

Table 5 SHIMADZU® AGS-X main characteristics table.

Characteristic	Description
Model	SHIMADZU® AGS-X
Load Capacity	10 kN
Testing Type	Tensile, Compression, Bending, Shear
Load Cell	High-precision load cell with ±0.5% accuracy
Crosshead Speed	0.001 to 1.000 mm/min
Resolution	1/500 000 of the load cell capacity
Stroke Length	1000 mm
Software	Trapezium X

Figure 81 Experimental determination of spring k using the SHIMADZU® AGS-X.

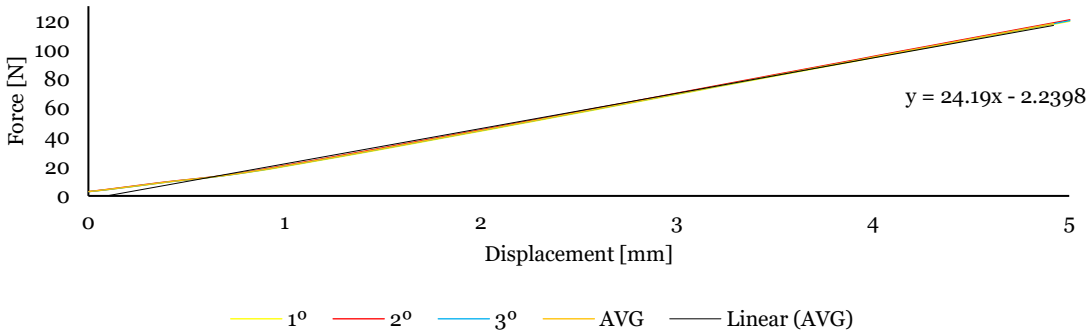

Figure 82 Force versus displacement curve for the spring with 4 mm wire.

Table 6 Spring parameters

Spring characteristics	
Wire diameter	$d = 0.004\ m$
External diameter	$D_{ext} = 0.031\ m$
Internal diameter	$D_{int} = 0.027\ m$
Active coils	$N = 5$
Calculated stiffness constant	$k = 23.4\ kN/m$
Experimental stiffness constant	$k = 24.2\ kN/m$

Following the characterization of the spring, a stiffness constant of 24.2 kN/m was obtained. The spring was subjected to a deformation of 0.01 m in order to achieve the desired preload, resulting in a preload force of 0.0242 kN. Some dimensional constraints were also established for the cam's dimensions to ensure it would not interfere with other

components of the mechanism and to avoid abrupt changes in the cam profile that could lead to mechanical failures. After these considerations, an initial radius of 0.05 m and a follower roller radius of 0.008 m were defined, taking into consideration some design constraints of the mechanism. The initial parameters defined for the cam are summarized in Table 7.

Table 7 Balancing mechanism design parameters.

Cam	Spring
$r_{initial} = 0.05\ m$	$k = 24.2\ kN/m$
$r_{roller} = 0.008\ m$	$P = 0.242\ kN$
$\Delta\theta_{crank} = 10°$	

The cam was constructed based on the torque profile shown in Figure 75, as mentioned before. However, it was observed that the experimentally obtained torque profile could not be directly used, as it exhibited variations induced by the acquisition method, which would lead to an irregular and mechanically impractical cam profile. To mitigate these variations, a moving average of 12 values was applied to the torque profile, which served to smooth the torque profile and, consequently, the cam profile; this variation in the torque profile is demonstrated in Figure 83.

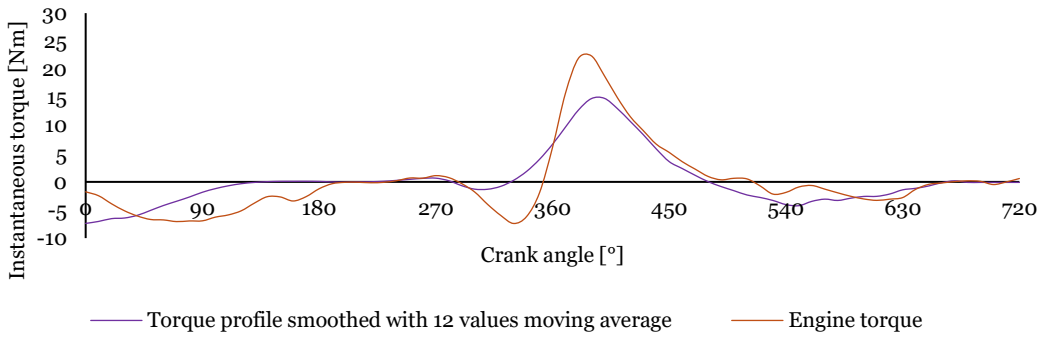

Figure 83 Comparison between experimental instantaneous torque profiles for the Honda® GX 120 engine at 1500 RPM and the same torque profile smoothed by applying a moving average of 12 values. The orange line represents the original torque curve, while the purple line shows the smoothed.

Figure 84 presents the cam geometry in Cartesian coordinates obtained based on the initially defined parameters. A deeper analysis on the cam profile shows three distinct zones; represented in the schematic in Figure 84, it is possible to see that Section 1, in

the 1st quadrant, shows the beginning of a cam profile depression, signifying energy release from the spring to the crankshaft, countering the resistive torque of intake valve opening, and the driving torque of the air-fuel mixture intake. Section 2 highlights a marked decrease in cam radius, associated with compensating the compression process of the air-fuel mixture, with a sharp radius increase towards the end of compression and the start of the expansion; this radius increase continues during the 3rd quadrant, storing energy in the spring from the expansion to utilize during the other strokes. Section 3, located in the 4th quadrant, presents the releasing energy from the spring to the crankshaft, countering the resistive torque of exhaust valve opening, and the driving torque of exhaust process. Additionally, a perfect circumference is depicted by a red dotted line, allowing for a comparison between the cam profile variations and an ideal circle profile.

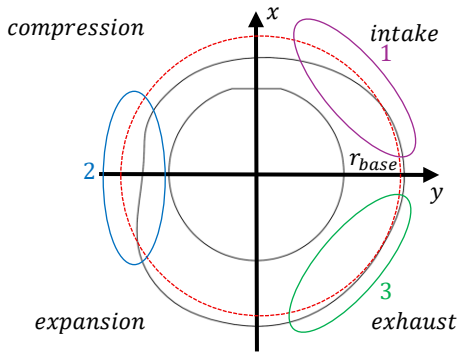

Figure 84 Cam profiles for the balancing mechanism roller follower.

The performance of the balancing cam mechanism is evaluated by analysing the resulting torque profiles after its implementation. The cam is designed based on a smoothed torque profile, which introduces some expected discrepancies but ensures a feasible geometry and the proper functioning of the mechanism; an excessively aggressive cam profile could result in high accelerations of the follower, potentially compromising the reliable operation of the system. However, these discrepancies arise from the cam geometry and the friction present in the mechanism. This friction occurs primarily in the bushings of the follower. A schematic representation of the mechanism is presented in Figure 85, whose design and construction are detailed in Section 4.4.

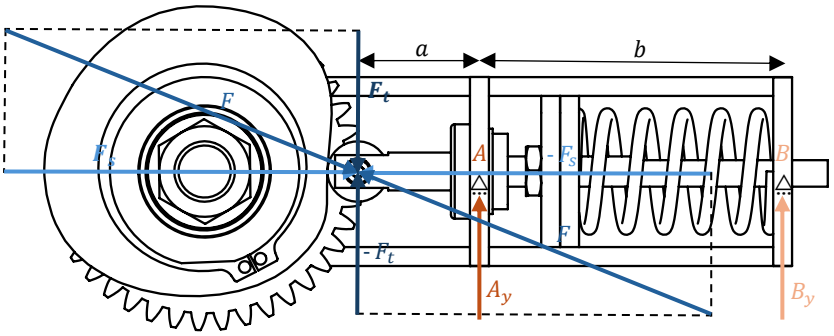

Figure 85 Mechanical model used to analyse support reactions and friction caused by the tangential force F_t.

The mechanism consists of a follower supported at two points, A and B, which are spaced by a fixed distance b equal to 0.08 m. Support A includes a nylon® bushing to reduce friction, while the follower slides directly against a machined steel surface in support B. Support B features a specific geometry to keep the follower aligned with the cam throughout its motion. The reactions at supports A and B depend on the cam geometry, which causes variations in the distance a, measured from support A to the follower's centre. The system was induced to a tangential force F_t applied by the cam, and its effect on the support reactions results in frictional forces that reduce the mechanism's effectiveness.

Using moment equilibrium around each support, the vertical reaction forces at points A and B are determined by Equations 112 and 113:

$$A_y = F_t \frac{a+b}{b} \tag{112}$$

$$B_y = -F_t \frac{a}{b} \tag{113}$$

$A_y - vertical\ reaction\ at\ support\ A\ [N]$

$F_t - \ tangential\ force\ [N]$

$a - distance\ from\ support\ A\ to\ roller\ center, varies\ with\ cam\ radius\ [m]$

$b - distance\ from\ support\ A\ to\ B\ [m]$

$B_y - vertical\ reaction\ at\ support\ B\ [N]$

The corresponding frictional forces at each support are proportional to the reaction forces and the materials in contact, as defined by the equation 114 and 115:

$$F_{friction\,A} = \mu_A A_y \tag{114}$$

$$F_{friction\,B} = \mu_B B_y \tag{115}$$

$F_{friction\,A} - friction\ force\ at\ support\ A\ [N]$

$\mu_A - coefficient\ of\ friction\ between\ steel\ follower\ and\ nylon\ bushing\ bushing$

$F_{friction\,B} - friction\ force\ at\ support\ A\ [N]$

$\mu_B - coefficient\ of\ friction\ between\ steel\ follower\ and\ steel\ support$

The materials in contact and their respective friction coefficients influence the frictional forces at supports A and B. At support A, the interface between the steel follower and the nylon® bushing is characterized by a coefficient of friction, μ_A = 0.03. At support B, where the steel follower slides directly against a steel surface, a coefficient of friction μ_B = 0.20 is commonly assumed to account for potential surface imperfections and operating conditions. The impact of friction on the torque delivered by the mechanism is illustrated in Figure 86. The graph shows the theoretical torque provided by the cam mechanism in the absence of friction, alongside the actual torque delivered when frictional effects at the supports are considered. Additionally, the contribution of friction torque alone is isolated to highlight its influence on the system's performance. The presence of friction reduces the adequate torque delivered by the mechanism, particularly around the power stroke, where follower acceleration and contact forces are highest.

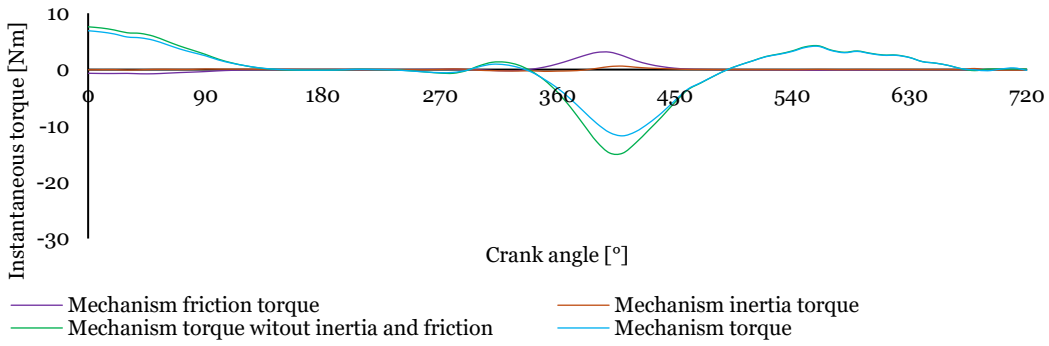

Figure 86 Torque delivered by the balancing mechanism, including the mechanism devolved torque without friction and inertia form follower, the torque considering support friction, the torque form inertia, and the isolated friction torque, and the inertia torque.

The graph in Figure 86 shows the theoretical torque provided by the cam mechanism in the absence of friction, alongside the actual torque delivered when frictional effects at the supports are considered. Additionally, the friction torque component is plotted independently to highlight its influence on system performance. As expected, friction reduces the effective torque delivered by the mechanism, particularly during the power stroke, where follower acceleration and contact forces are higher.

To assess the overall compensation effectiveness, Figure 86 also compares the original torque profile of the engine with the resulting torque after applying the balancing mechanism. The resulting torque curve is obtained by subtracting the mechanism's contribution from the engine torque. A clear reduction in fluctuations is observed, especially during the high-load phases of the cycle.

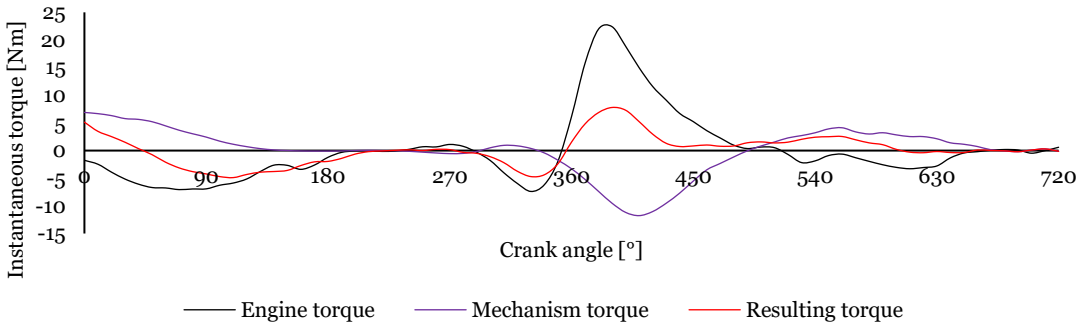

Figure 87 Torque delivered by the balancing mechanism and resulting compensated torque compared to the measured torque profile of Honda® GX 120.

Figure 87 presents the resulting torque profiles after implementing the balancing cam mechanism. The original torque profile of the engine at 1500 rpm is black, highlighting the significant fluctuations, particularly around the power stroke at the 360° crank angle. The compensatory torque provided by the balancing mechanism, illustrated by the purple line, was designed to counter these fluctuations by generating an inverse torque pattern to mitigate the peaks and valleys in the original profile.

This improvement can be quantitatively supported by analysing the standard deviation of the torque signal over a complete engine cycle. Standard deviation is a statistical measure that indicates the amount of variation or dispersion from the mean value. In this context, a lower standard deviation reflects a more stable and uniform torque output, which is desirable for smoother engine operation. The standard deviation of the uncorrected engine torque is 6.25 Nm, while the compensated torque exhibits a significantly lower value of 2.05 Nm. This substantial reduction confirms the

mechanism's effectiveness in attenuating torque peaks and balancing the engine's dynamic behaviour.

The red line in Figure 87 highlights the final resulting torque after applying the balancing mechanism. Figure 87 demonstrates that the balancing cam mechanism can significantly reduce the torque fluctuations in the engine at 1500 rpm. However, due to the need of using a soften torque profile for cam construction, the resulting torque profile only partially eliminates the fluctuations, as the original profile could not be replicated with complete conformity. This approach was necessary to ensure a mechanically feasible cam design, which nonetheless provides a considerable improvement in torque stability.

4.4. Construction of the Balancing cam mechanism

The Honda® GX 120 engine was selected due to its simple design, which allows for its application across a wide range of machinery. The mechanism was designed to be installed at the crankshaft output, typically used to drive various machines. Its design focused on accommodating the characterized spring and cam. Two gears with module 2 were used to achieve a transmission ratio of 2:1. The supporting structure was constructed from 3 mm thick steel plates cut using laser technology and slightly over-dimensioned to facilitate future testing of different springs. This structure supports the mechanism and positions its components to interact effectively. The appendices include detailed drawings of the parts used in the construction of the mechanism. Additionally, a shaft was machined using a lathe, which held the gear to which the cam was attached. This shaft is the intermediary for transmitting movement between the key components, including the cam, follower, spring, and crankshaft.

Figure 88 shows the fully assembled structure of the engine, where the entire setup and the shaft are visible.

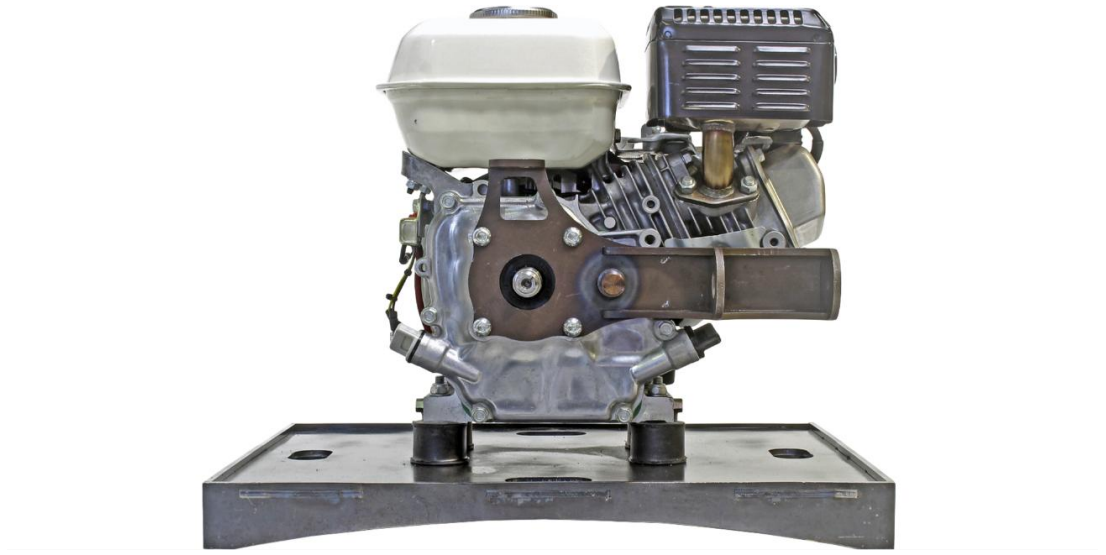

Figure 88 Fully assembled structure of the mechanism with the intermediary shaft, mounted on the Honda ® GX 120 engine.

For the purpose of conducting and measuring the experimental tests, a trigger wheel was designed and attached to the gear existing on the primary shaft. The transmission of motion between the crankshaft and the gear is achieved via a tapered coupling. The subsequent transmission of motion between the gear and the trigger wheel is facilitated through a keyway specifically created in the gear for this purpose. To secure the trigger wheel in place, a retaining ring was used. Figure 89 illustrates the gear with 20 teeth, with the trigger wheel attached and fixed using the retaining ring.

Figure 89 Gear with 20 teeth and the attached trigger wheel.

One of the critical components of the mechanism is the follower, as shown in Figure 90. This roller follower was constructed using a 625-2RS bearing, facilitating contact between the follower and the cam. A distinctive feature of this follower is its threaded section, which allows for the spring preload adjustment. This adjustment is made by tightening the adjuster, which compresses or decompresses the spring in response to the

follower's movement. A friction bushing made of nylon® was developed to minimize friction between the follower and the previously mentioned structure. This bushing is fixed to the mechanism's structure using a retaining ring.

Figure 90 Roller follower with adjustable preload spring, featuring a 625 RS bearing and a nylon® friction bushing.

Figure 91 shows the mechanism structure, along with the 20-tooth gear, the follower mounted on the engine, and the VR sensor. This represents the assembly order of the mechanism. It is necessary to first install the gear on the engine output shaft, followed by the gear that supports the cam. This sequence is required to avoid interference between the trigger wheel and the 40-tooth gear that holds the cam, which would otherwise prevent proper assembly.

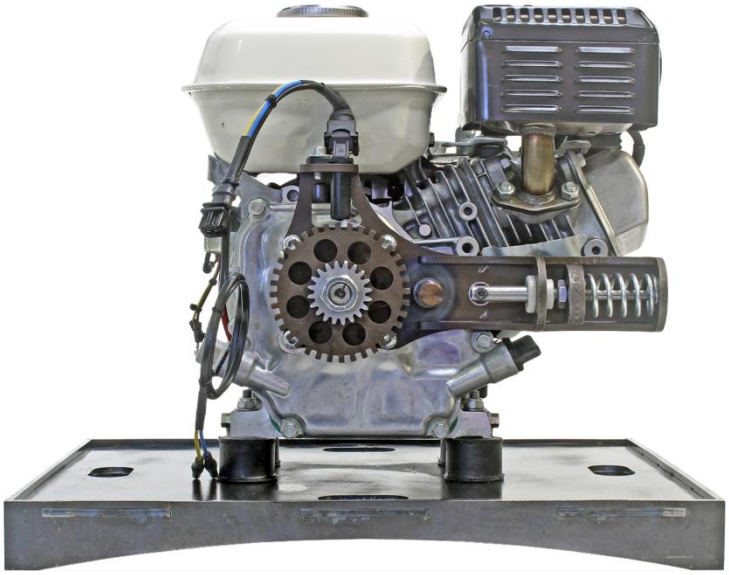

Figure 91 Assembled mechanism on the Honda® GX 120 engine, showing the 20-tooth gear, roller follower with preload spring, and VR sensor.

The 40-tooth gear shown in Figure 92 is the component onto which the cam of the mechanism is mounted. The cam attachment system on the gear is like that used for the trigger wheel, utilizing a keyway and a retaining ring. This design ensures secure attachment while also enhancing the versatility of the prototype, as it allows for easy removal and replacement of the cam. Another feature of this gear is the inclusion of two 6003-2RS bearings on its interior, which facilitate its mounting onto the shaft of the structure. These bearings enable free rotation of the gear relative to the structure, allowing for smooth transmission of movement between the cam mechanism and the engine output shaft.

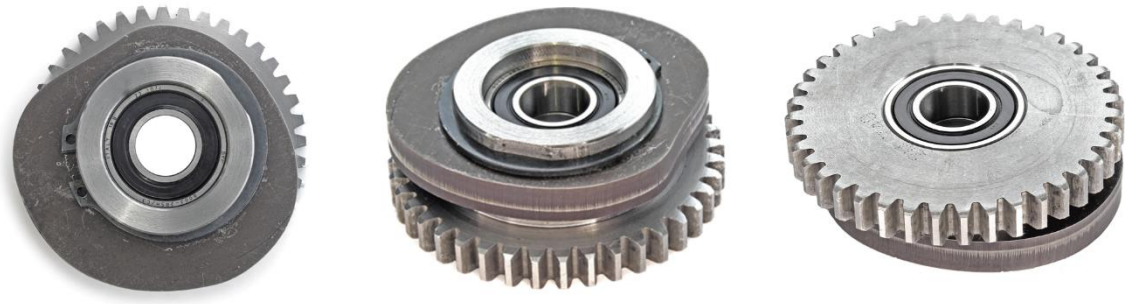

Figure 92 40-tooth gear with mounted cam, featuring a keyway and retaining ring, along with two internal bearings to mount on the mechanism structure shaft.

Figure 93 shows the mechanism fully assembled. After assembling the mechanism, it is essential to proceed with its alignment to ensure perfect synchronization. The alignment process starts by positioning the cam at its smallest radius, corresponding to the section where the engine torque is at its minimum. Then, the engine is set to TDC, which occurs at the end of the compression stroke and the beginning of combustion. To rotate the engine to TDC without moving the mechanism, the nut securing the gear on the engine output shaft is only tightened once proper alignment is verified. Since the connection between the gear and the engine shaft uses a tapered fit, it ensures that the gear rotates in unison with the crankshaft only when fully tightened. At this point, the mechanism is synchronized and securely linked with the engine. Finally, the mechanism's spring preload must be adjusted. This is done by tightening the adjuster to compress the spring. Additionally, a second locking nut is used to prevent the adjuster from loosening, thereby ensuring that the applied spring preload remains stable.

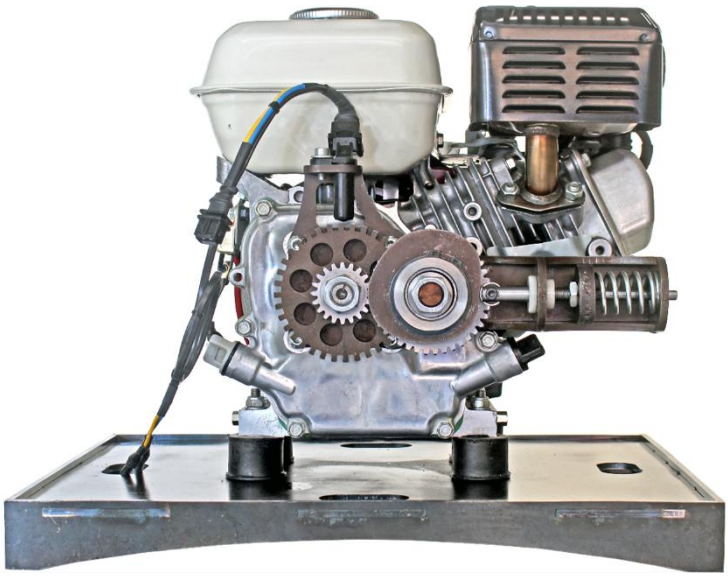

Figure 93 Fully assembled mechanism mounted on the Honda® GX 120 engine, including the 40-tooth gear with mounted cam, 20-tooth gear with trigger wheel, follower, and VR sensor.

4.5. Experimental results

The experimental tests were conducted considering the same procedure as the initial tests, which were performed to validate the simulation and obtain the velocity variation profile that served as the basis for the cam design. The validation tests for assessing the mechanism's effectiveness followed the same procedure used in the initial tests. Specifically, ten measurements were considered for each experiment, and the average of these ten measurements was calculated to reduce laboratory errors and account for possible operational variations in the engine.

Four distinct groups of tests were performed to evaluate the engine's behaviour when operating with the balancing mechanism. The first group of ten tests was conducted without the follower in contact with the CAM. The second group of tests involved the follower acting on the cam, with the spring preload adjusted to the value for which the cam was designed. Subsequently, two additional groups of tests were performed with different preload variations to assess the mechanism's response to changes in spring preload.

4.5.1. Influence of balancing cam mechanism inertia on engine behaviour

To evaluate the influence of the mechanism's inertia on the velocity variation of the engine, experimental tests were conducted with the mechanism assembled on the

engine. However, to ensure no external forces were exerted on the system, the follower was positioned such that it did not come into contact with the cam during these tests.

Figure 94 illustrates the results obtained from 10 tests performed under these specific conditions.

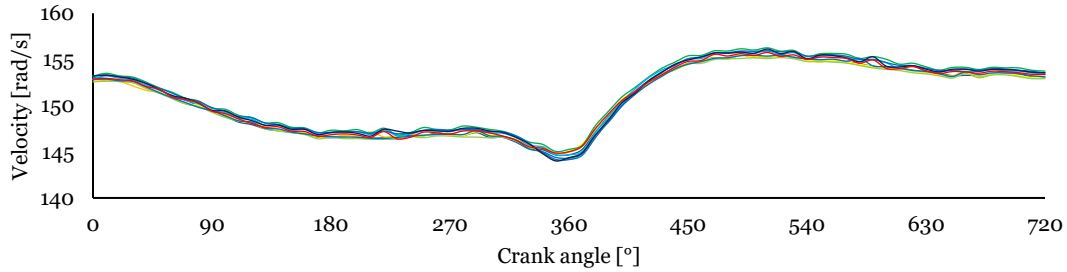

Figure 94 Velocity variation profiles from 10 tests recorded with a VR sensor on a Honda® GX 120 engine. The mechanism was mounted on the engine, and the follower was disengaged from the cam to isolate the system's inherent inertia.

Due to the mechanism's added inertia, there is a small improvement in velocity variation, as seen in Figure 95. Although this improvement is minimal, to isolate only the results associated with the mechanism's operation and not the inertia it generates, all results from this point forward will be compared against the velocity obtained when the mechanism's inertia is taken into account, rather than the initially measured velocity variation.

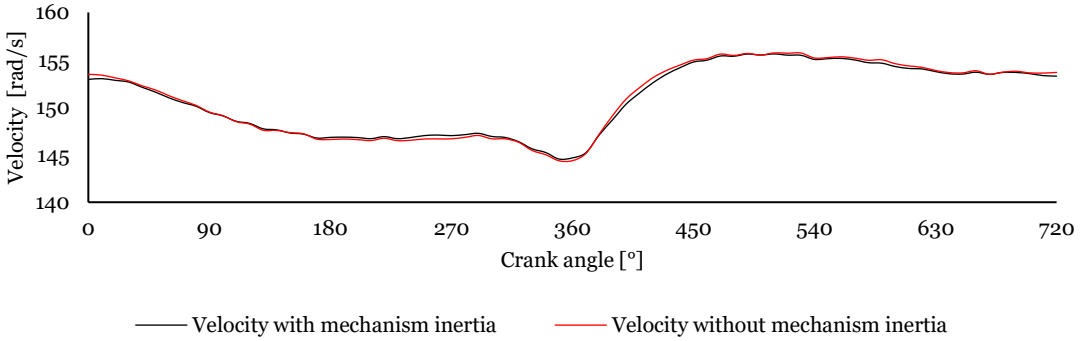

Figure 95 Velocity as a function of crank angle, comparing results obtained with and without the mechanism's inertia.

In an analytical analysis to the results present in Figure 95 the standard deviation from the stock velocity profile is 3.74 rad/s and the added rotational inertia torque profile as standard deviation of 3.58 rad/s.

4.5.2. Influence of balancing cam mechanism actuation on engine behaviour

After evaluating the influence of the mechanism's inertia on engine behaviour, tests were conducted to assess how its actuation affects the engine's angular velocity variation. In this stage, the mechanism was operated under standard conditions, with the spring preload set to 242 N the value originally defined during the cam profile design process to ensure optimal energy storage and release. This test aimed to verify whether the torque delivered by the mechanism effectively compensates for the fluctuations observed in the stock engine configuration. As in earlier procedures, 10 repeated measurements were performed to ensure repeatability and reliability of the results. The recorded velocity profiles obtained under these conditions are presented in Figure 96.

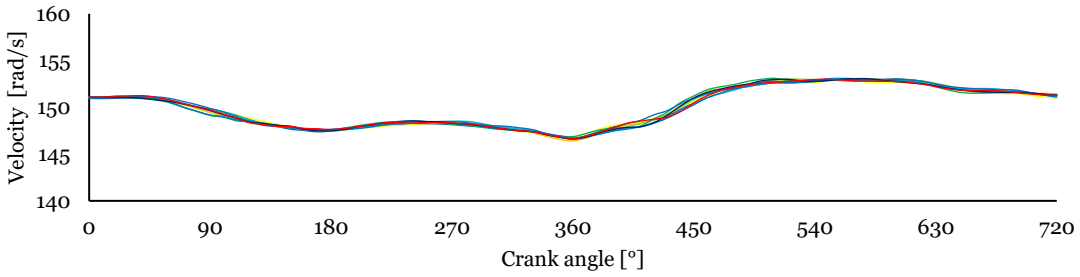

Figure 96 Velocity variation as a function of crank angle for 10 tests performed with the mechanism operating.

The repeated profiles demonstrate consistency between tests, confirming the reproducibility of the system's dynamic behaviour under these conditions. This repeatability indicates that the mechanism operates reliably without introducing uncontrolled variability into the engine's response. To better interpret the impact of the mechanism's actuation, the average velocity profile obtained from these tests is compared in Figure 97 with the profile presented in Figure 95, when the mechanism was installed but not actively engaged. This comparison allows for isolating the torque compensation effect from the influence of the mechanism's inertia.

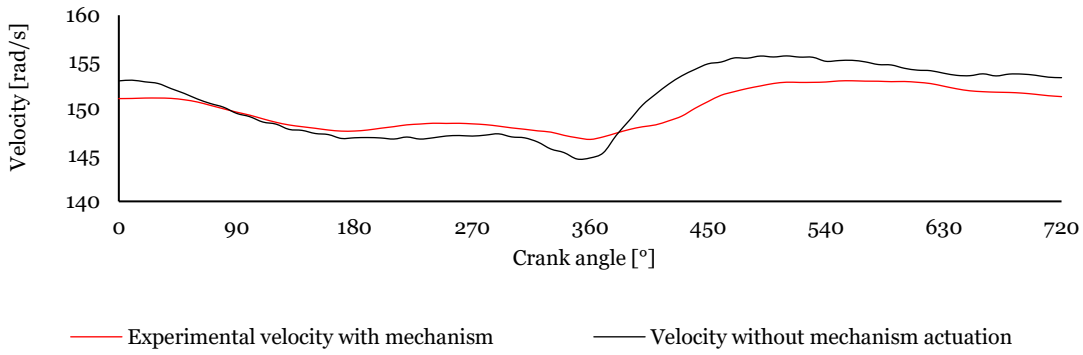

Figure 97 Comparison between the average velocity variation and the profile recorded without the mechanism in operation.

The graph in Figure 97 shows that introducing the mechanism significantly reduces the amplitude of velocity fluctuations throughout the engine cycle. From 0° to 360°, the velocity profile with the cam mechanism exhibits a smoother decrease compared to the profile without active mechanism actuation, particularly during the intake and compression strokes, due to the torque the mechanism delivers to the crankshaft. At 360°, corresponding to the power stroke, the velocity peak is less pronounced when the cam is engaged, indicating a damping effect introduced by the mechanism. Between 360° and 720°, the profile with the mechanism maintains a more stable pattern, whereas the profile without cam action exhibits greater fluctuations during the exhaust and subsequent intake strokes.

These results demonstrate that the mechanism effectively induces torque on the crankshaft and stabilizes velocity variation not due to the small additional inertia it introduces but through the torque actively produced by storing and releasing energy via the spring-cam system. The velocity variation profiles' standard deviation and amplitude were calculated to support this analysis quantitatively. The amplitude represents the difference between the minimum velocity, typically registered at the end of the compression stroke, and the maximum velocity, which occurs near the end of the combustion. The stock configuration, without any compensation, exhibits a standard deviation of 3.58 rad/s and an amplitude of 11.08 rad/s. When the mechanism is engaged, these values are reduced to 2.07 rad/s and 6.30 rad/s.

To explore the influence of preload adjustment, additional tests were conducted with the spring set to 121 N and 363 N values below and above the designed initial preload of 242 N. These tests assessed how deviations from the optimal preload affect the mechanism's ability to stabilize crankshaft velocity.

Figure 98 compares the velocity variation profiles for the three preload conditions against the stock engine configuration, in which the balancing mechanism was not engaged.

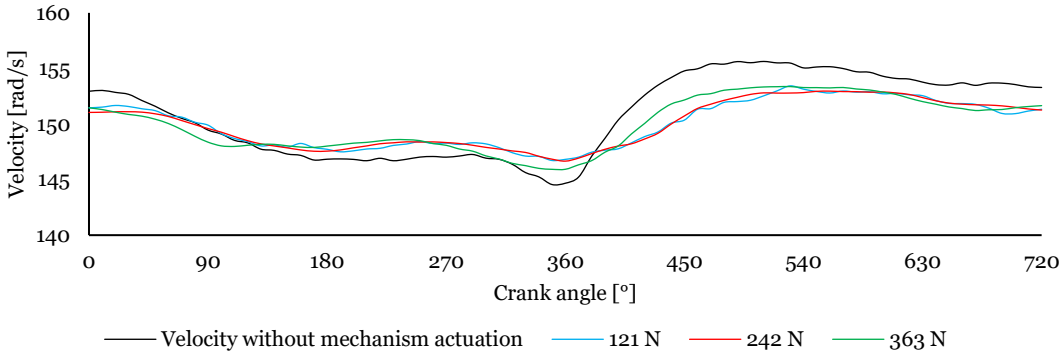

Figure 98 Comparison of velocity variation for different spring preloads (242 N, 121 and 363 N) with the stock velocity variation.

The results clearly show that introducing the mechanism reduces velocity fluctuations, though the spring preload directly influences the degree of improvement. The 121 N and 242 N conditions yield substantial improvements over the uncorrected case, particularly during the intake and compression strokes. Although 242 N was the preload used for cam design, its advantage over 121 N is slight, becoming more noticeable during the compression stroke and in the recovery following the combustion phase.

Conversely, applying a preload of 363 N degrades the performance. The excessive spring force introduces greater mechanical resistance, limiting the mechanism's responsiveness and leading to increased velocity fluctuations compared to the 121 N and 242 N cases. These results indicate that deviations from the designed 242 N preload, whether lower or higher, result in suboptimal stabilization. At 121 N, the reduced energy stored in the spring limits the torque available for compensation. At 363 N, the preload becomes excessive, introducing unwanted resistance and friction that disrupts the force delivery intended by the cam design.

The standard deviation and amplitude of the velocity variation profiles were calculated to support this analysis. The stock engine presents a standard deviation of 3.58 rad/s and an amplitude of 11.08 rad/s. When the mechanism is engaged, these values drop to 2.08 rad/s and 6.72 rad/s at 121 N, 2.07 rad/s and 6.30 rad/s at 242 N, and 2.35 rad/s and 7.45 rad/s at 363 N. The 242 N preload achieves the lowest values in both metrics, validating it as the most effective setting for minimizing velocity fluctuations, these results are quantitatively summarized in Figure 99.

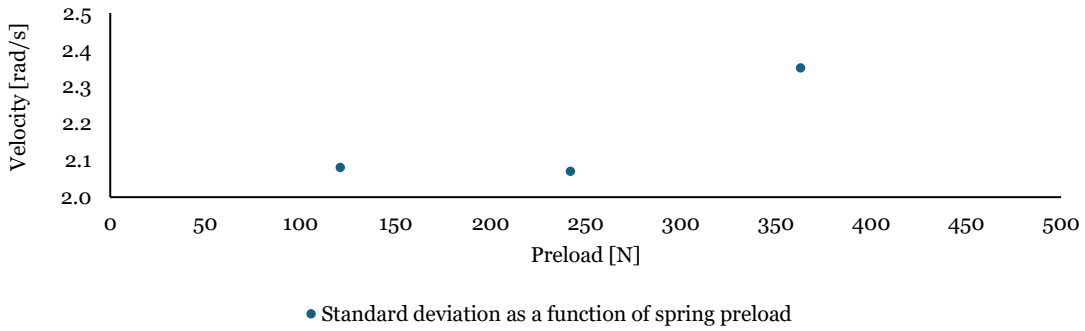

Figure 99 Comparison of crankshaft velocity standard deviation as a function of spring preload (121 N, 242 N, and 363 N).

The influence of the preload P on the torque output of the mechanism can be understood from Equations 104 and 105, which show that the torque is directly proportional to the spring force F_s, given by $F_s = k(r_{cam} - r_{base}) + P$. When the cam radius variation is small such as during the intake and compression strokes the deformation term $k(r_{cam} - r_{base})$ becomes negligible, and F_s, is essentially determined by the preload P. In these regions, the torque generated by the mechanism is more sensitive to the preload. Conversely, in high-torque phases like the expansion stroke, the radius variation increases, and the deformation term $k(r_{cam} - r_{base})$ begins to play a more significant role in the torque delivered by the mechanism. In this case, the combination of a high preload and a substantial deformation results in an elevated spring force, which can lead to excessive reaction forces and increased friction within the mechanism.

Figure 100 illustrates that friction torque increases significantly with higher preload, especially at 363 N, where follower displacement and contact forces are most pronounced during the expansion phase. This frictional loss is directly tied to the increase in tangential force F_t, which grows with the total spring force F_s. According to Equations (112-115), this leads to higher support reaction forces and increased friction at points A and B from mechanism, dissipating part of the energy stored in the spring. As a result, the torque delivered by the mechanism is reduced, particularly in regions where precise compensation is needed. This limits the effectiveness of the correction and directly affects the velocity variation from the engine.

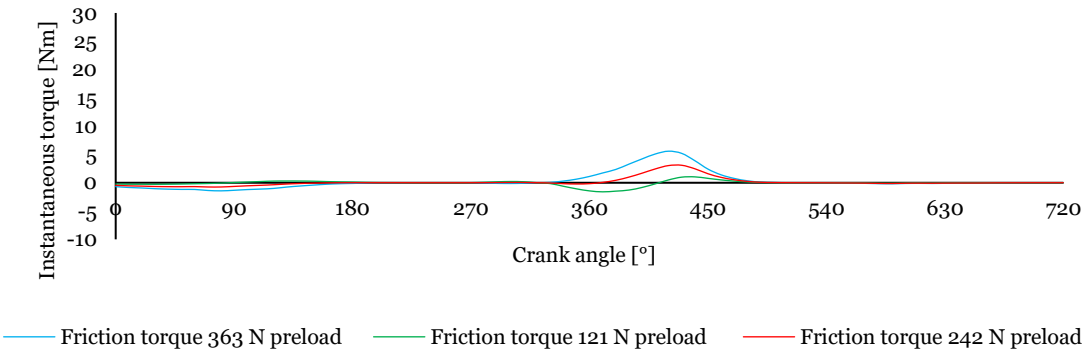

Figure 100 Friction torque generated by the mechanism under preload values of 121 N, 242 N, and 363 N.

While the 242 N preload shows moderate friction with good torque delivery, confirming it as the best balance between compensation and losses, the 121 N preload benefits from reduced internal friction despite its lower energy storage.

4.6. Mechanism performance evaluation and results discussion

To evaluate the balancing mechanism's effectiveness, Figure 101 compares the velocity variation simulated for the engine with the mechanism with the corresponding experimentally measured profile. This analysis aims to verify how closely experimental behaviour replicates the predicted engine dynamics under the same operating conditions.

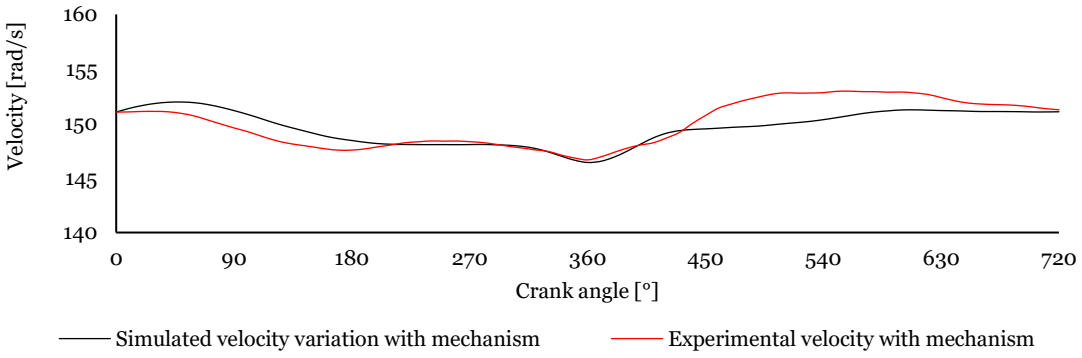

Figure 101 Comparison between the simulated velocity variation for the engine with mechanism actuation and the experimental results obtained.

The curves show that both profiles follow a similar overall trend throughout the engine cycle. In the intake and compression strokes and during the expansion and exhaust phases, the simulated and experimental velocity variations exhibit consistent phase

alignment. However, the experimental profile presents slightly more pronounced fluctuations in specific regions, which can be attributed to minor mechanical imperfections, sensor resolution limits, and assembly tolerances not accounted for in the simulation.

Quantitatively, the standard deviation of the simulated velocity variation is 1.56 rad/s, while the experimental result is slightly higher at 2.07 rad/s. Regarding amplitude, the simulated value reaches 5.54 rad/s, compared to 6.30 rad/s obtained experimentally. Nevertheless, the overall consistency in the trend and magnitude of the profiles confirms that the simulation provides a reliable prediction of the engine's dynamic behaviour when the mechanism is engaged.

Figure 102 compares the experimental corrected with the simulated torque profile. Although the experimental curve shows slightly higher peaks and minor discrepancies in certain phases, the general shape remains consistent. The experimental standard deviation is 3.12 Nm, while the simulated profile shows a slightly lower value of 2.75 Nm. Similarly, the amplitude is 13.66 Nm for experimental data and 12.68 Nm for the simulated result. These differences from simulated to experimental results may be attributed to factors such as assembly misalignments, slight variations in spring characteristics, or non-ideal contact behaviour between components, effects that, although the model includes friction and inertia, are difficult to characterize precisely in simulation. Associated errors from data acquisition, manufacturing tolerances, and dynamic variability in real engine operation also contribute to slight divergence between predicted and measured performance.

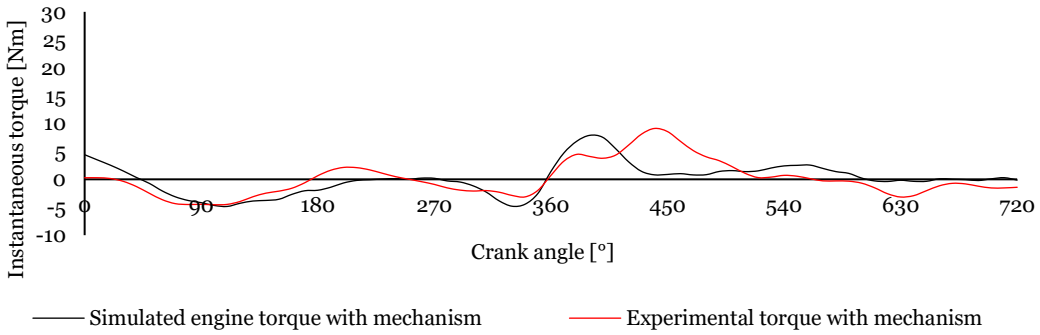

Figure 102 Comparison between the simulated engine torque for the engine with mechanism actuation and the experimental results obtained.

Figure 103 presents and summarizes a direct comparison between the average velocity variation profile obtained with the balancing mechanism engaged and the profile

recorded with the mechanism disengaged. This visualization complements the quantitative analysis provided earlier and offers a clearer understanding of the system's behaviour throughout the engine cycle.

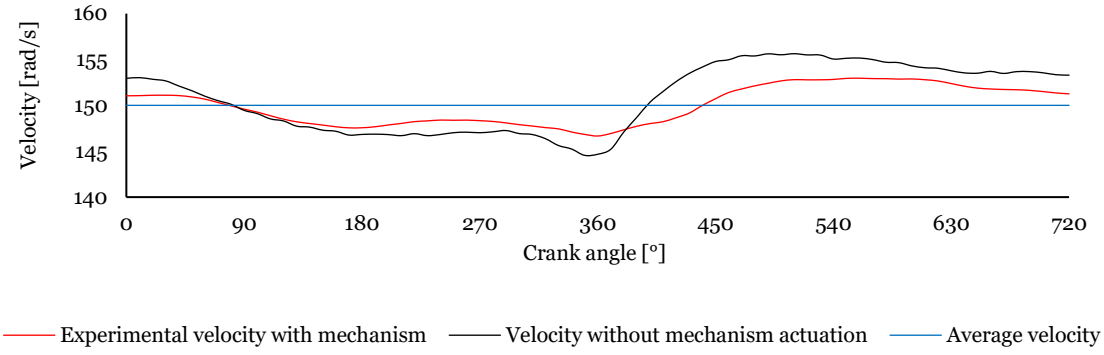

Figure 103 Comparison between average velocity, velocity variation with the balancing mechanism engaged and without mechanism actuation.

The graph in Figure 103 shows that the mechanism effectively reduces velocity fluctuations throughout the entire 720° engine cycle. The corrected velocity profile consistently remains close to the average value. Around 90°, during the intake phase, only minor deviations are observed, which is likely due to the velocity at that point already being near the average, thus requiring minimal correction. In contrast, during the compression phase and especially at the peak of the expansion stroke, the mechanism provides a more pronounced correction. These correspond to regions where the torque demand is higher, aligning with the phases in which the mechanism delivers greater compensating torque. Figure 104 presents the torque profiles with and without mechanism actuation and the average torque.

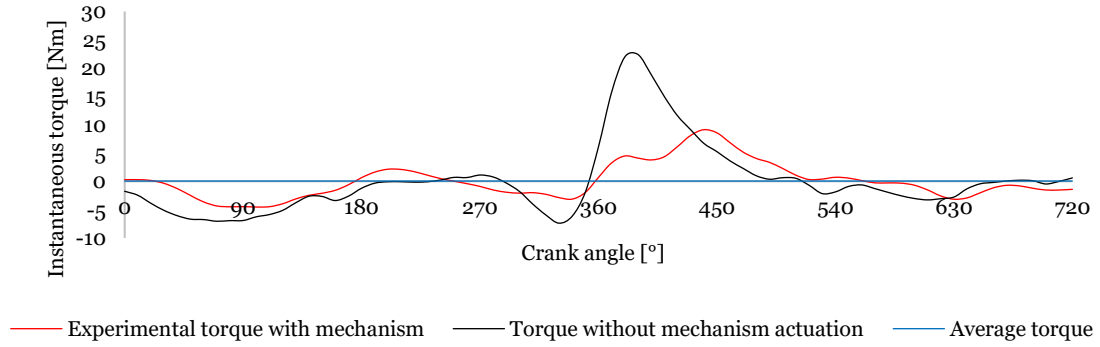

Figure 104 Comparison between average torque, torque with the balancing mechanism engaged and without mechanism actuation.

The graph shows a significant reduction in amplitude compared to the uncorrected profile, especially during the expansion stroke, where the peak torque is notably dampened. Quantitatively, the standard deviation decreases from 6.25 Nm to 3.12 Nm, and the amplitude is reduced from 29.79 Nm to 13.66 Nm, indicating improved regularity and smoother torque delivery.

4.7. Performance improvements and future developments

Recent developments in ICEs technologies have significantly contributed to improving engine performance, enhancing fuel efficiency, and reducing emissions. Traditional ICEs, despite their environmental drawbacks, remain highly relevant due to their widespread use, mature infrastructure, and engineering versatility [6] [7]. The introduction of lightweight mechanical actuators as proposed in this research represents an innovative approach to mitigating torque fluctuations, which are inherent to the intermittent combustion process in ICEs. By storing and releasing energy in sync with engine torque output, these actuators reduce velocity variations and promote smoother operation [11]. Unlike traditional systems such as flywheels, which add mass and inertia, mechanical actuators are compact, adaptive, and capable of dynamic response under variable operating conditions. Their integration could lead to substantial improvements in engine smoothness, efficiency, and emission profiles, particularly in applications requiring precise torque control. The cyclical nature of torque production in ICEs, particularly in single-cylinder configurations, exposes the engine to pronounced fluctuations, which stem from the varying contributions of the intake, compression, expansion, and exhaust strokes. Among these, only the expansion stroke contributes positively to effective power output, while the others impose negative or resistive torque that must be overcome to complete the cycle. These torque irregularities are not only inherent to the thermodynamic operation of reciprocating engines but are further amplified by the slider-crank mechanism, which introduces additional inertial forces based on the mass and geometry of moving components such as pistons, connecting rods, and crankshafts. This dynamic behaviour becomes particularly critical during idle or low-load conditions, where reduced rotational inertia leads to more perceptible speed variations.

The balancing mechanism developed in this investigation demonstrated a clear potential to reduce torque fluctuations during idle operation of single-cylinder internal combustion engines. Simulation results, corroborated by experimental validation, show that the system can significantly soften torque irregularities by delivering a counteracting mechanical response tailored to the cyclic nature of the engine's torque profile. Based on

a spring-loaded cam mechanism, this passive solution effectively mitigates angular speed variations, reduces vibrational noise, and contributes to a more stable idle regime without the drawbacks associated with traditional flywheels [30].

The operation of ICEs is fundamentally governed by cyclical thermal-to-mechanical energy conversion processes, where combustion-induced pressure changes generate torque output across engine cycles. However, these same processes introduce inherent irregularities in torque delivery, particularly in single-cylinder configurations operating at idle. Considering the proposed balancing mechanism within this broader theoretical framework, it becomes clear that such mechanical innovations serve as a natural extension of ongoing efforts to refine engine performance without compromising fundamental thermodynamic efficiency. Historical progression from Otto's pre-compression four-stroke engine to modern high-compression, alcohol-fuelled variants highlights how combustion dynamics and engine geometry have evolved to extract more usable work from thermal processes [45]. Therefore the mitigation of torque fluctuations pursued in this study represents a complementary objective, addressing the dynamic behaviour of the engine's mechanical components rather than changing the combustion process itself [61]. Hence, the mechanical actuator functions not only act as a vibration-damping mechanism but also as an enabler of smoother torque transmission, preserving the integrity of the operating cycle and enhancing the perceived and actual performance of the ICE.

The current implementation is primarily designed for idle conditions. However, as engine load and rotational speed increase, the relative contribution of the balancing mechanism diminishes. This is mainly due to the fixed spring preload and stiffness values, which do not dynamically adapt to changing engine demands. To address this limitation, future iterations of the system should explore the integration of adaptive elements, such as adjustable preloading systems or variable stiffness components, which could be either mechanically or electronically actuated based on real-time operating conditions. Another avenue for development involves material optimization and friction minimization. As the cam and follower system introduces additional resistive torque, selecting low-friction materials and advanced bearing systems could help maintain efficiency and prevent energy losses. Furthermore, the cam profile design methodology can benefit from refinement using higher-resolution torque data, possibly acquired with real-time engine monitoring systems and selective filtering techniques that preserve critical transient features without compromising mechanical feasibility. Despite the positive outcomes, several areas for improvement and future exploration remain to be explored.

Lastly, while this study focused on a single-cylinder configuration, the proposed approach has potential for broader application. Future development should include extending the system to multi-cylinder engines, where inter-cylinder interactions and phase offsets introduce additional complexity in torque harmonization. This could involve the synchronization of multiple balancing cams or the development of distributed correction systems for each cylinder exploring a profile that leads to the multicylinder arrangement.

Looking ahead, the future of ICE development will likely hinge on multi-faceted strategies that combine combustion optimization, electrification, advanced materials, and intelligent control systems. The scalable nature of the mechanical solution explored in this study enables its application across various ICE platforms, including hybrid vehicles, range extenders, and micro-cogeneration systems. Such adaptability enhances its potential impact in reducing greenhouse gas emissions and supports global efforts toward sustainable development and energy efficiency. Future research may explore integration with predictive control systems, sensor networks, and real-time diagnostics, further pushing the boundaries of what ICEs can achieve in an increasingly decarbonized world.

5. Conclusions

5.1. Benefits and advantages of the balancing system

The balancing system developed and analysed in this research offers technical and practical benefits that position it as a viable alternative to conventional torque-smoothing methods in ICEs, particularly for low-speed and idle operation.

One of the principal advantages of the proposed mechanism is its ability to improve rotational smoothness significantly. Integrating the spring-loaded cam mechanism significantly reduces the standard deviation and peak amplitude of the torque and speed profiles. In both simulations and physical tests, the presence of the mechanism yielded the most stable operating conditions, particularly under idle regimes where such fluctuations are most pronounced. These improvements are critical, as they directly impact engine stability, noise, vibration levels, and overall mechanical wear factors, which are often limited in compact or lightweight engine configurations.

The performance gains are noteworthy when contrasted with traditional torque-smoothing solutions such as flywheels or DMFs. While these devices function by storing kinetic energy to buffer against cyclic variations, they introduce considerable mass and inertia into the system. This limits their responsiveness, especially in dynamic load scenarios, and contributes to packaging and efficiency constraints. In contrast, the proposed system is passive and purely mechanical, relying on a synchronized cam profile and a preloaded spring to counteract torque variations. It achieves this with negligible additional mass and without altering the engine's dynamic behaviour during acceleration or deceleration.

Another important benefit resides in the system's mechanical simplicity and integration flexibility. The mechanism is designed to operate without active control, sensors, or feedback loops, making it inherently robust and easy to implement. Its architecture requires no significant structural modifications to the engine, enabling retrofitting or modular integration. This is particularly advantageous in applications where space, weight, and reliability are critical, such as hybrid powertrains, micro-cogeneration units, or portable combustion-based generators. The system's modular nature allows it to be scaled or adapted to different engine architectures with relative ease, broadening its applicability across sectors.

The mechanism also introduces minimal additional complexity from a manufacturing and maintenance standpoint. All components cam, follower, spring, and mountings—

can be fabricated using standard manufacturing processes, and no specialized servicing is required.

Furthermore, the system promotes stability in idle regimes. Reducing rotational oscillations minimizes unburned fuel events and cyclic combustion instabilities that can arise from fluctuating piston speeds and pressures. This indirectly contributes to smoother combustion, more stable idle emissions, overall efficiency, and longer component lifespans—factors increasingly relevant under modern environmental regulations.

In addition to improving operational smoothness and combustion stability, the mechanism also offers structural benefits in terms of component design. Another relevant advantage of the proposed mechanism is its potential to reduce the service factor typically required in the design of components coupled to internal combustion engines. Due to the inherently pulsating torque profile of piston engines, mechanical elements such as shafts, couplings, and gearboxes are often oversized to withstand cyclic loads, requiring elevated service factors that account for irregular torque transmission and vibration. By significantly attenuating these fluctuations, the balancing system developed in this research promotes a smoother and more uniform torque delivery. This reduction in dynamic loading can justify lower service factors during component selection, enabling lighter, more compact, and cost-effective mechanical designs without compromising durability or safety.

5.2. Answers to the research questions

Research conducted throughout this work aimed to understand, model, and mitigate instantaneous torque fluctuations in reciprocating internal combustion engines through a mechanical balancing approach. The following discussion summarises the main findings as direct answers to the research questions formulated in Chapter 1

The first research question explored how to model and quantify instantaneous torque fluctuations in reciprocating internal combustion engines. It also examined how these fluctuations affect angular velocity over the cycle. The total crankshaft torque was broken down into driving, inertia, and resistive components, each as a function of crank angle. A crank-angle-resolved model, using thermodynamic, kinematic, and dynamic approaches, showed that irregularities are greatest between the compression and expansion strokes. They showed that angular-velocity oscillations are cyclic, repeatable,

and proportional to instantaneous torque imbalance. This characterization established the frequency and amplitude targets for the compensating mechanism.

Addressing the second research question considered using a mechanically driven actuator, based on a cam–spring system, to generate compensating torque in opposite phase to the engine's imbalance. This aimed to reduce velocity fluctuations without adding rotational inertia. The actuator stores energy during torque surplus phases and releases it when torque drops, creating a counter-phase effect synchronized with the crankshaft. Numerical and experimental analysis showed that the actuator reduces velocity oscillations. It does so while remaining lightweight and passive. Thus, a purely mechanical system improves rotational regularity without requiring electronic control or active systems.

In response to the third research question focused on which geometric and functional cam–spring parameters most affect torque compensation efficiency and how to optimize them for different working conditions. The study found cam-profile geometry, spring stiffness, and preload force most important. Numerical optimization identified a 242 N preload as the best balance between torque amplitude and mechanical losses. Maintaining phase alignment between compensating torque and torque deficit was critical. Deviating from optimal preload reduced smoothing.

The fourth research question assessed the extent to which experimental results validate the numerical predictions regarding torque-fluctuation reduction and engine-speed stabilization when the balancing cam mechanism is applied. The experimental tests confirmed that the proposed mechanism reduces the amplitude of speed fluctuations in line with simulation results, achieving a measurable decrease in the standard deviation of angular velocity. The observed behaviour closely matched the predicted torque and velocity profiles, validating both the modelling approach and the mechanical feasibility of the design. The mechanism's inertial impact remained negligible, and no additional instability beyond those predicted analytically were observed.

Overall, the findings provide clear answers to the research questions. Torque fluctuations were modelled and validated experimentally; a cam–spring actuator was designed, optimised, and proven effective in reducing rotational irregularities. These outcomes confirm the research hypothesis, showing that a passive mechanical solution can mitigate torque and speed fluctuations while preserving simplicity, reliability, and efficiency.

5.3. Conclusions and future works

This study confirms the effectiveness of the proposed passive balancing cam mechanism in reducing cyclic torque and angular speed fluctuations in single-cylinder internal combustion engines, particularly under idle conditions. Through a combination of theoretical modelling, numerical simulation, and experimental validation, the mechanism demonstrated a clear capacity to smooth out the characteristic irregularities of engine operation by introducing a compensatory mechanical torque. Bridging the gap between classic engine theory and practical mechanical innovation, the developed mechanism actuated by a cam synchronized with the crankshaft, introduces a counteracting mechanical torque aligned with the engine torque cycle. Hence, this solution offers an entirely passive system, requiring no external control, energy input or complex synchronization systems.

Central to the development of this solution a detailed decomposition of engine torque was detailed: driving torque from the pressure force on the piston during combustion, inertia torque from the reciprocating masses, and resistive torque primarily from valve train operation. This modelling revealed that while driving torque is tied to the pressure profile and crankshaft angle, inertia torque scales with the square of engine speed, and resistive torque follows the timing and stiffness of the valve mechanism. These effects are magnified at idle or low rpm, as demonstrated through dynamic equations and pressure-force relationships that show how combustion pressure leads to unbalanced forces and torque pulses, creating operational instability. Such findings reinforce classical insights into the non-uniform generation inherent to Otto and Diesel cycles, where only the expansion stroke actively contributes to propulsion, while the intake compression and exhaust phases introduce negative or resistive torque.

The cam mechanism presented here addresses these issues by targeting the dominant low-frequency components of the torque fluctuation. However, its performance is susceptible to the selected preload and cam geometry, which must be tuned carefully to the engine's dynamic response. As confirmed through analysis and testing, even slight deviations from the optimal preload degrade the phase alignment and amplitude of the compensatory torque, leading to reduced smoothing effectiveness. Moreover, to preserve manufacturability and avoid mechanical infeasibility, it was necessary to soften the torque signal during cam design, which inherently limits responsiveness to rapid transients. This constraint and energy losses from follower inertia and friction, particularly under higher preload conditions, define the practical limits of the mechanism’s performance.

The passive nature of the proposed system, while imposing certain limitations, also represents a significant advantage in simplicity and reliability. Compared with alternative systems previously studied, such as the active switched reluctance machine. SRM-based approach, for instance, achieves torque correction dynamically by absorbing and supplying energy during different engine phases, yet it requires complex electronics, energy storage, and precise synchronization. Nevertheless, the mechanisms practical impact is significant, reducing vibrational noise, improving idle smoothness and enhancing low speed operation, which are key areas where torque irregularities are most disruptive.

This research also aligns with broader trends in advanced engine development. New engine concepts such as downsized configurations, skip-cycle strategies, cylinder deactivation, and the eight-stroke low heat rejection cycle seek to improve fuel efficiency and emissions but face increased challenges with torque irregularity.

This research introduces a theoretically grounded, experimentally validated and mechanically efficient method for addressing torque irregularities in ICEs. By placing a proper solution within a deep understanding of engine dynamics, thermodynamic cycles and mechanical systems behaviour, this investigation contributes not only as a novel actuator but also as a framework to challenge passive energy balancing in combustion-based power.

Looking forward, several directions merit further exploration. Refining the cam profile using high-resolution in-cylinder pressure data and advanced filtering techniques could preserve more of the original torque signal while maintaining a physically feasible design. Reducing internal losses through optimised follower design, low-friction materials, or improved bearing assemblies could also extend operational efficiency. Moreover, incorporating limited adjustability into the preload mechanism thermally, mechanically, or semi-passive actuation could allow real-time adaptation to varying engine loads and operational states. Extending the concept to multi-cylinder platforms may prove complex but promising.

Despite promising results, this investigation highlights several inherent limitations and practical challenges associated with the proposed passive balancing cam mechanism. These considerations not only define the current bounds of the system's applicability but also point toward meaningful avenues for future research and development. Therefore, extending the engine functionality to broader operating conditions such as partial load or transient acceleration. The follower cam interface introduces non-negligible frictional

losses, particularly under high preload forces. The cam profile is inherently limited by manufacturability constraints—such as avoiding discontinuities in curvature or accelerations beyond what typical valvetrain materials can handle. While the single-cylinder configuration provided a controlled environment to isolate and study torque fluctuations, the solution must be re-evaluated for multi-cylinder platforms, where inter-cylinder phasing and overlapping torque pulses add complexity.

In conclusion, this research contributes a technically sound, experimentally supported, and practically relevant solution to the problem of torque irregularity in small internal combustion engines. By building on a foundation of engine dynamics and mechanical design and by situating the mechanism within a broader context of current and emerging engine technologies, this work lays the groundwork for future passive systems capable of enhancing the efficiency, reliability, and applicability of combustion-based powertrains in a changing energy landscape.

6. Contributions

This PhD has led to meaningful scientific and technological contributions in the field of alternative internal combustion engine optimization, particularly in torque fluctuation mitigation. One of the primary outcomes is the structured methodology and content developed throughout the thesis, which together form a solid theoretical and practical framework for analysing instantaneous torque in these engines. By combining analytical tools with simulation and experimental work, the thesis provides a foundation that can support future studies on engine dynamics and torque compensation strategies. These contributions are reflected in two patent applications and seven scientific publications, highlighting the relevance and applied value of the research.

The principal contribution of this work is developing a passive balancing cam mechanism designed to reduce instantaneous torque and angular speed fluctuations in single-cylinder ICEs. This innovation has been protected by a national patent application submitted to the Portuguese Institute of Industrial Property (INPI) under application number 119346, titled "*Método implementado por Computador para a Conceção de um Atuador de Equilíbrio para um Motor, Atuador de Equilíbrio, Programa de Computador e Meio de Leitura Associados*." The patent formalizes the design method, mechanical structure, and computational implementation of the mechanism. It represents a central pillar of this thesis, offering a low-cost, mechanically autonomous, and efficient solution to rotational instability—particularly relevant for small-scale or hybrid engine applications.

A complementary innovation emerged from investigating torque behaviour in alternative engine cycles, leading to the conceptualization and simulation of an eight-stroke low-heat rejection engine. This system is protected under INPI application number 117438, titled "*Ciclo termodinâmico de oito tempos com baixa taxa de rejeição de calor*." Initially driven by observations of increased torque irregularity under unconventional thermodynamic conditions, this work demonstrated a viable method for enhancing thermal efficiency by alternating between fuelled and air-only cycles. However, the pronounced torque variation inherent to this architecture further underscored the relevance of the balancing mechanism introduced in this thesis.

The research has also resulted in a structured body of scientific publications, each of which contributes unique insights to the development of the thesis:

“A Review of Micro and Mild Hybrid Systems”, (DOI: 10.1016/j.egyr.2019.08.077) provides a broad overview of hybridization strategies for ICEs, mapping the current state of energy recovery technologies and identifying the challenges associated with integrating conventional engines into hybrid systems.

“Modulation, Simulation and Analysis of a Switched Reluctance Machine for Flywheel Replacement” (DOI: 10.1007/978-981-32-9531-5_13) introduces an active approach to torque fluctuation correction using a motor-generator unit based on switched reluctance technology. While it demonstrates effective energy management during the engine cycle, the complexity of control systems, power electronics, and energy storage highlights the practical advantages of the more straightforward passive solution developed in this thesis.

“Inertial Dynamometer for Shell Eco-marathon Engine: Validation” (DOI: 10.18502/keg.v5i6.7091) presents the development and experimental validation of a compact inertial dynamometer tailored for testing ultra-efficient engines, such as those used in the Shell Eco-marathon. This work also contributed to the refinement of the data acquisition methodology later employed in the experimental validation phases of this thesis.

“Instantaneous Angular Velocity and Torque on Otto Single-Cylinder Engine: A Theoretical and Experimental Analysis” (DOI: 10.1016/j.egyr.2020.10.031) establishes the analytical and experimental framework; it introduces the methodology for capturing and interpreting instantaneous torque and velocity signals, which underpins the dynamic design and validation of the balancing mechanism.

“8-Stroke Low Heat Rejection Engine” (DOI: 10.1016/j.egyr.2022.01.103) presents the design and simulation of an innovative thermodynamic cycle that reduces energy losses through improved heat retention. Though focused on efficiency, the study revealed severe cyclic torque fluctuations, reinforcing the importance of mechanical stabilization mechanisms in emerging engine designs.

“Intelligent Micro-Cogeneration Systems for Residential Grids: A Sustainable Solution for Efficient Energy Management” (DOI: 10.3390/en16135215) evaluates the integration of ICEs into residential energy systems, emphasizing the role of operational stability for electrical reliability and thermal comfort. In such systems, mainly when operating at a steady speed, the torque stabilization offered by the balancing mechanism is crucial for maintaining frequency stability and reducing mechanical stress.

“An Innovative Mechanical Approach to Mitigating Torque Fluctuations in IC Engines during Idle Operation” (DOI: 10.3390/designs8030047) presents the foundational theoretical and experimental research supporting the balancing cam mechanism. It demonstrates the passive device's effectiveness in reducing torque and velocity fluctuations under idle conditions and validates its relevance for ICE applications where control simplicity and efficiency are prioritized.

“Balancing Cam Mechanism for Instantaneous Torque and Velocity Stabilization in Internal Combustion Engines: Simulation and Experimental Validation” (DOI: 10.3390/en18133256) completes the research narrative by presenting the full implementation of the mechanism on a real engine. It documents the practical aspects of cam design, tuning, and physical integration, finalizing the concept’s technical feasibility and performance impact.

All the scientific works referenced in this section are accessible through the respective DOIs provided. Additionally, proof of submission for the two patent applications mentioned is included in the Annexes, where the official receipts issued by the Portuguese Institute of Industrial Property (INPI) are attached for reference.

References

[1] V. J. Reddy, N. P. Hariram, R. Maity, M. F. Ghazali, and S. Kumarasamy, "Sustainable Vehicles for Decarbonizing the Transport Sector: A Comparison of Biofuel, Electric, Fuel Cell and Solar-Powered Vehicles," *World Electric Vehicle Journal*, vol. 15, no. 3, p. 93, Mar. 2024, doi: 10.3390/wevj15030093.

[2] W. J. Ripple *et al.*, "World scientists' warning of a climate emergency 2021," Sep. 01, 2021, *Oxford University Press*. doi: 10.1093/biosci/biab079.

[3] P. Pal, P. R. C. Gopal, and M. Ramkumar, "Impact of transportation on climate change: An ecological modernization theoretical perspective," *Transp Policy (Oxf)*, vol. 130, pp. 167–183, Jan. 2023, doi: 10.1016/j.tranpol.2022.11.008.

[4] L. Chapman, "Transport and climate change: a review," *J Transp Geogr*, vol. 15, no. 5, pp. 354–367, Sep. 2007, doi: 10.1016/j.jtrangeo.2006.11.008.

[5] F. Leach, G. Kalghatgi, R. Stone, and P. Miles, "The scope for improving the efficiency and environmental impact of internal combustion engines," Jun. 01, 2020, *Elsevier Ltd*. doi: 10.1016/j.treng.2020.100005.

[6] L. M. Oliveri, D. D'Urso, N. Trapani, and F. Chiacchio, "Electrifying Green Logistics: A Comparative Life Cycle Assessment of Electric and Internal Combustion Engine Vehicles," *Energies (Basel)*, vol. 16, no. 23, Dec. 2023, doi: 10.3390/en16237688.

[7] A. Alagumalai, "Internal combustion engines: Progress and prospects," 2014, *Elsevier Ltd*. doi: 10.1016/j.rser.2014.06.014.

[8] I International Energy Agency, Global EV Outlook 2020: Entering the Decade of Electric Drive?, Paris, France: IEA, 2020. [Online]. Available: https://www.iea.org/reports/global-ev-outlook-2020. [Accessed: Mar. 13, 2024].

[9] J. Martins and F. P. Brito, "Alternative fuels for internal combustion engines," Aug. 01, 2020, *MDPI AG*. doi: 10.3390/en13164086.

[10] A. Fayyazbakhsh *et al.*, "Engine emissions with air pollutants and greenhouse gases and their control technologies," Nov. 20, 2022, *Elsevier Ltd*. doi: 10.1016/j.jclepro.2022.134260.

[11] Z. Wang, S. Shuai, Z. Li, and W. Yu, "A review of energy loss reduction technologies for internal combustion engines to improve brake thermal efficiency," Oct. 01, 2021, *MDPI*. doi: 10.3390/en14206656.

[12] L. F. Ineza Havugimana, B. Liu, F. Liu, J. Zhang, B. Li, and P. Wan, “Review of Artificial Intelligent Algorithms for Engine Performance, Control, and Diagnosis,” Feb. 01, 2023, *MDPI*. doi: 10.3390/en16031206.

[13] K. Çağatay Bayindir, M. A. Gözüküçük, and A. Teke, “A comprehensive overview of hybrid electric vehicle: Powertrain configurations, powertrain control techniques and electronic control units,” *Energy Convers Manag*, vol. 52, no. 2, pp. 1305–1313, 2011, doi: 10.1016/j.enconman.2010.09.028.

[14] D. S. Cardoso, P. O. Fael, and A. Espírito-Santo, “A review of micro and mild hybrid systems,” in *Energy Reports*, Elsevier Ltd, Feb. 2020, pp. 385–390. doi: 10.1016/j.egyr.2019.08.077.

[15] S. T. P. Purayil, M. O. Hamdan, S. A. B. Al-Omari, M. Y. E. Selim, and E. Elnajjar, “Review of hydrogen–gasoline SI dual fuel engines: Engine performance and emission,” Dec. 01, 2023, *Elsevier Ltd*. doi: 10.1016/j.egyr.2023.03.054.

[16] H. Solmaz and H. Karabulut, “A mathematical model to investigate the effects of misfire and cyclic variations on crankshaft speed fluctuations in internal combustion engines,” *Journal of Mechanical Science and Technology*, vol. 29, no. 4, pp. 1493–1500, Apr. 2015, doi: 10.1007/s12206-015-0322-8.

[17] M. Babagiray, H. Solmaz, D. İpci, and F. Aksoy, “Modeling and validation of crankshaft speed fluctuations of a single-cylinder four-stroke diesel engine,” *Proceedings of the Institution of Mechanical Engineers, Part D: Journal of Automobile Engineering*, vol. 236, no. 4, pp. 553–568, Mar. 2022, doi: 10.1177/09544070211026290.

[18] D T. Sinigaglia, M. Martins, and J. Siluk, “Technological forecasting for fuel cell electric vehicle: A comparison with electric vehicles and internal combustion engine vehicles,” *World Patent Information*, 2022, doi: 10.1016/j.wpi.2022.102152.

[19] Z. S. Filipi and D. N. Assanis, “A nonlinear, transient, single-cylinder diesel engine simulation for predictions of instantaneous engine speed and torque,” *J Eng Gas Turbine Power*, vol. 123, no. 4, pp. 951–959, 2001, doi: 10.1115/1.1365122.

[20] A. K. Antonopoulos and D. T. Hountalas, “Effect of instantaneous rotational speed on the analysis of measured diesel engine cylinder pressure data,” *Energy Convers Manag*, vol. 60, pp. 87–95, 2012, doi: 10.1016/j.enconman.2012.01.020.

[21] K. H. Munde, V. K. Mehtre, D. S. Ware, and D. P. Kamble, “Review on Performance of Dual Mass Flywheel over Conventional Flywheel,” *Mathematical*

Statistician and Engineering Applications, vol. 71, no. 1, pp. 496–505, 2022, doi: 10.17762/msea.v71i1.2583.

[22] S. V. Dawange and V. L. Kadlag, "A review paper on vibration analysis of DI engine," *International Journal of Science and Research (IJSR)*, vol. 4, no. 2, pp. 759–761, Feb. 2015, doi: 10.21275/SUB151324.

[23] D. Cardoso, D. Nunes, J. Faria, P. Fael, and P. D. Gaspar, "Intelligent Micro-Cogeneration Systems for Residential Grids: A Sustainable Solution for Efficient Energy Management," *Energies (Basel)*, vol. 16, no. 13, Jul. 2023, doi: 10.3390/en16135215.

[24] V. Mittal, R. Shah, and A. Przyborowski, "Analyzing the Usage of Wankel Engine Technology in Future Automotive Powertrains," *SAE International Journal of Sustainable Transportation, Energy, Environment, & Policy*, vol. 5, no. 2, pp. 13-05-02–0009, Aug. 2023, doi: 10.4271/13-05-02-0009.

[25] U. Schaper, O. Sawodny, T. Mahl, and U. Blessing, "Modeling and torque estimation of an automotive dual mass flywheel," *Proceedings of the American Control Conference*, pp. 1207–1212, 2009, doi: 10.1109/ACC.2009.5160136.

[26] E. Ayana, P. Plahn, K. Wejrzanowski, and N. Mohan, "Active torque cancellation for transmitted vibration reduction of low cylinder count engines," *IEEE Trans Veh Technol*, vol. 60, no. 7, pp. 2971–2977, Sep. 2011, doi: 10.1109/TVT.2011.2159255.

[27] R. Anjum, A. Yar, Q. Ahmed, and A. Bhatti, "Model Based Unified Framework for Detection and Mitigation of Cyclic Torque Imbalance in a Gasoline Engine," *J Eng Gas Turbine Power*, Apr. 2021, doi: 10.1115/1.4049620.

[28] Y. Zhang, X. Zhang, T. Qian, and R. Hu, "Modeling and simulation of a passive variable inertia flywheel for diesel generator," *Energy Reports*, vol. 6, pp. 58–68, Dec. 2020, doi: 10.1016/j.egyr.2020.01.001.

[29] X. Zhang *et al.*, "Modelling and active damping of engine torque ripple in a power-split hybrid electric vehicle," *Control Eng Pract*, vol. 104, Nov. 2020, doi: 10.1016/j.conengprac.2020.104634.

[30] D. Y. Lin, B. J. Hou, and C. C. Lan, "A balancing cam mechanism for minimizing the torque fluctuation of engine camshafts," *Mech Mach Theory*, vol. 108, pp. 160–175, Feb. 2017, doi: 10.1016/j.mechmachtheory.2016.10.023.

[31] V. Arakelian and S. Briot, “Simultaneous inertia force/moment balancing and torque compensation of slider-crank mechanisms,” *Mech Res Commun*, vol. 37, no. 2, pp. 265–269, Mar. 2010, doi: 10.1016/j.mechrescom.2009.11.007.

[32] D. S. Cardoso and P. M. O. Fael, "Modelation, Simulation and Analysis of a Switched Reluctance Machine for Flywheel Replacement," in Lecture Notes in Engineering and Computer Science, Singapore: Springer, 2019, pp. 173–185. doi: 10.1007/978-981-32-9531-5_13.

[33] G. W. Kim and S. C. Shin, “Research on the torque transmissibility of the passive torsional vibration isolator in an automotive clutch damper,” *Proceedings of the Institution of Mechanical Engineers, Part D: Journal of Automobile Engineering*, vol. 229, no. 13, pp. 1840–1847, Nov. 2015, doi: 10.1177/0954407015579296.

[34] Vehicular Technology Society and Institute of Electrical and Electronics Engineers, “Active Torque Ripple Damping in Direct Drive Range Extender Applications: a Comparison and an Original Proposal”, doi: 10.1109/VPPC.2015.7352891.

[35] B. Jianguo, L. Xudong, Z. Ming, and L. Kaixiong, “Design and Optimization for the Main Dimension of Flywheel Motor Based on Torque Density,” in *2018 IEEE 3rd Advanced Information Technology, Electronic and Automation Control Conference (IAEAC)*, IEEE, Oct. 2018, pp. 2156–2162. doi: 10.1109/IAEAC.2018.8577753.

[36] L. Chen, "Nonlinear dynamical model of an automotive dual mass flywheel," Proceedings of the Institution of Mechanical Engineers, Part D: Journal of Automobile Engineering, vol. 229, no. 10, pp. 1339–1349, Oct. 2015. doi: 10.1177/1687814015589533.

[37] D. S. Cardoso, P. O. Fael, and A. Espírito-Santo, “Instantaneous angular velocity and torque on Otto single-cylinder engine: A theoretical and experimental analysis,” *Energy Rep.*, vol. 6, pp. 43–48, Oct. 2020, doi: 10.1016/j.egyr.2020.10.031.

[38] E. Galvagno, M. Velardocchia, A. Vigliani, and A. Tota, “Experimental analysis and model validation of a dual mass flywheel,” *SAE Tech. Paper*, 2015, doi: 10.4271/2015-01-1121.

[39] M. Hässler, T. Fieback, M. Rabe, and M. Ryll, “Clutch Disc with Centrifugal Pendulum Absorber,” *ATZ worldwide*, vol. 118, no. 1, pp. 42–47, Jan. 2016, doi: 10.1365/s40112-016-1118-7.

[40] Q. Li and T. Zhang, “Study on Vibration Damping Characteristics of Centrifugal Pendulum Double Mass Flywheel,” in *DEStech Trans. Comput. Sci. Eng.*, 2018. doi: 10.12783/DTCSE/CMSAM2018/26525.

[41] M. Pfabe and C. Woernle, “Reducing torsional vibrations by means of a kinematically driven flywheel - Theory and experiment,” *Mech Mach Theory*, vol. 102, pp. 217–228, Aug. 2016, doi: 10.1016/j.mechmachtheory.2016.03.011.

[42] D. S. Cardoso, P. O. Fael, P. D. Gaspar, and A. Espírito-Santo, “An innovative mechanical approach to mitigating torque fluctuations in IC engines during idle operation,” *Designs (Basel)*, vol. 8, no. 3, p. 47, 2024, doi: 10.3390/designs8030047.

[43] C. Zhang and J. Yang, *A History of Mechanical Engineering*. Singapore: Springer Singapore, 2020. doi: 10.1007/978-981-15-0833-2.

[44] J. B. Heywood, *Internal Combustion Engines Fundamentals*, First Edit. New York: McGraw Hill Education, 1988.

[45] B. J. Challen and R. A. Baranescu, Diesel Engine Reference Book, 2nd ed. Oxford, U.K.: Butterworth-Heinemann, 1999.

[46] C. Ju, "Analysis of the Research Status of Internal Combustion Engines," Highlights in Science, Engineering and Technology, vol. 53, pp. 214–219, Jun. 2023. doi: 10.54097/hset.v53i.9728.

[47] A. M. K. P. Taylor, “Science review of internal combustion engines,” *Energy Policy*, vol. 36, no. 12, pp. 4657–4667, Dec. 2008, doi: 10.1016/j.enpol.2008.09.001.

[48] J. Lu, “Performance Comparison Between Traditional Internal Combustion Engines and Hybrid Powertrains,” Highlights in Science, Engineering and Technology, vol. 114, pp. 129-135, Oct. 2024. doi: 10.54097/a5ggnc71.

[49] J. Moradi, I. Banagar, S. Mehranfar, A. Mahmoudzadeh Andwari, J. Könnö, and A. Gharehghani, “Advancing combustion technologies and alternative fuels in hybrid electric vehicles: a pathway to high-efficiency, low-emission propulsion systems,” *Future Technology*, vol. 3, no. 4, pp. 42–54, Nov. 2024, doi: 10.55670/fpll.futech.3.4.5.

[50] BHASKARA, “Advanced combustion strategies for improving ic engine efficiency and emissions,” *World Journal of Advanced Research and Reviews*, vol. 17, no. 2, pp. 905–916, Feb. 2023, doi: 10.30574/wjarr.2023.17.2.1444.

[51] J. M. Mazanec, N. S. Vang, and S. L. Kokjohn, “Enabling off-highway diesel engine downsizing and performance improvement using electrically assisted turbocharging,” *International Journal of Engine Research*, vol. 24, no. 9, pp. 4104–4126, Sep. 2023, doi: 10.1177/14680874231181002.

[52] M. Sellnau, M. Foster, K. Hoyer, W. Moore, J. Sinnamon, and H. Husted, “Development of a Gasoline Direct Injection Compression Ignition (GDCI) Engine,” *SAE Int J Engines*, vol. 7, no. 2, pp. 835–851, 2014, doi: 10.4271/2014-01-1300.

[53] O. I. Awad, X. Ma, M. Kamil, O. M. Ali, Z. Zhang, and S. Shuai, “Particulate emissions from gasoline direct injection engines: A review of how current emission regulations are being met by automobile manufacturers,” May 20, 2020, *Elsevier B.V.* doi: 10.1016/j.scitotenv.2020.137302.

[54] BHASKARA, “Comparative study of alternative fuels for sustainable IC engine operation,” *World Journal of Advanced Research and Reviews*, vol. 12, no. 1, pp. 512–520, Oct. 2021, doi: 10.30574/wjarr.2021.12.1.0407.

[55] D. N. L. Huynh *et al.*, “Using hydrogen as potential fuel for internal combustion engines: A comprehensive assessment,” *International Journal of Renewable Energy Development*, vol. 14, no. 1, pp. 83–103, Jan. 2025, doi: 10.61435/ijred.2025.60707.

[56] M. Hofny, N. Ghazaly, A. Shmroukh, and M. Abouelsoud, “The Impact of Alternative Fuels on the Performance and Emissions of Petrol Engines: A Review,” *Journal of Advanced Research in Fluid Mechanics and Thermal Sciences*, vol. 122, no. 1, pp. 118–162, Oct. 2024, doi: 10.37934/arfmts.122.1.118162.

[57] Q. Cheng, A. Muhammad, O. Kaario, Z. Ahmad, and L. Martti, “Ammonia as a sustainable fuel: Review and novel strategies,” Jan. 01, 2025, *Elsevier Ltd*. doi: 10.1016/j.rser.2024.114995.

[58] M. Ayinampudi, “Sustainable Alternatives to Electric Energy: An Exploration of Car Engine Fuels for a Greener Future,” *INTERATIONAL JOURNAL OF SCIENTIFIC RESEARCH IN ENGINEERING AND MANAGEMENT*, vol. 08, no. 10, pp. 1–6, Oct. 2024, doi: 10.55041/IJSREM38286.

[59] R. Stone, *Introduction to Internal Combustion Engines*, Third Edit. London: Macmillan Press, 1999.

[60] C. N. Grimaldi and F. Millo, " Internal Combustion Engine (ICE) Fundamentals ," in *Handbook of Clean Energy Systems*, Wiley, 2015, pp. 1–32. doi: 10.1002/9781118991978.hces077.

[61] J. Martins, *Motores de Combustão Interna*, 4ª Edição. Porto: Publindústria, 2013.

[62] G. P. Blair, *Design and Simulation of Four-Stroke Engines*, First Edit. Warrendale: Society of Automotive Engineers, Inc., 1999.

[63] G. P. Blair, *Design and Simulation of Two-Stroke Engines*, First Edit. Warrendale: Society of Automotive Engineers, Inc., 1996.

[64] T. Janhunen, A. Oy, and M. Larmi, "Increasing the Efficiency of a Two-Stroke Car Diesel Engine," *ATZautotechnology*, vol. 3, no. 5, pp. 60–62, Sep. 2003, doi: 10.1007/BF03246792.

[65] S. Zhu, Y. Gu, H. Yuan, Z. Ma, and K. Deng, "Thermodynamic analysis of the turbocharged marine two-stroke engine cycle with different scavenging air control technologies," *Energy*, vol. 191, p. 116533, Jan. 2020, doi: 10.1016/j.energy.2019.116533.

[66] V. Mejía-Gallón, S. Gomez, D. Estrada Grisales, and M. A. Fula, "6-Stroke water injection engine literature review with an introduction of heat transfer and thermodynamic analysis," May 01, 2024, *Springer Nature*. doi: 10.1007/s13762-023-05404-8.

[67] D. N. Thatoi and S. Gaur, "Design and thermal analysis of six stroke engine," in *Materials Today: Proceedings*, Elsevier Ltd, 2021, pp. 540–542. doi: 10.1016/j.matpr.2021.03.704.

[68] A. Omanovic, N. Zsiga, P. Soltic, and C. Onder, "Increased internal combustion engine efficiency with optimized valve timings in extended stroke operation," *Energies (Basel)*, vol. 14, no. 10, May 2021, doi: 10.3390/en14102750.

[69] D. S. Cardoso and P. O. Fael, "8-stroke low heat rejection engine," *Energy Reports*, vol. 8, 2022, doi: 10.1016/j.egyr.2022.01.103.

[70] H. M. Mnati, M. Hammami, O. Ksentini, M. S. Abbes, M. Haddar, and M. M. Hanon, "Kinematic and vibration analysis of a single-cylinder engine: Effects of connecting rod length, fuel type, and engine speed," *International Review of Applied Sciences and Engineering*, vol. 16, no. 2, pp. 331–345, Jun. 2025, doi: 10.1556/1848.2025.00944.

[71] V. Ganesan, *Internal Combustion Engines*, Third Edit. New Delhi: Tata McGraw Hill, 2002.

[72] F. Brunetti, *Motores de combustão interna: Volume 1*, 1st ed. São Paulo: Edgard Bl"ucher, 2012.

[73] J. Guo, W. Zhang, and D. Zou, "Investigation of dynamic characteristics of a valve train system," *Mech Mach Theory*, vol. 46, no. 12, pp. 1950–1969, Dec. 2011, doi: 10.1016/j.mechmachtheory.2011.07.014.

[74] C. J. Kim, Y. J. Kang, B. H. Lee, and H. J. Ahn, "Determination of optimal position for both support bearing and unbalance mass of balance shaft," *Mech Mach Theory*, vol. 50, pp. 150–158, Apr. 2012, doi: 10.1016/j.mechmachtheory.2011.11.006.

[75] N. D. Manring and M. Ali, "Modeling the Inertial Torque Imbalance Within an Internal Combustion Engine: Quantifying the Equivalent Mass Approximation," *J Dyn Syst Meas Control*, vol. 140, no. 7, Jul. 2018, doi: 10.1115/1.4039282.

[76] K. M. Tsitsilonis and G. Theotokatos, "Engine malfunctioning conditions identification through instantaneous crankshaft torque measurement analysis," *Applied Sciences (Switzerland)*, vol. 11, no. 8, Apr. 2021, doi: 10.3390/app11083522.

[77] Jr. G. R. P. J. E. S. John J. Uicker, *Theory of Machines and Mechanisms*, 5th ed. New York: Oxford University Press, 2017.

[78] R. G. Budynas and J. K. Nisbett, *Shigley's Mechanical Engineering Design*, 9th ed. New York, NY, USA: McGraw-Hill, 2010.

[79] E. Rostek, M. Babiak, and E. Wróblewski, "The Influence of Oil Pressure in the Engine Lubrication System on Friction Losses," *Procedia Eng*, vol. 192, pp. 771–776, 2017, doi: 10.1016/j.proeng.2017.06.133.

[80] A. S. Kolekar, A. V. Olver, A. E. Sworski, and F. E. Lockwood, "Windage and Churning Effects in Dipped Lubrication," *J Tribol*, vol. 136, no. 2, Apr. 2014, doi: 10.1115/1.4025992.

[81] Y. Dai, C. Yang, H. Liu, and X. Zhu, "Analytical and Experimental Investigation of Windage–Churning Behavior in Spur, Bevel, and Face Gears," *Applied Sciences*, vol. 14, no. 17, p. 7603, Aug. 2024, doi: 10.3390/app14177603.

[82] G. Mastrangelo, D. Micelli, and D. Sacco, "Extreme Downsizing by the two-cylinder gasoline engine from fiat," *ATZautotechnology*, vol. 11, no. 1, pp. 18–25, 2011, doi: 10.1365/s35595-011-0006-7.

[83] M. M. Namar, O. Jahanian, R. Shafaghat, and K. Nikzadfar, "Engine Downsizing; Global Approach to Reduce Emissions: A World-Wide Review," *HighTech and*

Innovation Journal, vol. 2, no. 4, pp. 384–399, Dec. 2021, doi: 10.28991/HIJ-2021-02-04-010.

[84] L. Chen, W. Shi, and Z. Chen, "Modeling and Experimental Study on Dynamic Characteristics of Dual-Mass Flywheel Torsional Damper," *Shock and Vibration*, vol. 2019, no. 1, Jan. 2019, doi: 10.1155/2019/5808279.

[85] V. Berbyuk, "Weight-Vibration Pareto Optimization of a Dual Mass Flywheel," *Journal of Mathematical Sciences*, vol. 263, no. 1, pp. 1–14, May 2022, doi: 10.1007/s10958-022-05917-6.

[86] R. Zeng, Z. F. Jiang, and X. Wan, "Frequency Response Analysis of Damped Dual Mass Flywheel," *Applied Mechanics and Materials*, vol. 724, pp. 271–274, Jan. 2015, doi: 10.4028/www.scientific.net/AMM.724.271.

[87] L. P. Zeng, L. Q. Song, and J. D. Zhou, "Design and elastic contact analysis of a friction bearing with shape constraint for promoting the torque characteristics of a dual mass flywheel," *Mech Mach Theory*, vol. 92, pp. 356–374, Oct. 2015, doi: 10.1016/j.mechmachtheory.2015.06.002.

[88] L. Chen, W. Shi, and Z. Chen, "Research on Damping Performance of Dual Mass Flywheel Based on Vehicle Transmission System Modeling and Multi-Condition Simulation," *IEEE Access*, vol. 8, pp. 28064–28077, 2020, doi: 10.1109/ACCESS.2019.2951618.

[89] C. Greco, P. Kotak, L. Pagnotta, and C. Lamuta, "The evolution of mechanical actuation: from conventional actuators to artificial muscles," *International Materials Reviews*, vol. 67, no. 6, pp. 575–619, Aug. 2022, doi: 10.1080/09506608.2021.1971428.

[90] K. Chan, A. Ordys, K. Volkov, and O. Duran, "Comparison of engine simulation software for development of control system," 2013, *Hindawi Limited*. doi: 10.1155/2013/401643.

[91] T. De Cuyper, S. Broekaert, K. Chana, M. De Paepe, and S. Verhelst, "Evaluation of empirical heat transfer models using TFG heat flux sensors," *Appl Therm Eng*, vol. 118, pp. 561–569, 2017, doi: 10.1016/j.applthermaleng.2017.02.049.

[92] G. C. Mavropoulos, "Experimental study of the interactions between long and short-term unsteady heat transfer responses on the in-cylinder and exhaust manifold diesel engine surfaces," *Appl Energy*, vol. 88, no. 3, pp. 867–881, 2011, doi: 10.1016/j.apenergy.2010.09.018.

[93] C. D. Rakopoulos and G. C. Mavropoulos, “Experimental evaluation of local instantaneous heat transfer characteristics in the combustion chamber of air-cooled direct injection diesel engine,” *Energy*, vol. 33, no. 7, pp. 1084–1099, 2008, doi: 10.1016/j.energy.2008.02.003.

[94] L. Fonseca, P. Olmeda, R. Novella, and R. M. Valle, “Internal Combustion Engine Heat Transfer and Wall Temperature Modeling: An Overview,” *Archives of Computational Methods in Engineering*, vol. 27, no. 5, pp. 1661–1679, Nov. 2020, doi: 10.1007/s11831-019-09361-9.

[95] F. P. Beer, E. Russell Johnston, P. J. Mazurek David F and Cornwell, and B. Self, *Vector mechanics for engineers: Statics and dynamics*, 11th ed. New York, NY: McGraw-Hill Professional, 2016.

Appendices

- Proof of patent submission: "*Ciclo termodinâmico de oito tempos com baixa taxa de rejeição de calor*" - INPI - 117438
- Proof of patent submission: "*Método implementado por computador para a conceção de um atuador de equilíbrio para um motor, atuador de equilíbrio, programa de computador e meio de leitura associados*" – INPI – 119346
- Assembly drawings of the balance cam mechanism.

instituto nacional da propriedade industrial

Campo das Cebolas - 1149-035 Lisboa - Portugal
NIF: 600017583 / Tel: +351 218 818 100 / Linha de atendimento: 808 200 689 / Fax: +351 218 875 308 / Fax: +351 218 860 066 / E-mail: serviço.publico@inpi.pt / https://inpi.justica.gov.pt/

Nº REQUERIMENTO	CÓDIGO	DATA E HORA DE RECEÇÃO	MODALIDADE	PROCESSO RELACIONADO
20212002507168	0199	01/09/2021 14:30:48	PAT	

PATENTE, MODELO DE UTILIDADE, CCP OU TOPOGRAFIA DE PRODUTOS SEMICONDUTORES (OUTROS ATOS)

1 REQUERENTE

Código 2251976 **Nacionalidade** PORTUGUÊS

Nome UNIVERSIDADE DA BEIRA INTERIOR

Endereço CONVENTO DE SANTO ANTÓNIO

Localidade COVILHÃ **Código Postal** 6201-001

País PORTUGAL

Telefone **Telemóvel** **Fax**

Actividade(CAE) 80300

NIF 502083514

2 MODALIDADE

Modalidade: Pedido de patente

3 TÍTULO OU EPÍGRAFE

Ciclo termodinâmico de oito tempos com baixa taxa de rejeição de calor

4 RESUMO

A presente invenção diz respeito a um ciclo termodinâmico de 8 tempos com baixa taxa de rejeição de calor para motores de combustão interna. Este ciclo é caracterizado por realizar 8 tempos de funcionamento ao longo de um ciclo motor, por ter uma taxa de rejeição de calor baixa uma vez que utiliza uma segunda admissão de ar para o arrefecimento do motor recuperando assim algum do calor que seria dissipado no sistema de arrefecimento do motor e pela sua fácil implementação uma vez que recorre a um motor alternativo convencional. Este ciclo funciona segundo os 4 tempos convencionais realizados ao longo dos 720 graus de rotação da cambota do motor (admissão, compressão, expansão e escape), mas difere deste pelo facto de realizar um segundo ciclo perfazendo 1440 graus de rotação da cambota em que no tempo de admissão, ao invés da admissão da mistura combustível/ar, admite apenas ar, que retira calor das paredes do cilindro.

5 FIGURA DE PUBLICAÇÃO

6 INVENTORES

Nome completo : DANIEL FILIPE DA SILVA CARDOSO

Morada : ESTRADA DA RAMALHOSA, LOTE 50, R/C POST. DIRT.

Localidade : VISEU **Código Postal :** 3505-514

País : PORTUGAL

Telefone 275329146 **Telemóvel** **Fax**

Email silva.cardoso@ubi.pt

NIF : 258446366

inpi instituto nacional da propriedade industrial

Campo das Cebolas - 1149-035 Lisboa - Portugal
NIPC: 600017583 / Tel: +351 218 818 100 / Linha de atendimento: +351 218 818 188 / Fax: +351 218 869 308 / E-mail: servico.publico@inpi.pt / https://inpi.justica.gov.pt/

Nº REQUERIMENTO	CÓDIGO	DATA E HORA DE RECEÇÃO	MODALIDADE	PROCESSO RELACIONADO
20242005959752	0199	22/03/2024 15:21:22	PAT	

PEDIDO DE PATENTE, MODELO DE UTILIDADE OU DE TOPOGRAFIA DE PRODUTOS SEMICONDUTORES

1 REQUERENTE

Código 2251976 **Nacionalidade** PORTUGUÊS (PT)

Nome UNIVERSIDADE DA BEIRA INTERIOR

Endereço CONVENTO DE SANTO ANTÓNIO

Localidade COVILHÃ **Código Postal** 6201-001

País PORTUGAL

Telefone **Telemóvel** **Fax**

Actividade(CAE) 80300

NIF 502083514

Tipo de Representação Agente Oficial de Propriedade Industrial

Código 600046 **Nacionalidade** (PT)

Nome TIAGO ANDRÉ DELGADO REIS NOBRE

Endereço ALAMEDA DOS OCEANOS, 41K-21 - PARQUE DAS NAÇÕES

Localidade PARQUE DAS NAÇÕES **Código Postal** 1990-207

País PORTUGAL

Telefone **Telemóvel** **Fax**

NIF 192633619

Exclusivo para este ato? Não

2 MODALIDADE

Modalidade Pedido de patente

3 TÍTULO OU EPÍGRAFE

MÉTODO IMPLEMENTADO POR COMPUTADOR PARA A CONCEÇÃO DE UM ATUADOR DE EQUILÍBRIO PARA UM MOTOR, ATUADOR DE EQUILÍBRIO, PROGRAMA DE COMPUTADOR E MEIO DE LEITURA ASSOCIADOS

4 RESUMO

A invenção refere-se a um método implementado por computador para determinar um perfil exterior ideal de um came (11). A invenção refere-se também a um mecanismo atuador de equilíbrio (10) incorporando o came (11) que exige um perfil exterior (20) determinado pelo método implementado por computador e um orifício (16) de árvore de cames ou de eixo de cambota (121). O mecanismo atuador de equilíbrio compreende ainda um seguidor (12) conectado a um pistão de mola (14) que por sua vez está adaptado para comprimir a mola (13) que armazena energia e entrega energia à árvore de cames ou ao eixo da cambota onde o mecanismo atuador de equilíbrio (10) está instalado. O pistão de mola (14) e a mola (13) estão alojados numa estrutura de alojamento de mola (15). A invenção refere-se ainda a um motor compreendendo um mecanismo atuador de equilíbrio (10).

ITEM NO.	DESCRIPTION	QTY.
1	Support structure - DWG NO. 2	1
2	Bolt – M8 x 20 - 20S	4
3	Switched reluctance sensor - FAE 79094	1
4	Bolt – M6 x 4 x 0.7 x 10 - Hex SHCS	1
5	Follower assembly - DWG NO. 3	1
6	20-Tooth gear with trigger wheel assembly - DWG NO. 4	1
7	40-Tooth gear with cam assembly - DWG NO. 5	1
8	Hex jam nut – M16 - N	2

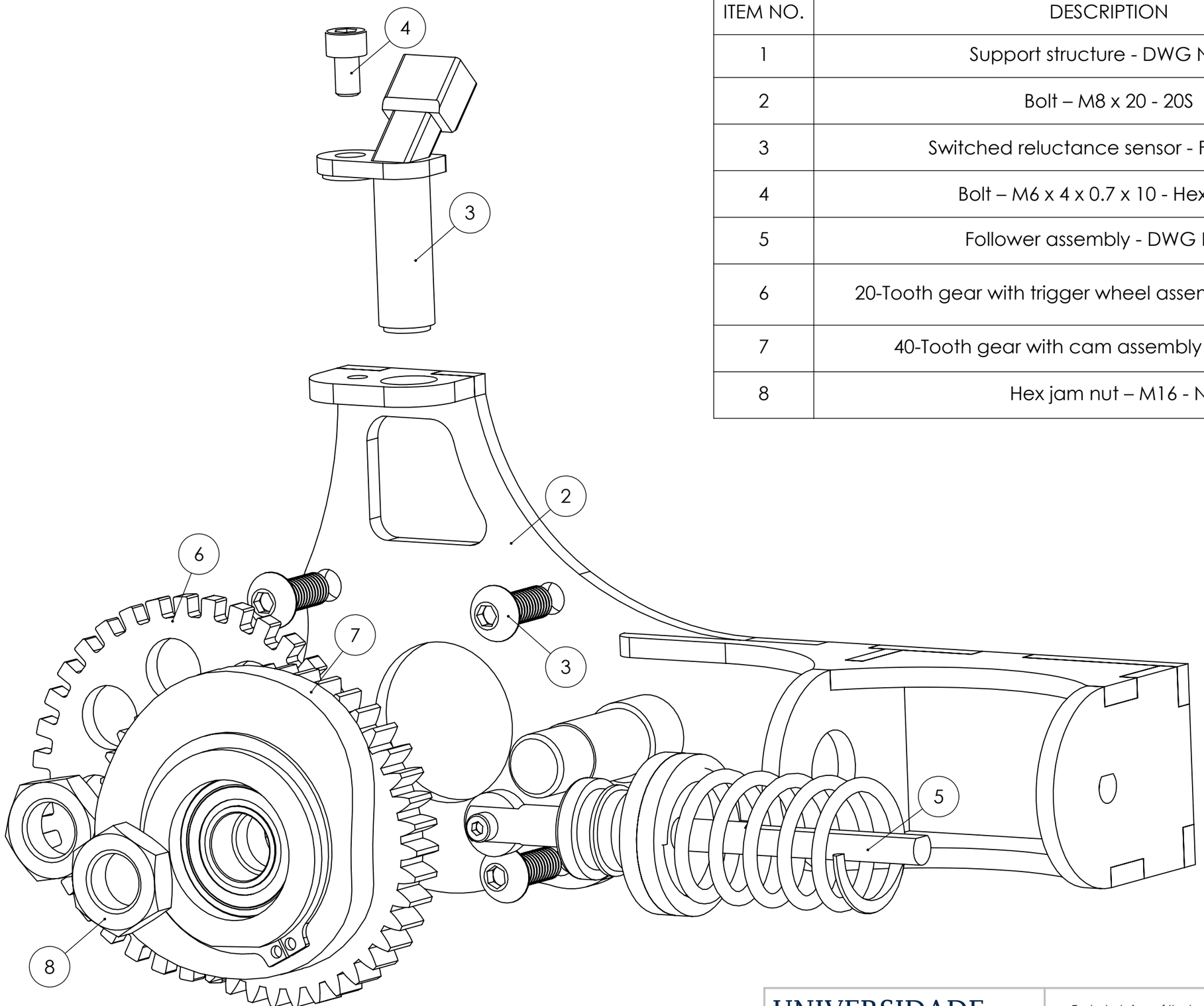

UNIVERSIDADE BEIRA INTERIOR

TITLE: Exploded view of the balancing mechanism.

DWG NO. 1

DESCRIPTION: This drawing presents an exploded view of the complete balancing mechanism assembly, illustrating the various sub-assemblies and fastening elements used. It details components such as the support structure, follower assembly, and gear assemblies, alongside all connecting hardware.

DESIGNER: Daniel Filipe da Silva Cardoso

DATE: 02/07/2024

A3 | SCALE:1:1 | SHEET 1 OF 5

ITEM NO.	DESCRIPTION	QTY.
1	Base plate – 3 mm hot-rolled sheet – Laser cuted	1
2	Lateral plate – 3 mm hot-rolled sheet – Laser cuted	2
3	Sensor support – 3 mm hot-rolled sheet – Laser cuted	1
4	40-tooth gear mounting axle – Steel – Milled	1
5	Rear follower support – 3 mm hot-rolled sheet – Laser cuted	1
6	Front follower support – 3 mm hot-rolled sheet – Laser cuted	1

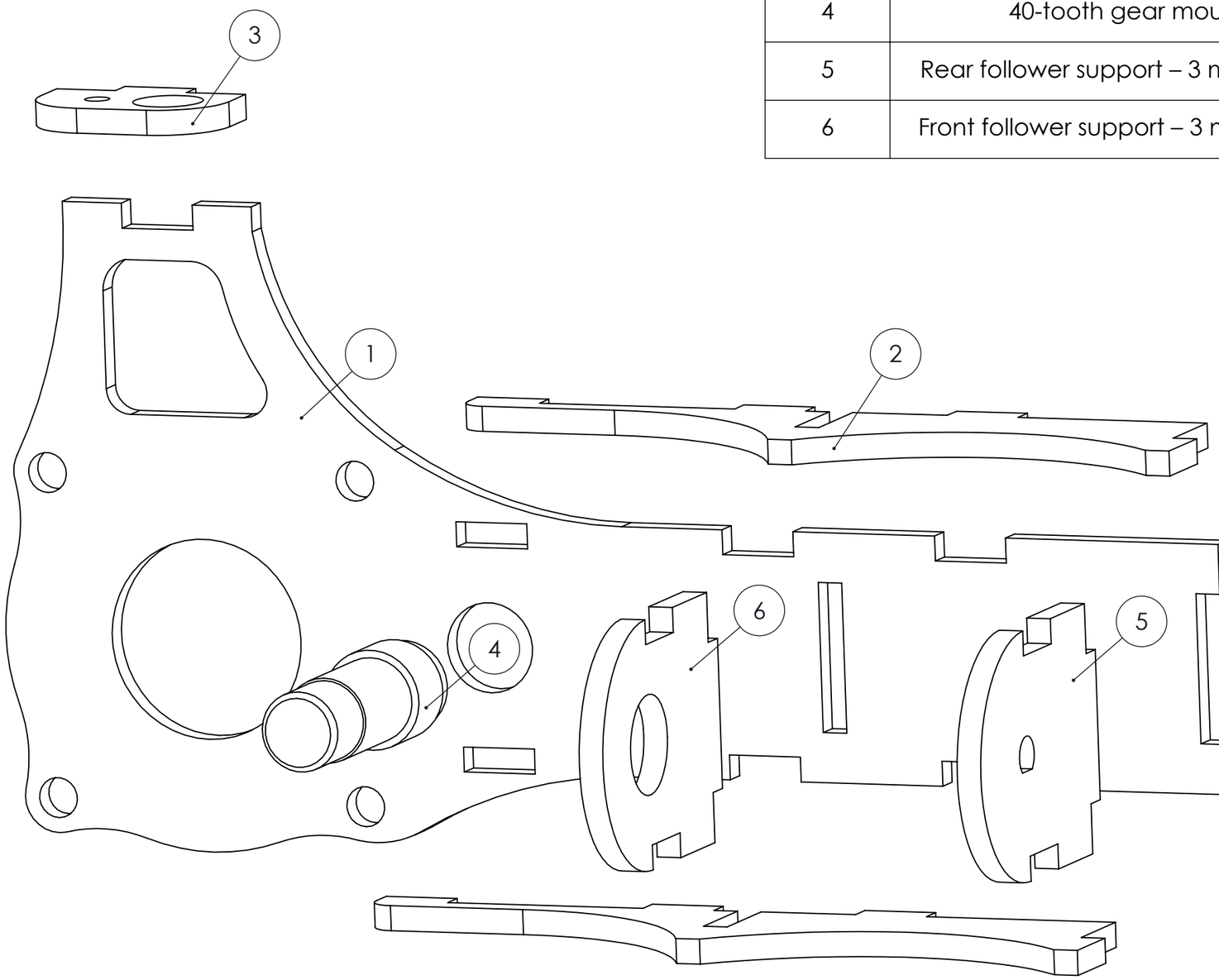

UNIVERSIDADE BEIRA INTERIOR

TITLE: Support structure

DWG NO. **2**

DESCRIPTION: Assembly composed of 3 mm hot-rolled steel sheets, laser cut. The 40-tooth gear mounting axle is machined from solid steel by a turning process. The various plates (base, lateral, support, and sensor bracket) are joined using TIG welding, ensuring structural rigidity and dimensional accuracy for the proper operation of the balancing mechanism.

DESIGNER: Daniel Filipe da Silva Cardoso

DATE: 02/07/2024

A3 | SCALE:1:1 | SHEET 2 OF 5

ITEM NO.	DESCRIPTION	QTY.
1	Follower – Steel – Milled	1
2	Deep-groove ball bearing - 625 RS	1
3	Retaining ring - 3AM1-20	1
4	Hex jam nut – M8 x 1.25 – D-N	1
5	Compression spring – 3 mm wire	1
6	Spring sustainer – 3 mm hot-rolled sheet – Laser cuted	1
7	Bushing – Nylon – Milled	1
8	Bolt – 4 x 0.7 x 10 Hex SHCS – 10NHX	1

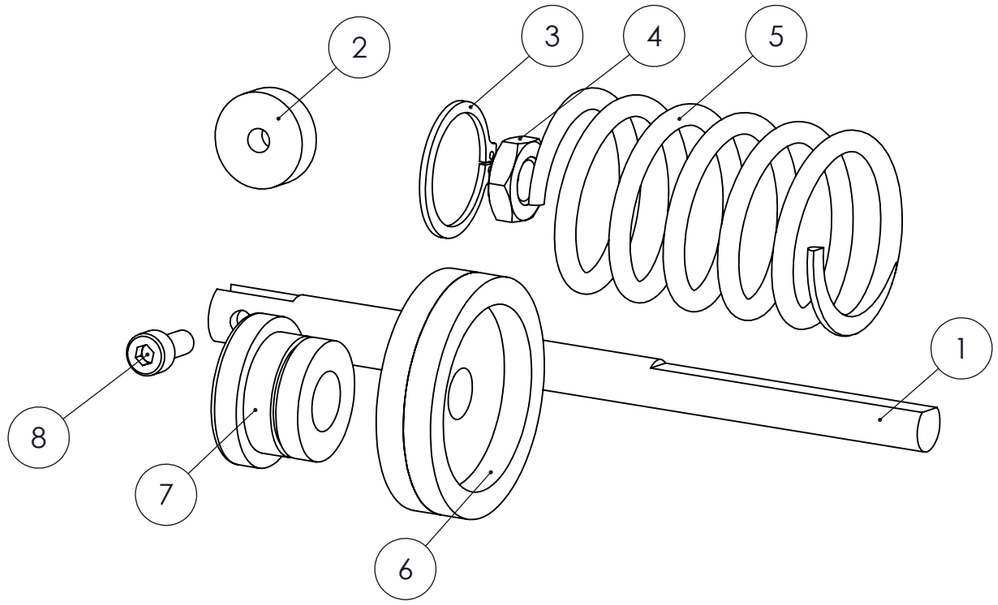

UNIVERSIDADE BEIRA INTERIOR

TITLE: Follower assembly

DWG NO. **3**

DESCRIPTION: Assembly composed of a milled steel follower, deep-groove ball bearing (sealed), retaining ring, hex jam nut, and a compression spring made from 4 mm diameter spring-steel wire. The spring sustainer is manufactured from 3 mm hot-rolled steel sheet and cut by laser. The assembly also includes a machined nylon bushing and a hex socket-head cap screw.

DESIGNER: Daniel Filipe da Silva Cardoso

DATE: 02/07/2024

A3 | SCALE:1:1 | SHEET 3 OF 5

ITEM NO.	DESCRIPTION	QTY.
1	20-Tooth spur gear – M1– Steel – Hub milled	1
2	Trigger wheel – 5 mm hot-rolled sheet – Laser cuted	1
3	Retaining ring - 3AM1-30	1

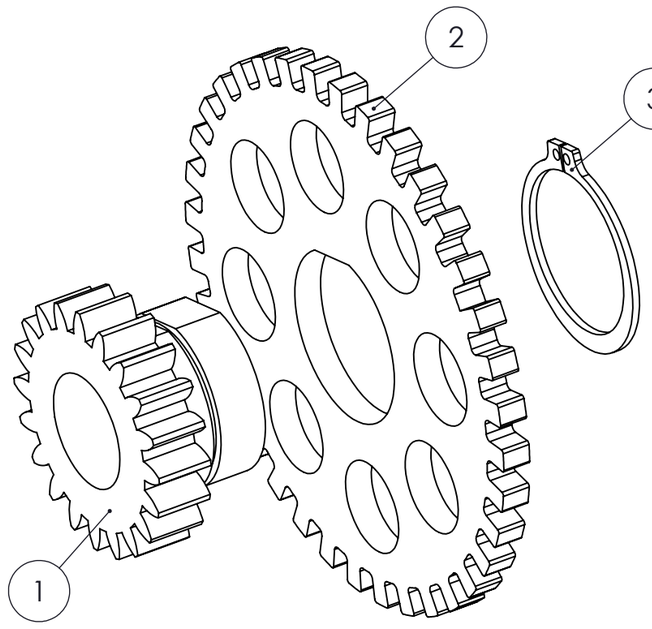

UNIVERSIDADE BEIRA INTERIOR

TITLE: 20-Tooth gear assembly

DWG NO. **4**

DESCRIPTION: Assembly composed of a commercially available 20-tooth spur gear (module 1), with its hub machined to accommodate the trigger wheel and the retaining ring. The trigger wheel is manufactured from a 5 mm hot-rolled steel sheet using laser cutting and is mounted concentrically on the gear. Axial retention is ensured by a retaining ring, providing secure alignment and reliable coupling for rotational motion sensing.

DESIGNER: Daniel Filipe da Silva Cardoso

DATE: 02/07/2024

A3 | SCALE:1:1 | SHEET 4 OF 5

ITEM NO.	DESCRIPTION	QTY.
1	Retaining ring - 3AM1-50	1
2	CAM – 10 mm hot-rolled sheet – Laser cuted	1
3	40-Tooth spur gear – M1– Steel – Hub milled	1
4	Spacer – Steel – Milled	1
5	Deep-groove ball bearing - 6003 2RS	2

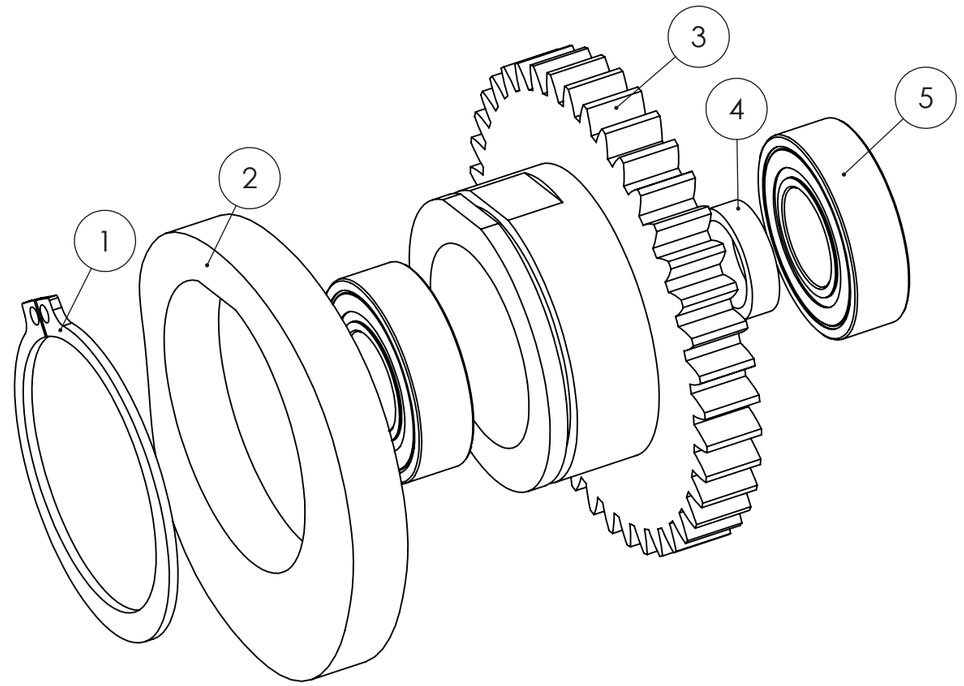

UNIVERSIDADE BEIRA INTERIOR

DESIGNER: Daniel Filipe da Silva Cardoso

DATE: 02/07/2024

TITLE: 40-Tooth gear assembly

DWG NO. **5**

DESCRIPTION: Assembly composed of a commercially available 40-tooth spur gear, with its hub machined to accommodate a 10 mm laser-cut steel cam and a retaining ring. The gear is supported by two deep-groove ball bearings, and a machined steel spacer is used to ensure the correct axial distance between the bearings. Axial retention of the cam is provided by the 3AM1-50 retaining ring. The rotational locking between the cam and the gear is achieved through a machined notch in the hub.

A3 | SCALE:1:1 | SHEET 5 OF 5